University of Minnesota
St. Anthony Falls Hydraulic Laboratory
Department of Civil and Mineral Engineering
Mississippi River at 3rd Avenue S.E.
Minneapolis, Minnesota 55414

Project Report No. 282

# Physical and Mathematical Modeling of the HYKAT

by

C.C.S. Song, J. M. Wetzel,

J. M. Killen, and R.E.A. Arndt

Prepared for
Hamburgische Schiffbau–Versuchsantalt
Hamburg, West Germany

December 1988

TABLE OF CONTENTS


| | | Page No. |
|---|---|---|
| | List of Figures | iii |
| I. | Introduction | 1 |
| II. | Mathematical Modeling | 2 |
| | A. Introduction | 2 |
| | B. Description of Mathematical Model | 2 |
| | C. Validation of Diffuser Model | 4 |
| | D. Parametric Study of Diffuser Flow | 5 |
| | 1. Effect of Asymmetric Inlet Velocity Profile | 5 |
| | 2. Effect of Asymmetric Diffuser Geometry | 5 |
| | 3. Effect of Diffuser Angle | 6 |
| | 4. Effect of Inflow Boundary Layer Thickness | 6 |
| | 5. Effect of Exit Pressure Nonuniformity | 6 |
| | E. Turning Vane Design | 7 |
| | F. Flow Adjustment with Turning Vanes | 8 |
| | G. Prototype Performance | 8 |
| III. | Physical Modeling | 10 |
| | A. The Model | 10 |
| | 1. Turning Vanes | 10 |
| | 2. Second Elbow | 11 |
| | 3. Honeycomb | 12 |
| | B. Data Collection | 12 |
| | 1. Equipment | 12 |
| | 2. Calibration | 12 |
| | 3. Measurement Procedure | 13 |

| | | Page No. |
|---|---|---|
| IV. | Discussion of Experimental Results | 15 |
| | A. Boundary Pressures | 15 |
| | 1. Contraction | 15 |
| | 2. Test Section | 15 |
| | 3. Diffuser | 15 |
| | B. Velocity Profiles | 16 |
| | 1. Pump Intake Plane | 16 |
| | 2. Inlet to Elbow No. 2 | 19 |
| | 3. Horizontal Profiles | 19 |
| | 4. Effect of Honeycomb | 21 |
| | 5. Effect of Ship Model | 21 |
| | C. Turbulence Management System | 22 |
| | D. Head Losses | 24 |
| | 1. Main Diffuser | 24 |
| | 2. Elbow No. 2 | 24 |
| | 3. Summary of Losses | 24 |
| V. | Conclusions | 26 |
| | References | 27 |
| | Figures 1 through 50 | |

## LIST OF FIGURES


| Figure No. | |
|---|---|
| 1 | Configuration of HYKAT. |
| 2 | Asymmetric inlet velocity profile used for the model compared with the base line value. |
| 3 | Comparison of calculated and measured velocity distribution of diffuser exit. |
| 4 | Comparison of calculated and measured velocity distribution at exit (calculation based on adjusted inflow velocity distribution. |
| 5 | Exit velocity distributions for various asymmetric inlet velocity profiles. |
| 6. | Variation of RQ along the diffuser for various inlet velocity profiles. |
| 7 | Effect of diffuser asymmetry on exit velocity distribution. |
| 8 | Effect of diffuser asymmetry on discharge ratio. |
| 9 | Effect of diffuser angle on discharge ratio. |
| 10 | Blockage effect on diffuser exit discharge ratio. |
| 11 | Effect of asymmetric inflow on diffuser exit discharge ratio. |
| 12 | Effect of nonuniform pressure distribution at exit on diffuser flow quality. |
| 13 | Contoured tuning vane profile. |
| 14 | Computed exit velocity distribution at first elbow. |
| 15 | Pressure distribution on recommended vane, fine mesh result compared with coarse mesh result. |
| 16 | Velocity distribution at downstream end of guidevanes; vane at normal position. |
| 17 | Velocity distribution at downstream end of guide vanes; vanes at 1 degree overturn position. |

Figure No.

18 The geometry and velocity field for HYKAT elbow with extended draft channel.

19 Velocity (boundary condition) and pressure (calculated) distributions at upstream end, Re = $1.2\times10^6$.

20 Calculated velocity and pressure distribution at 1 meter downstream compared with the given velocity distribution at the upstream end.

21 Velocity and pressure distribution on a cross–section 2 meters downstream of the center of the miter line.

22 Velocity and pressure distribution on a cross–section 4 meters downstream of the center of the miter line.

23 Velocity and pressure distribution on a cross–section 8 meters downstream of the center of the miter line.

24 Velocity distribution, magnitude and direction, on a line parallel to the miter line.

25 Variation of discharge ratio.

26 Velocity and pressure distributions with 3 degree underturning and Re = $1.82\times10^7$.

27 Velocity and pressure distributions with 1.5 degree underturning and Re = $1.2\times10^7$.

28 Sketch of 1 to 5 physical model.

29 Constant thickness turning vane profile.

30 Elbow No. 2 pump shaft fairing, vertical.

31 Elbow No. 2 pump shaft fairing, inclined.

32 Boundary pressure distributions, bottom centerline of contraction and test section.

33 Boundary pressure distribution bottom centerline, main diffuser.

34 Pump intake velocity distribution—plate vanes.

35 Pump intake velocity distribution—contoured vanes.

36 Variation of vertical plane velocity profiles around circuit.

Figure No.

37 Pump intake velocity distribution, with honeycomb.

38 Pump intake velocity distribution, with honeycomb and ship model.

39 Pump intake velocity distribution, Elbow No. 2, vanes 3° off design.

40 Pump intake axial velocity distribution—final design.

41 Pump intake tangential velocity distribution—final design.

42 Definition sketch for velocity distributions.

43 Velocity contours at inlet to Elbow No. 2.

44 Effect of reducing vane angle in Elbow No. 1 on centerline velocity profiles at Elbow No. 2.

45 Velocity profiles on horizontal centerline.

46 Vertical centerline velocity profiles, with honeycomb Elbow No. 1 vanes—design angle.

47 Vertical velocity profiles at test section exit with ship model.

48 Vertical velocity profiles at diffuser exit with ship model.

49 Velocity and turbulence intensity profiles, upstream of honeycomb and test section entrance.

50 Velocity profiles and turbulence intensity downstream of first and second honeycomb.

# I. INTRODUCTION

HYKAT is an acronym for a water tunnel that will be used for both hydroacoustic and cavitation testing. It has a somewhat different configuration than conventional water tunnels, and therefore has been subjected to considerable analysis. The first studies carried out at the St. Anthony Falls Hydraulic Laboratory were primarily concerned with the overall characteristics of the facility. These studies resulted in a recommendation for the shape of the contraction for a given contraction ratio, analysis of the turning vanes in the first elbow, turbulence management system, and overall headloss estimations. The entire effort was a "paper" study, and consisted of mathematical modeling and other analysis based on previous studies and available data. The results have been reported earlier [1].

As a result of the above mentioned work, it was recommended that additional work be carried out to verify the performance of the preliminary design. The overall configuration of the HYKAT that was to be evaluated is shown in Fig. 1. This configuration is slightly different than that originally proposed. The second elbow has been changed from a round to square cross–section, and the number of turning vanes in the elbows has been increased. The study was to include both physical and mathematical modeling. The math modeling was to be verified by the physical model so that it could then be used to predict the performance of the full–scale HYKAT. The math model would also be useful in guiding the experimental programs and possibly be used in defining new boundary shapes, if deemed necessary. A combination of both types of modeling has proven to be very effective, particularly with the opportunity for close liaison being available between the two modeling groups at the Laboratory. The results of these efforts are discussed in detail in the following sections.

# II. MATHEMATICAL MODELING

## A. INTRODUCTION

During the previous phase of the study the Euler equation model was used to design the contraction and the turning vanes in the first elbow. No further analysis of the contraction was considered necessary because the viscous effect in contracting flow is known to be insignificant.

Major objectives of the extended phase of the study were (1) to analyze the diffuser performance and (2) to optimize the turning vane design so that good flow quality at the pump intake may be achieved.

As will be described in detail later in this report, the flow in the diffuser is extremely sensitive to the inflow velocity distribution, Reynolds number, free–stream turbulence level, etc. and must be analyzed very carefully based on a turbulent flow model. The relatively unstable flow in a diffuser also makes it difficult to obtain consistent measurements in a physical model. An unsteady two–dimensional turbulent flow model was developed and applied to the diffuser design. This model will be briefly described in the next section.

Three types of turning vane profiles (1) NACA (20)315, (2) K&R(III,IV), and (3) K&R(I,II), were considered during the previous phase of the study. At the request of the sponsor the K&R (III,IV) profile was selected for further analysis and modification. The possibility of using the turning vanes at the first elbow to improve the nonsymmetrical velocity distribution produced by the diffuser was also studied.

## B. DESCRIPTION OF MATHEMATICAL MODEL

The Euler equation model used for the design of the contraction and turning vanes was described in the previous report [1] and will not be repeated here. Only the diffuser model which is a two–dimensional unsteady Navier–Stokes equation model for turbulent flows will be briefly described herein.

Because the diffuser to be considered has a very small and symmetrical lateral diffusion (1.5° included angle), a two–dimensional flow model is believed to be adequate for the purpose. The governing equations are the equation of continuity for weakly compressible flow,

$$\frac{\partial p}{\partial t} + a^2 \rho \nabla \cdot \vec{v} = 0 \tag{1}$$

and the Navier–Stokes equations of motion

$$\frac{\partial \vec{v}}{\partial t} + (\vec{v}\cdot\nabla)\vec{v} + \nabla\left(\frac{p}{\rho}\right) = \nu\nabla^2\vec{v} \tag{2}$$

in which a = speed of sound and $\rho$ = density.

For weakly compressible flows, both a and $\rho$ are assumed to be constants. Based on the cell averaged turbulent flow model [2], the kinematic viscosity is the sum of the molecular viscosity $\nu_\ell$ and the subgrid scale turbulent viscosity $\nu_t$. For the subgrid scale turbulent viscosity computation, the Smagorinsky [3] model given below was used.

$$\nu_t = (c\Delta)^2 \, (2S_{ij} \, S_{ij})^{\frac{1}{2}} \tag{3}$$

in which

$$S_{ij} = \frac{1}{2}\left(\frac{\partial u_i}{\partial x_j} + \frac{\partial u_j}{\partial x_i}\right) \tag{4}$$

In Eq. 3, $\Delta$ represents the grid size and c is a constant to be determined by calibration. Smagorinsky [3] suggested a value of 0.4 for c.

The computer model is based on the finite volume method using the predictor–corrector scheme. The velocity distribution at the upstream end and the mean pressure at the downstream end were specified as boundary conditions.

For large Reynolds number flows, like the diffuser flow of HYKAT, extremely small grids are needed to completely resolve the flow in the wall region where an extremely large gradient exists. To make the computation economically feasible by using fairly coarse grids, it is necessary to use a partial slip condition based on an assumed velocity distribution near the wall. For the flow in a diffuser, the popular logarithmic function assumption appears to be reasonable.

The time averaged velocity, $\bar{u}$, parallel to a smooth wall, is assumed to satisfy

$$\frac{\bar{u}}{\bar{u}_*} = 2.5 \, \ell n \, (0.9 \, \bar{u}_* y/\nu_\ell) \tag{5}$$

where y is the distance measured from the wall and $\bar{u}_*$ is the shear velocity defined as

$$\bar{u}_* = \sqrt{\bar{\tau}_w/\rho} \tag{6}$$

Following Schumann's [4] approach, it is further assumed that

$$\tau = (\nu_\ell + \nu_t) \frac{\partial u}{\partial y} \tag{7}$$

$$\frac{\tau}{\bar{\tau}} = \frac{u}{\bar{u}} \tag{8}$$

and $$\tau = \bar{\tau}_w \tag{9}$$

the partial slip velocity at the wall $u_w$ is related to the velocity at the center of the first grid next to the wall $u_1$ as

$$u_w = u_1 - \frac{1}{2} \Delta y \frac{\bar{\tau}_w}{(\nu_\ell + \nu_t)} \tag{10}$$

Eq. 10 is the partial slip boundary condition for the wall used for the diffuser model.

## C. VALIDATION OF DIFFUSER MODEL

As it will be explained in more detail in the following sections, the flow in a diffuser is affected by a number of factors including (1) the inflow velocity distribution (2) the Reynolds number, (3) the downstream end pressure distribution, (4) the lateral diffusion, (5) the inflow turbulence level, etc. The effect of inflow turbulence level on diffuser performance was not analyzed. The lateral diffusion affects the diffuser performance because it reduces the mean velocity over a cross section and worsens the adverse pressure gradient. The effect of reduced mean velocity is partially accounted for by comparing the results based on the normalized values. The effect of increased adverse pressure gradient is ignored. Among the first three factors, the effect of inflow velocity distribution has been found to be most important.

Because the diffuser flow is so sensitive to the variation in the inflow velocity profile, model calibration is most effectively done by adjusting the inflow velocity distribution. Very minor adjustment in the inflow velocity distribution is needed to make the calculated exit velocity profile match the measured values.

The velocity profile indicated by circles shown in Fig. 2 represents the measured velocity distribution at the inlet to the diffuser at the Reynolds number, based on the height and the velocity at the test section, of $1.2 \times 10^6$. The solid line shown in the same figure is the adjusted velocity distribution represented by

$$u = u_m - \Delta u \left( \frac{y}{H} - 0.5 \right) \tag{11}$$

where $\Delta u = 0.025$, $u_m$ is the measured velocity, y is the distance from the bottom wall, and H is the test section height. Maximum adjustment provided by Eq. 11 with $\Delta u = 0.025$ is 1.25 percent of the mean velocity.

Figure 3 shows the comparison of the calculated exit velocity profile based on the measured inflow velocity profile as the upstream boundary condition, with the measured exit velocity profile. The calculated exit velocity profile does not show the skew towards the bottom exhibited by the measured profile. Figure 4 shows the comparison of the calculated exit velocity profile, based on the adjusted inflow velocity profile as the upstream boundary condition. with the measure exit velocity distribution. A quite good match except very near the walls is indicated.

## D. PARAMETRIC STUDY OF DIFFUSER FLOW

### 1. Effect of Asymmetric Inlet Velocity Profile

The coefficient of asymmetry $\Delta u$ was varied from 0.1 to $-0.1$, corresponding to 5 percent and $-5$ percent maximum variation, and the resulting profiles were used as the upstream boundary condition while all other conditions were kept unchanged. The resulting exit velocity distributions were calculated and plotted in Fig. 5. The results show that the diffuser tends to reinforce the initial velocity asymmetry.

A better way to represent how the diffuser exaggerates an asymmetric velocity distribution is to examine the discharge ratio defined as

$$RQ = Q_{top}/Q_{btm} \tag{12}$$

where $Q_{top}$ and $Q_{btm}$ are the discharge through, respectively, the top half and the bottom half of a cross section. RQ is greater than one if the flow skews towards the top wall, but less than one if the flow favors the bottom half of the diffuser. A family of curves showing the variation of RQ in the diffuser using $\Delta u$ as a parameter is plotted in Fig. 6. This figure shows that a slight inflow asymmetry is rapidly exaggerated as the fluid moves downstream.

### 2. Effect of Asymmetric Diffuser Geometry

The HYKAT diffuser has been designed to have a horizontal top wall and the bottom wall inclined 5.4 degrees downward. In other words, the diffusion is provided entirely by the bottom wall. To study the effect of diffuser asymmetry on the flow quality, a group of diffusers with different $\theta_t/\theta$ values were considered. Here $\theta_t$ is the angle between the top wall and the horizontal line and $\theta$ is the total diffuser angle which was kept constant at 5.4 degrees. For the inflow velocity distribution, Eq. 11 with $\Delta u = 0.025$ was used.

The computed exit velocity distribution for five different values of $\theta_t/\theta$ are plotted in Fig. 7. Note that $\theta_t/\theta = 0$, 0.5, and 1.0 represent, horizontal top wall, symmetrical diffuser, and horizontal bottom wall cases, respectively. The same inflow velocity profile was used for the five different cases shown in the figure. The computed discharge ratios for these cases are plotted in Fig. 8. In examining this figure it is necessary to note that the inflow velocity distribution is slightly skewed toward the bottom wall and the initial RQ is 0.982. For this small amount of initial velocity asymmetry, the diffuser amplifies the asymmetry more when $\theta_t/\theta$ is larger. It implies that the

HYKAT diffuser which diffuses in the downward direction is more sensitive to a velocity defect near the bottom wall than a defect near the top wall.

3. Effect of Diffuser Angle

Two sets of runs, one set with RQ at a 0.982 inlet and the other with RQ of 1.045, were made to study the effect of diffuser angle. Nonsymmetrical diffusers with a horizontal top wall with different diffuser angles were analyzed. The resulting RQ at the diffuser exit are plotted in Fig. 9.

4. Effect of Inflow Boundary Layer Thickness

The flow quality in a diffuser is known to be sensitive to the inlet blockage produced by the boundary layers. Let $\delta_T$ and $\delta_B$ represent the inlet flow boundary layer thicknesses at the stop wall and the bottom wall, respectively. Then the blockage factor, B, may be expressed as

$$B = \frac{\delta_T + \delta_B}{(1+n)H_i} \tag{13}$$

where $H_i$ is the diffuser height at inlet and n is the exponent of the boundary layer velocity profile based on the power law approximation. In addition, the asymmetry parameter, $A_f$, defined as

$$A_f = \frac{\delta_T}{\delta_B} \tag{14}$$

has been found to be an extremely important factor affecting the diffuser flow.

A series of numerical experiments were carried out for the HYKAT diffuser to study the effect of B and $A_f$ on the flow quality parameter RQ. For this purpose, n = 5.125 obtained from the physical model was used for all calculations. The calculated RQ at the diffuser exit, as a function of B, for three fixed values of $A_f$, are plotted in Fig. 10. The symbol s in the figure indicates the existence of flow separation or stall. Clearly, with sufficiently large B, stall can occur. Also stall is more likely to occur when $\delta_T < \delta_B$ than when $\delta_T > \delta_B$. The same data are replotted in Fig. 11 using $A_f$ as the independent variable and B as the parameter. Note that the three curves intersect at $A_f$ slightly greater than unity because the diffuser is nonsymmetrical. For a symmetrical diffuser, the point of intersection would be at $A_f = 1$.

5. Effect of Exit Pressure Nonuniformity

As indicated in previous sections, the majority of numerical simulations assumed constant pressure at the diffuser exit. In reality the diffuser is followed very closely by a 90 degree elbow with turning vanes. Therefore, a slightly nonuniform pressure is expected to occur at the diffuser exit. According to the mathematical model of the turning vanes to be described

later, the pressure at diffuser exit can be approximated by the following equation.

$$P_d = \bar{P}_d + d_p\left(\frac{1}{2}\rho\,\bar{U}^2\right)\left[3\left(\frac{y}{H_d}\right)^2 - 2\left(\frac{y}{H_d}\right)^3\right] \qquad (15)$$

where $\bar{P}_d$ is the average pressure, $\bar{U}$ is the average velocity, and $y/H_d$ is the relative position. $d_p$ is the maximum difference in a dimensionless pressure at the exit.

The computed RQ along the diffuser length for various values of $d_p$ is plotted in Fig. 12. This figure indicates that the effect of pressure nonuniformity is limited to a small region near the exit. Since the experimental data indicates $|d_d| < 0.1$, the effect of pressure nonuniformity does not need to be considered for the HYKAT diffuser design.

## E. TURNING VANE DESIGN

The original K&R (III,IV) vanes were found to slightly underturn the flow because the line bisecting the trailing edge of the vane is off the vertical line by about 1.8 degrees. The vane profile was modified to correct this problem. As shown in Fig. 13, the arc length of the outer surface is increased by 3.6 degrees so that the tangent is parallel to the vertical line. The modified profile is shown in Fig. 13. Assuming uniform inflow velocity distribution, the exit speed and flow angle are computed and plotted in Fig. 14. The modeling results show that the modified vanes turn the flow perfectly. The calculated mean pressure distribution is plotted in Fig. 15.

Acoustic considerations by the sponsor led to the selection of vanes exactly half the size originally proposed by doubling the number of vanes. The performance of these smaller vanes in the first elbow was evaluated using the mathematical model. First, the vanes are placed according to the original design and the measured velocity profile at the diffuser exit was used as the upstream end boundary condition. The calculated speed distribution immediately downstream of the vane (dotted line) and the inlet speed (solid line) are shown in Fig. 16(a). The corresponding flow angle referred to the vertical line at guide vane exit is plotted in Fig. 16(b). The number of velocity peaks shown in the figure is identical to the number of vanes. The spatial oscillation of the velocity field rapidly damps out as the flow moves away from the vanes. As an average, the vanes underturn the flow for about 1.5 degrees at the end of the vanes.

For the next trial, the vanes were rotated to a 1 degree overturning position. The resulting exit velocity distributions are shown in Fig. 17(a) and Fig. 17(b). As an average, the flow is still about 0.5 degrees underturned at the exit. This condition is acceptable because the flow will rapidly adjust itself and become perfectly parallel to the walls within a small distance.

## F. FLOW ADJUSTMENT WITH TURNING VANES

Measurements in the physical model at the diffuser exit showed the tendency for the velocity profile to be skewed towards the bottom wall and RQ is less than one. The velocity profile just upstream of the pump impeller is also found to be nonsymmetrical. For this reason, it was decided to study the feasibility of using the guide vanes to improve the velocity distribution.

In order to make a detailed study of how the turning vanes modify the flow field, a hypothetical elbow with a long, straight draft channel as shown in Fig. 18 was modeled. The turning vanes were rotated –3 degrees from the original design position. The downstream end boundary is far enough away from the vanes so that the assumption of constant pressure there should not cause significant error anywhere. A measured velocity profile at the diffuser exit which is located 3.5 meters upstream measured from the center of the miter line for Re = $1.2\times10^6$ as shown in Fig. 19 (solid line) was used as the upstream boundary condition. Also shown in this figure is the nonuniform pressure distribution at the upstream end induced by the elbow and vanes as predicted by the mathematical model.

The calculated velocity distribution at 1 meter downstream (dotted line) is compared with the given velocity distribution at the upstream end (solid line) in Fig. 20. Similar comparisons are made in Figs. 21, 22, and 23 for three sections located downstream of the elbow. The velocity distribution on a line parallel to the miter line located just downstream of the trailing edge of the turning vanes are shown in Fig. 24. The variation of RQ along the general flow direction is plotted as Curve 1 in Fig. 25.

A fairly clear picture of how the underturned vanes affect the flow field emerges from Fig. 18 to Fig. 25. First, in the region upstream of the vanes, the pressure field generated by the underturned vanes actually diverts the flow toward the bottom wall, contradicting the stated purpose. The flow exiting the turning vanes has RQ = 0.81 which is a significant reduction from the initial value of 0.91. However, the average flow angle at the turning vane exit of 3.6 degrees causes the flow to gradually shift toward the outer wall as indicated by the increasing RQ. This change in the exit flow angle caused by the vane rotation is responsible for the redistribution of the flow in a desired direction. An important factor dictating the effectiveness of flow redistribution by vane rotation is the existence of a sufficiently long, straight channel downstream of an elbow. According to Fig. 23 and Fig. 25, the flow in the physical model at Re = $1.2\times10^6$ is made nearly symmetrical (RQ = 0.98) at 8 meters downstream of the miter line if the vanes are underturned 3 degrees.

## G. PROTOTYPE PERFORMANCE

It was pointed out in the previous section that the flow at eight meters downstream of the first elbow may be made nearly symmetrical by underturning the vanes in the first elbow by 3 degrees if the Reynolds number is $1.2\times10^6$. For a higher Reynolds number, the flow at the diffuser exit or the elbow entrance is expected to be more uniform and symmetrical. This means a 3 degree underturning would overadjust the flow at the prototype flow condition. In Fig. 26 the velocity distributions at the section 8 meters downstream of the miter line with 3 degrees underturning and at the

maximum prototype flow condition, Re = $1.82 \times 10^7$, are plotted. The discharge coefficient of 1.08 indicates over adjustment.

As a reasonable design target, approximately 65 percent of maximum velocity or Re = $1.2 \times 10^7$ was selected for the purpose of determining the turning vane setting. It was determined by trial that the optimum condition is obtained by underturning the turning vanes 1.5 degrees. In this case RQ = 1.01 at 8 meters downstream and the velocity and pressure distributions are as shown in Fig. 27.

The variation of RQ along the general direction of the flow for three cases, Re = $1.2 \times 10^6$ and 3 degrees undertuning, Re = $1.82 \times 10^7$ and 3 degrees underturning, and Re = $1.2 \times 10^7$ and 1.5 degrees underturning are plotted in Fig. 25.

# III. PHYSICAL MODELING

## A. THE MODEL

A physical model was constructed to a scale of 1 to 5 using air as the working fluid rather than water. This was done to reduce the structural loading on the model components, as well as to make the turbulence measurements easier to obtain. The ratio of the Reynolds numbers between the model and full–scale at the design flow velocity was about 1 to 18.

A sketch of the model is shown in Fig. 28. It is to be noted that the entire flow circuit was not modeled. The components between the pump and the fourth elbow have not been included. It was decided that the pump would not be modeled in this circuit, and an axial flow Joy Manufacturing fan was available at the Laboratory which could readily be installed in a partial flow circuit. The fan motor speed was constant, and the fan blades were adjustable at rest. The configuration shown was adopted so that a high quality flow entered the fourth elbow which would serve as a basis for all other flow conditions. The inlet consisted of a bellmouth obtained from the fan manufacturer, and this bellmouth extended into a very large open area in the Laboratory to approximate an infinite reservoir. Fine filter material was placed just downstream of the inlet to collect dust particles that would otherwise rapidly destroy the hot–wire probes used for velocity measurement. The contraction, test section, and diffuser were constructed of transparent plastic to permit flow visualization. Many pressure taps were drilled in these components, usually along axial centerlines. Several viewing ports were also installed in the second elbow in the region of the shaft fairing.

### 1. Turning Vanes

An extensive theoretical analysis was made of the turning vane configuration. The results of this analysis have been previously reported [1]. The configuration adopted was a modification of the vane profile used in the K–16 tunnel at Hamburgishe Shiffbau–Versuchsantalt (HSVA). This profile was suggested by the sponsor due to the relative ease in fabrication. Following the original theoretical analysis of the cascade, it was determined by HSVA that the vane spacing for the HYKAT should be the same as in the K–16 tunnel. The spacing was related to the acoustic performance of the vanes, and was about one–half of that proposed. Thus, to keep the space–chord ratio of one–half, the chord of the profile was also reduced by about one–half. The math model was used to recalculate the performance of the new cascade, and through several iterations, it was found that performance could be improved by changing the aft portion of the profile slightly. The dimensions of the profile are shown in Fig. 13. These vanes have been proposed for use in all four elbows.

It was anticipated that some change in the stagger angle from the design value may be required during the test program. Therefore, the cascade of

vanes was assembled in a frame which could be inserted in a gap provided in the elbow. It was thus possible to remove the entire vane assembly as a unit for adjustment of the vanes.

The vanes themselves were fabricated as an aluminum extrusion. Long lengths were furnished by the fabricator which were cut to length as required. A jig was made for the accurate drilling of holes in each end of the vane to accommodate steel pins. Holes were also drilled in the frame at the proper spacing for vane positioning. With this arrangement it was possible to rotate the vanes about the steel pins. The stagger angle of the vanes was set with a machinist's protractor based on the angle between the nose–tail line and the miter line. The nose–tail line was measured from an enlarged drawing of the vane profile. Initial tests were made with the vane cascade at the design angle. Two splitter plates that divided the elbow span in thirds were used. These plates were made of plywood 0.25 m thick. Openings that accurately matched the vane profile and at the proper spacing were sawn in the splitter plates, which were then passed over the vanes to hold them in place.

For tests made at other than the design angle of attack, the splitter plates were removed. A narrow 16 gauge (1.6 mm) sheet metal plate was fabricated with notches made at the proper vane spacing to fit the trailing edge of the vanes. The notches were equally spaced. After the desired angle was set, the plate was fastened to the frame locking each of the vanes in place. This permitted rapid adjustment of the vane angle.

As delays were encountered in obtaining the contoured vanes from the fabricator, temporary vanes were made so that preliminary measurements could be made of the overall performance of the design. These vanes were bent from 16 gauge (1.6 mm) sheet metal plates to the contour shown in Fig. 29. This particular shape, angle of attack, and space–chord ratio was selected as it is being used in a large wind tunnel being constructed at the Laboratory. Therefore, the cascade has undergone rather extensive theoretical analysis. It should be noted that a space–chord ratio of 0.25 is used rather than the 0.5 proposed for the contoured vanes. However, the magnitude of the vane spacing is the same for both the plate and contoured profiles.

The plate vanes were also installed in a frame that was inserted in the elbow. Two metal pegs were soldered to each end of the vanes. These pegs were inserted into holes in the frame which were drilled using a jig to provide the proper spacing and angle.

2. Second Elbow

The second elbow is complicated by the pump shaft passing through the vane cascade. Based on the earlier design of the 36 in. water tunnel at DTNSRDC and the more recent Large Cavitation Channel, fairings were installed both upstream and downstream of the miter line. The leading edge of the upstream fairing was parallel with the elbow miter line, and was elliptically shaped as shown in Fig. 30. Two configurations of the downstream fairing were used. The trailing edge of the first fairing was perpendicular to the tunnel centerline. This fairing was later revised so that the trailing edge was parallel to the miter line. Dimensions are shown in Figs. 30 and 31.

The vanes were assembled in a frame which was slipped into a gap in the elbow. The vanes spanned the entire width of the elbow. To enclose the gap between the upstream and downstream portion of the shaft fairing, plates were installed. These plates had openings sawn to the shape of the vane profile and at the proper positions. The plates were then slipped over the vanes to hold them in place, smooth with the upstream and downstream fairings. New plates were required for each change in vane angle.

Details of the pump shaft and hub were taken from Pleuger Drawing No. SK 2087.3, dated September 15, 1987, and supplied by HSVA. The pump shaft itself was turned from a piece of wood to the scaled dimensions. The hub of the pump impeller was also included and supported with three thin, shaped struts that extended to the walls. Adjustable faired legs were provided so that the hub could be located in the center of the pump housing.

### 3. Honeycomb

The honeycomb used in the HYKAT model was obtained from the American Cyanamid Company, Maryland. It was an expanded commerical grade aluminum with a material thickness of 0.003 inches. The hexagonal cell size was 0.25 inches across the flats and the depth was 6 inches. Two honeycomb units were installed in series with a 6–inch spacing. The first unit was located immediately downstream of the vanes in elbow No. 4. The downstream face of the second honeycomb was located 10 inches from the entrance to the contraction.

## B. DATA COLLECTION

### 1. Equipment

The following equipment and their pertinent specifications were used for the experimental measurements:

- LeCroy analog to digital converter Model 8210.
  - 16 channels
  - Simultaneous sample and hold
  - 11 bit digitizer
  - ± 5 volt range
  - 1. to 100 microsecond sampling interval unlimited, with external control
  - 8000 to 32000 words internal storage.

- AT&T 3B2 computer with 4 megabytes of 32 bit memory and 140 megabytes of hard disk storage.

- TSI hot wire anemometer controller Model 1050 and Model 1240–T1.5 hotwire probes
  - Signal conditioner and filters

- Validyne pressure transducer Model DP 103–16 and controller Model CD 23–F.
  - 10 inches of water pressure range
  - x 10 range multiplier
  - ± 10 volt output

- Merriam micro-manometer
  - ± 10 inches of water range
  - Resolution 0.001 inches water

- Orifice–type velocity calibrator

2. Calibration

a. Pressure

The pressure measurement system, composed of the pressure transducer, controller, AD converter, and computer was adjusted to give pressure in inches of water as it appeared on the computer readout and compared with the micromanometer reading. Accuracy was limited by the AD converter to 3 digits.

b. Velocity

The hot wire anemometer probe was placed in the potential core region of air flow from a sharp edged orifice mounted in a large chamber. The chamber was filled with a number of damping screens to reduce turbulence in the flow approaching the orifice. Pressure drop across the orifice was measured with the micromonometer. The probe was calibrated with the velocity calculated from the pressure measurements. These data were used to determine the constants and exponent in King's equation or the parameters in a fourth order polynomial. The computer was programmed to linearize the output of the anemometer using one or the other of these equations.

3. Measurement Procedure

a. Pressure measurements

Pressures on the model were measured in one of two ways; either with the micromanometer connected directly to pressure taps when a single point measurement was desired, or by means of the pressure transducer and a 30 position scanning valve when a large number of locations were of interest. The AD converter and computer were used to process and store the readings from the transducer. The sampling rate of the AD converter was adjusted so approximately 10 seconds were required to take 8000 samples (the minimum storage of the AD converter) and then averaged by the computer program to give the desired reading.

b. Velocity measurements

All velocity measurements were made with the hot–wire anemometer and AD converter under computer program control. The AD converter sampling rate was 10,000 sps and the anemometer filters cut–off frequency set at 5,000 Hertz. Sampled voltage was converted to velocity by a linearizing program; the velocity readings were then averaged over the sample. If turbulent velocity fluctuations were desired, the above average was subtracted from the velocity samples and an r.m.s. average formed from the resulting fluctuating part of the velocity samples. When it was desired to measure very low turbulence as would occur in the test section, low frequency filters were switched into the anemometer circuit to remove the average component of velocity and amplification was added to increase the fluctuating component to the level needed to achieve the greatest possible accuracy with the AD converter. Sample readings were converted to velocity by multiplying the voltage fluctuation by the slope of King's equation at the measured mean velocity point. R.m.s. values were then formed in the usual way.

Velocity readings were referenced to the measured mean velocity in the test section with the same hot wire probe if possible to compensate for drift in anemometer calibration which occurs with hot wire anemometers.

# IV. DISCUSSION OF EXPERIMENTAL RESULTS

## A. BOUNDARY PRESSURES

### 1. Contraction

Boundary pressures were measured along the longitudinal centerline of the bottom surface of the contraction. These data are plotted in Fig. 32. The data have been reduced in terms of a pressure coefficient, with the test section pressure and velocity being used as the reference values. The pressure distribution calculated with the three–dimensional math model is also shown for comparison purposes. The agreement is satisfactory.

### 2. Test Section

The measured pressure distribution along the bottom centerline of the test section is also plotted in Fig. 32. The scale for the pressure coefficient is shown on the right ordinate. In this case the length of the test section has been used for the normalizing length in the abscissa. The measured pressure coefficient, $C_p$, over a full–scale length of 10.16 m is 0.06. The pressure coefficient can be related to a skin friction coefficient, $C_f$, by the equation

$$C_f = C_p \frac{A}{A_p}$$

where A is the cross–sectional area of the test section and $A_p$ is the boundary area of the length of test section. Thus, with a ratio of A to $A_p$ of 0.050, $C_f$ is calculated to be 0.003. This can be compared to a value of $C_f$ for a smooth, flat plate in a turbulent boundary layer at a model Reynolds number, $Re_\ell$ of $6.1\times10^6$, based on boundary length. Using the equation

$$\frac{1}{\sqrt{C_f}} = 4.13 \log (Re_\ell C_f)$$

$C_f$ is calculated to be 0.00318, and the comparison with the measured value seems reasonable. At a full–scale Reynolds number of $1.4\times10^8$, the skin friction coefficient drops to 0.00198.

### 3. Diffuser

Pressure measurements were made along the bottom centerline of the diffuser and are shown in Fig. 33. These pressures were referenced to the pressure at the inlet to the diffuser, and the test section velocity was used as the reference velocity. From these measurements, it was initially decided that the diffuser did not exhibit very large separation regions or seriously adverse performance. Additional comments are made about the expected performance of the full–scale diffuser in other sections.

## B. VELOCITY PROFILES

### 1. Pump Intake Plane

Most interest was directed towards the velocity profiles at the intake plane of the pump. Velocities were measured along radial lines from the hub to the outer housing of the pump impeller. The distance along the lines has been made dimensionless by dividing with the outer radius. A number of radial lines have been used, and the circumferencial position of these lines has been referenced to top center with the angle increasing in a clockwise direction looking at the pump impeller.

The first set of measurements for mean velocities are plotted in Fig. 34. These measurements were taken with the turning vanes of constant thickness installed in all three elbows, and the shaft fairing configuration with the trailing edge vertical. Considerable variation of the velocity can be noted throughout the plane, particularly in the circumferential direction. Deficiency in the velocity exists at the bottom of the plane, i.e. at $\theta = 180°$. This deficiency was considered unacceptable.

The shaft fairing was consequently modified to incorporate a trailing edge parallel to the miter line of the second elbow. The vanes of constant thickness were replaced with the recommended contoured vanes in each of the three elbows. The measurements were repeated and are plotted in Fig. 35. Some improvement in velocity uniformity was noted, but not to the extent desired.

This resulted in a very extensive search for the source of the non–symmetry. It was hoped that the velocity deficiency could be corrected without requiring major modifications to the HYKAT configuration. Velocity profiles were taken at various planes in the flow circuit, and are presented in other sections. It was found that the non–symmetry of the velocity profile was originating at the exit of the main diffuser and was being transmitted through the two elbows without being significantly changed. A diagram of the general flow characteristics is shown in Fig. 36. This diagram shows the progress of a velocity profile in the vertical plane of the water tunnel as it originates at the exit of the test section. The distorted profile at the exit of the diffuser passes through the first elbow without change. A slight modification occurs in the diffuser between the first and second elbow. This profile moves through the second elbow with the result shown at the pump inlet plane. The velocity at the top at a given radius is higher than the velocity at the bottom.

Some measurements were also made to determine the influence of adding the honeycomb upstream of the contraction and also the ship model in the test section. These results are shown in Figs. 37 and 38, with little effect noted.

Attempts were made to alter the velocity profile by reducing the turning action of the vanes and thereby direct more of the flow to the outside of the flow circuit. The stagger angles of the same cascade were reduced uniformly in increments of three degrees from the design angle. These angles were first changed in elbow No. 1 and later in elbow No. 2. The mathematical model

of the turning vanes was used to guide the direction of the physical model tests, and close interaction existed between the two models. Results with the vane angle reduced by 3 degrees in the second elbow are shown in Fig. 39.

The final result of this continued interaction is shown in Fig. 40 for the velocity distribution at the pump intake plane. At the request of the sponsor, a more complete mapping of the velocity field was made, which included additional circumferential positions. Measurements of the tangential velocity component have also been made for selected positions. These data are shown in Fig. 41.

Tabulated values of the axial velocity ratios as a function of radius and angle are given in Table 1. These values were then extrapolated to a full-scale Reynolds number.

The method used to obtain the predicted velocity distribution at the pump entrance corresponding to the prototype Reynolds number for a test section velocity of 8 m/s is described below. Velocity distributions at the diffuser exit and the pump entrance in the physical model were measured. These are indicated by $U_{m1}$, $U_{m2}$, $u_{m1}$, $u_{m2}$ in Fig. 42. The mathematical model of the diffuser, calibrated with the measured velocity distribution, was used to calculate the velocity distribution at the diffuser exit under prototype condition ($U_{p1}$ and $U_{p2}$).

The next step is to determine how the flow at the diffuser exit is divided into the outer zone ($U_{m1}$ and $U_{p1}$) and the inner zone ($U_{m2}$ and $U_{p2}$). This is done by determining the thickness, h, such that

$$\frac{\int_0^h U_{m_2}\, dy}{\int_h^H U_{m_1}\, dy} = \frac{\int_2 u_{m_2}\, dy}{\int_1 u_{m_1}\, dy} \tag{16}$$

The relative differences between the prototype velocities and the corresponding model velocities are defined as follows.

$$\alpha_1 = \frac{U_{p_1} - U_{m_1}}{U_{m_1}} \quad ; \quad \alpha_2 = \frac{U_{p_2} - U_{m_2}}{U_{m_2}} \tag{17}$$

the parameters $\alpha_1$ and $\alpha_2$ are local correction factors needed to extrapolate the model velocity profile to obtain the prototype velocity profile at the diffuser exit. We now assume that the correction factors for the diffuser exit are also applicable to the pump inlet and set

$$u_{p_1} = (1 + \alpha_1)u_{m_1} \tag{18}$$

$$u_{p_2} = (1 + \alpha_2)u_{m_2} \tag{19}$$

TABLE 1. Pump Intake Velocity Distribution
Elbow No. 2 Vane Angle, Design Less 1.5°

| | $V/V_{TS}$ Axial Velocity Ratio $R/R_o$ | | | | | | | |
|---|---|---|---|---|---|---|---|---|
| $\theta°$ | 0.38 | 0.4 | 0.5 | 0.6 | 0.7 | 0.8 | 0.9 | 0.95 |
| 0 | 0.59 | 0.58 | 0.55 | 0.50 | 0.46 | 0.42 | 0.39 | 0.37 |
| 15 | 0.61 | 0.61 | 0.60 | 0.55 | 0.50 | 0.46 | 0.43 | 0.41 |
| 30 | 0.60 | 0.60 | 0.60 | 0.56 | 0.51 | 0.46 | 0.40 | 0.38 |
| 45 | 0.59 | 0.59 | 0.60 | 0.58 | 0.50 | 0.45 | 0.39 | 0.37 |
| 60 | 0.58 | 0.59 | 0.59 | 0.57 | 0.52 | 0.46 | 0.40 | 0.37 |
| 75 | 0.57 | 0.57 | 0.56 | 0.56 | 0.53 | 0.49 | 0.43 | 0.41 |
| 90 | 0.54 | 0.54 | 0.52 | 0.52 | 0.51 | 0.48 | 0.44 | 0.41 |
| 105 | 0.54 | 0.54 | 0.52 | 0.49 | 0.47 | 0.45 | 0.43 | 0.40 |
| 120 | 0.52 | 0.50 | 0.46 | 0.44 | 0.42 | 0.40 | 0.37 | 0.35 |
| 135 | 0.51 | 0.50 | 0.45 | 0.41 | 0.39 | 0.36 | 0.34 | 0.32 |
| 150 | 0.51 | 0.50 | 0.43 | 0.38 | 0.34 | 0.33 | 0.32 | 0.31 |
| 165 | 0.51 | 0.50 | 0.46 | 0.41 | 0.36 | 0.35 | 0.34 | 0.34 |
| 180 | 0.52 | 0.52 | 0.48 | 0.44 | 0.41 | 0.38 | 0.37 | 0.36 |
| 195 | 0.52 | 0.52 | 0.48 | 0.43 | 0.39 | 0.37 | 0.35 | 0.34 |
| 210 | 0.52 | 0.52 | 0.47 | 0.42 | 0.38 | 0.36 | 0.36 | 0.33 |
| 225 | 0.54 | 0.53 | 0.50 | 0.45 | 0.42 | 0.42 | 0.41 | 0.40 |
| 240 | 0.53 | 0.53 | 0.50 | 0.47 | 0.45 | 0.44 | 0.41 | 0.40 |
| 255 | 0.56 | 0.55 | 0.52 | 0.49 | 0.46 | 0.44 | 0.41 | 0.40 |
| 270 | 0.57 | 0.57 | 0.55 | 0.52 | 0.49 | 0.46 | 0.42 | 0.40 |
| 285 | 0.62 | 0.60 | 0.57 | 0.54 | 0.51 | 0.47 | 0.44 | 0.41 |
| 300 | 0.60 | 0.61 | 0.60 | 0.57 | 0.53 | 0.50 | 0.44 | 0.41 |
| 315 | 0.60 | 0.61 | 0.62 | 0.56 | 0.51 | 0.47 | 0.41 | 0.37 |
| 330 | 0.59 | 0.59 | 0.57 | 0.53 | 0.48 | 0.43 | 0.38 | 0.35 |
| 345 | 0.59 | 0.58 | 0.56 | 0.50 | 0.45 | 0.41 | 0.37 | 0.36 |

Strictly, the extrapolation equations are applicable only between the corresponding planes, i.e. between the center plane of the diffuser and the 0°–180° plane of the pump inlet. But, because there is no known way of relating the velocity distribution in a rectangular section to that of an annulus, the same parameters $\alpha_1$ and $\alpha_2$ are used for other planes. Judging from the shape of the model velocity distributions at the pump inlet, $\alpha_2$ is used for the area within $60° < \theta < 300°$ and $\alpha_1$ is used for the remaining area. Actually the extrapolated velocity profiles $u_{p1}$ and $u_{p2}$ are further normalized so that the discharge for the two different Reynolds number cases are identical. The final predicted values for the velocity distribution at full–scale Reynolds number are tabulated in Table 2.

2. Inlet to Elbow No. 2

Velocity profiles were initially measured on centerlines. The profiles in the vertical plane were generally skewed, and the profiles in the horizontal plane were generally symmetrical. During the course of the study to determine the source of the non–symmetry, additional measurements were made at the inlet to Elbow No. 2. The vanes of constant thickness were installed at their design angle in the elbows for this case. The additional stations were at the quarter points across the section. Contour lines of constant velocity have been sketched based on these measurements, and the isovels are shown in Fig. 43. The lower velocity on the outside of the flow circuit is apparent, and reasonable symmetry is evident in the lateral direction. It was determined that the non–symmetry at the pump existed upstream of the second elbow, and was not wholly dependent on the conditions at the second elbow.

A series of tests were run to determine the extent to which a velocity profile could be modified by reducing the turning angle of the vanes. The contoured vanes in the first elbow were rotated uniformly 3, 6, and 9 degrees from the design angle. Velocity measurements were made at the inlet to Elbow No. 2 along the centerline. The experimental data are plotted in Fig. 44. The design angle data are shown as a basis for comparison. As the vane angle is reduced, some improvement in the symmetry of the velocity profile can be noted. The largest effect on the velocity near the inside wall occurs with the vanes 9 degrees off the design angle. It is expected that flow separation is occurring for this extreme angle, and considerable mixing is taking place. However, separation is not desirable from noise considerations, and therefore large deviations from the design angle are not recommended.

3. Horizontal Profiles

At some selected locations, mean velocity profiles were taken along centerlines. These profiles are plotted in Fig. 45. The reference velocity for all the profiles was taken as the centerline velocity at the entrance to the test section. The four stations are at the entrance to the contraction, exit of contraction, test section exit, and diffuser exit. It can readily be seen that the velocity profiles are essentially symmetrical in the horizontal plane.

TABLE 2. Predicted Pump Intake Velocity Distribution
Fully Scale
Elbow No. 2 Vane Angle–Design Less 1.5°

| | $V/V_{TS}$ Axial Velocity Ratio $R/R_o$ | | | | | | | | | | |
|---|---|---|---|---|---|---|---|---|---|---|---|
| $\theta°$ | 0.37 | 0.44 | 0.51 | 0.58 | 0.64 | 0.71 | 0.77 | 0.84 | 0.91 | 0.94 | 0.97 |
| 0 | 0.54 | 0.52 | 0.50 | 0.48 | 0.48 | 0.49 | 0.47 | 0.46 | 0.44 | 0.42 | 0.39 |
| 15 | 0.57 | 0.56 | 0.54 | 0.53 | 0.53 | 0.53 | 0.52 | 0.52 | 0.48 | 0.45 | 0.40 |
| 30 | 0.55 | 0.55 | 0.54 | 0.53 | 0.53 | 0.54 | 0.52 | 0.49 | 0.45 | 0.43 | 0.40 |
| 45 | 0.54 | 0.55 | 0.54 | 0.54 | 0.54 | 0.53 | 0.51 | 0.48 | 0.42 | 0.41 | 0.37 |
| 60 | 0.55 | 0.56 | 0.56 | 0.56 | 0.56 | 0.54 | 0.50 | 0.46 | 0.43 | 0.41 | 0.37 |
| 75 | 0.54 | 0.54 | 0.54 | 0.54 | 0.54 | 0.54 | 0.52 | 0.49 | 0.48 | 0.43 | 0.40 |
| 90 | 0.52 | 0.51 | 0.50 | 0.50 | 0.50 | 0.51 | 0.51 | 0.50 | 0.47 | 0.43 | 0.40 |
| 105 | 0.52 | 0.50 | 0.48 | 0.48 | 0.47 | 0.48 | 0.48 | 0.46 | 0.46 | 0.43 | 0.40 |
| 120 | 0.50 | 0.47 | 0.44 | 0.43 | 0.43 | 0.44 | 0.43 | 0.41 | 0.40 | 0.37 | 0.35 |
| 135 | 0.49 | 0.46 | 0.43 | 0.41 | 0.39 | 0.40 | 0.38 | 0.37 | 0.37 | 0.35 | 0.32 |
| 150 | 0.48 | 0.46 | 0.42 | 0.38 | 0.36 | 0.35 | 0.35 | 0.34 | 0.34 | 0.33 | 0.31 |
| 165 | 0.49 | 0.46 | 0.44 | 0.42 | 0.37 | 0.38 | 0.38 | 0.37 | 0.37 | 0.36 | 0.33 |
| 180 | 0.49 | 0.49 | 0.45 | 0.44 | 0.42 | 0.42 | 0.42 | 0.40 | 0.40 | 0.38 | 0.36 |
| 195 | 0.50 | 0.48 | 0.46 | 0.43 | 0.41 | 0.40 | 0.40 | 0.39 | 0.37 | 0.36 | 0.34 |
| 210 | 0.50 | 0.48 | 0.45 | 0.42 | 0.40 | 0.39 | 0.39 | 0.39 | 0.38 | 0.35 | 0.33 |
| 225 | 0.52 | 0.49 | 0.48 | 0.45 | 0.43 | 0.43 | 0.44 | 0.45 | 0.45 | 0.42 | 0.36 |
| 240 | 0.51 | 0.49 | 0.48 | 0.46 | 0.45 | 0.46 | 0.47 | 0.47 | 0.45 | 0.42 | 0.37 |
| 255 | 0.53 | 0.52 | 0.50 | 0.48 | 0.47 | 0.47 | 0.47 | 0.46 | 0.46 | 0.41 | 0.37 |
| 270 | 0.55 | 0.54 | 0.53 | 0.51 | 0.50 | 0.50 | 0.49 | 0.47 | 0.45 | 0.40 | 0.35 |
| 285 | 0.63 | 0.55 | 0.55 | 0.53 | 0.53 | 0.52 | 0.51 | 0.49 | 0.47 | 0.45 | 0.40 |
| 300 | 0.57 | 0.58 | 0.58 | 0.57 | 0.56 | 0.55 | 0.55 | 0.50 | 0.49 | 0.45 | 0.37 |
| 315 | 0.55 | 0.55 | 0.55 | 0.55 | 0.54 | 0.54 | 0.54 | 0.51 | 0.46 | 0.43 | 0.39 |
| 330 | 0.54 | 0.54 | 0.52 | 0.51 | 0.51 | 0.51 | 0.50 | 0.46 | 0.43 | 0.40 | 0.37 |
| 345 | 0.54 | 0.53 | 0.50 | 0.48 | 0.47 | 0.48 | 0.47 | 0.46 | 0.43 | 0.41 | 0.37 |

4. Effect of Honeycomb

Velocity measurements in the vertical plane along centerlines were repeated after the honeycomb was installed upstream of the contraction. The locations were at the test section exit, diffuser exit, and the inlet to Elbow No. 2. The contoured vanes in Elbow No. 1 were set at their design angle. The data are plotted in Fig. 46, and the velocities have been made dimensionless by dividing by a reference velocity. This reference velocity is the velocity at the midpoint of each station and is indicated on the plot. The data are compared with other profiles taken earlier without the honeycomb in place.

At the exit of the section, the profile with the honeycomb in place is slightly fuller near the top surface than without the honeycomb. Little difference can be noted in other regions of the profile. The same trend is seen at the diffuser exit. The symmetry of the exit profile improved with the addition of the honeycomb. Some asymmetry is still seen at the inlet of Elbow No. 2.

Some measurements were also made of the axial turbulence intensity at the diffuser exit. The rms of the axial fluctuating velocity component has been divided by the local mean velocity. The data indicate that turbulence intensity is low near the center and increases quite rapidly as the walls are approached. The intensity near the bottom surface is considerably higher than near the top surface, approaching 40 percent. This distribution is fairly typical and has been observed in other measurements on the Large Cavitation Channel.

5. Effect of Ship Model

The ship model provided by HSVA was installed on the top flat surface of the test section with the midship point located at half the test section length from the entrance. Measurements were made of the velocity distribution in a vertical plane and along centerlines at both the exit of the test section and exit of the main diffuser. These measurements were made with the honeycomb installed upstream of the contraction.

The mean velocity profiles are plotted in Figs. 47 and 48 for both these locations. A comparison is made of the profiles with and without the ship model. The data with the ship model indicate a deficiency of the velocity in the region near the top of the test section. This region reflects the wake from the ship model. Near the bottom of the test section the velocity profile appears to be fuller than without the ship model.

At the diffuser exit, the velocity also has been normalized with the test section velocity. The velocity profiles on the inside half of the diffuser are essentially the same, even though the inflow velocity profiles were different. Near the top of the diffuser the velocity is higher with the model in place. This may be associated with the additional mixing due to the wake of the ship model.

## C. TURBULENCE MANAGEMENT SYSTEM

The honeycomb consists of two sections of the hexagonal cell material 6 inches deep with a spacing of 6 inches. As the turbulence level of the flow entering the honeycomb was quite low because of the bellmouth entrance, it was necessary to create some additional turbulence. This was accomplished by placing a coarse grid about 9 inches upstream of the third elbow. The grid consisted of 4 wood strips across the section with dimensions of 0.75 by 3 inches and the largest dimension perpendicular to the flow. Two of the strips were vertical and two horizontal and were crossed at the quarter points. Turbulence levels were measured 15 inches upstream of the honeycomb, between the two honeycombs, 4 inches downstream of the second honeycomb, and at the entrance of the test section. The data for the mean and rms longitudinal velocity components are shown in Figs. 49 and 50. The lower abscissa scale is the mean velocity normalized by the mean centerline velocity and the upper abscissa scale is the turbulence intensity. Note that the values for turbulence intensity in the test section should be divided by 100. The ordinate is the dimensionless distance measured from the bottom inside surface of the tunnel.

The velocity profiles upstream of the honeycomb and at the test section entrance are shown in Fig. 49. The effect of the turbulence generator near the bottom can be seen. It is more evident here than at the top as the bar is closer to the measuring station. The turbulence intensity of the incoming stream is about 10 to 15 percent.

The mean velocity profile at the entrance to the test section is essentially uniform, except that the boundary layer seems to be thicker at the top than the bottom. The turbulence intensity is about 0.15 percent over the top half of the section, increasing to about an average of about 0.22 percent over the lower half.

Profiles taken between the two honeycombs and downstream of the second honeycomb are shown in Fig. 50. The mean velocity profiles at both stations are essentially the same. Again, the velocity defect due to the lower bar is apparent. The turbulence intensity between the honeycombs is about 9 percent and is reduced to about 6 percent downstream of the second honeycomb.

The data were analyzed and the measured integral length scale at the entrance, between and downstream of the honeycomb, was about 4.8 inches. This length was based on the measurements taken at the dimensionless distance of 0.88. Using the curves presented by Lumley and McMahon [5] for a cell Reynolds number of 6300, a cell length to diameter ratio of 24, and the integral scale length to cell length ratio of 0.8, the expected turbulence reduction factor is 0.24. Thus, for an incoming turbulence of 13 percent, the expected turbulence intensity downstream of the honeycomb is about 3 percent. The turbulence generated by the honeycomb itself should be added to this value. From [5].

$$\frac{\bar{u}^2}{\bar{U}^2} = \frac{0.0072}{s/M}$$

and with $s/M = 2.5/0.25 = 10$,

$$\frac{u^2}{\bar{U}^2} = 0.00072$$

Combining the two effects results in a turbulence intensity of $(0.0009 + .00072)^{1/2} = 0.04$ or about 4 percent as compared to the measured 9 percent. If this level is corrected to the upstream face of the second honeycomb by the ratio of 2.5 to 6, the expected intensity is about 6 percent.

It would seem reasonable that the turbulence would be composed of two scales, part from upstream of the first honeycomb and part from the turbulence generated by the honeycomb itself. The part from upstream would have the same scale as before (4.8 in) and the turbulence generated by the cells a scale approximately equal to the cell size (0.25 in). A length scale ratio of 0.8 will be used which results in a turbulence reduction factor of 0.24 as before. The exit turbulence intensity, based on the measured incoming level of 9 percent, is about 2 percent. To this is added the turbulence generated by the honeycomb and translated to the measuring station 4 inches downstream of the honeycomb $(s/M) = 16$, the calculated intensity is about 3 percent as compared to the measured 6 percent.

The turbulence reduction by the contraction is determined by assuming the decay length of 1/3 the length of the contraction, or 23 inches. The settling length available from the downstream face of the honeycomb to the contraction entrance is 10 inches, resulting in a total decay length of 33 inches. Using the incoming intensity of 6 percent, the effect of decay length is $0.0036 \times 4/33 = .00045$.

From Batchelor [6], the reduction of mean square turbulent velocity ratios due to the contraction ratio is given by the factor

$$\frac{\mu + 2\nu}{3c^2}$$

where $\mu = 0.25$ and $\nu = 3$ for a contraction ratio, c, of 4. This gives a value of 0.13, so that the expected intensity in the test section is the square root of $0.00045 \times 0.13$ or 0.0077. The measured turbulence intensity was about 0.0015 or approximately five times lower than that predicted. This was much better than expected, and no explanation can be offered as to the better performance of the contraction unless noise contamination was present in the plenum measurements. Some estimates made assuming that the only turbulence remaining is that self-generated by the honeycomb indicate an expected intensity of about 0.3 percent, closer to the value observed.

## D. HEAD LOSSES

### 1. Main Diffuser

The headloss coefficient for the full scale main diffuser at maximum test section velocity has been previously estimated [1] to be 0.092. This value consisted of two components; a form loss (0.048) and a friction loss (0.044). The friction loss is a function of Reynolds number. For the air model tests, the Reynolds number was about 19 times less, and therefore the friction coefficient is higher. At the model Reynolds number, the friction factor is about 0.012, whereas the full-scale friction factor was 0.0095. The model friction loss coefficient is thus about 0.056. The measured pressure coefficient was 0.69, and the associated total headloss coefficient is about 0.12. The measured form loss is the difference between the total and the calculated friction loss or 0.064. Adding to this value, the calculated full-scale friction loss (0.044) results in a total loss coefficient of 0.108, which is quite close to the originally estimated 0.092 for the full-scale Reynolds number.

### 2. Elbow No. 1

Measurements were made of the pressure drop across the first elbow with the contoured vanes installed at their design angle. The pressures were measured at both the inside and outside of the tunnel walls. Pressure drops were small, on the order of 0.1 inches of water. Four measurements were taken and the calculated local loss coefficient varied from about 0.09 to 0.15, with an average of 0.11. This value is less than the loss coefficient of 0.14 used in the earlier report [1]. However, when multiplied by the local velocity head, the reduction in the head loss is only about 0.04 m. Therefore, the original value will be used to account for some of the variability.

### 3. Summary of Losses

The summary of the headlosses predicted for the full-scale HYKAT operating at a test section velocity of 11.5 m/s is given in Table 3. This includes the acoustic grids in the downcomer and upcomer. Computations were carried out in a manner similar to that described in the previous report [1].

TABLE 3

Summary of Component Headlosses

| Component | Pertinent Local A($m^2$) | Pertinent Local V(m/s) | Local $K_\ell$ | $H_\ell$(m) |
|---|---|---|---|---|
| Test Section | 4.48 | 11.5 | 0.046 | .310 |
| Main Diffuser | 4.48 | 11.5 | 0.108 | .727 |
| First Elbow | 10.30 | 5.00 | 0.14 | .178 |
| Acoustic Grid | 10.30 | 5.00 | 0.11 | .28 |
| Downcomer Diffuser | 10.30 | 5.00 | 0.015 | .019 |
| Second Elbow | 11.97 | 4.30 | 0.14 | .132 |
| Transition | 11.97 | 4.30 | 0.013 | .012 |
| Leg Upstream of Pump | 11.95 | 4.31 | 0.014 | .013 |
| Contraction Upstream of Pump | 11.95 | 4.31 | 0.004 | .004 |
| Diffuser Downstream of Pump | 11.19 | 4.60 | 0.06 | .065 |
| Large diameter leg downstream of pump | 17.94 | 2.87 | 0.020 | .009 |
| Contraction/Transition | 17.94 | 2.87 | 0.012 | .005 |
| Third Elbow | 17.89 | 2.88 | 0.14 | .059 |
| Upcomer | 17.89 | 2.88 | 0.015 | .006 |
| Acoustic Grid | 17.89 | 2.88 | 0.12 | .101 |
| Fourth Elbow | 17.89 | 2.88 | 0.14 | .059 |
| Honeycomb | 17.89 | 2.88 | 1.60 | .549 |
| 4:1 Contraction | 17.89 | 2.88 | 0.02 | .008 |
| | | | $\Sigma H_L$ = | 2.54 m |

# V. CONCLUSIONS

1. The diffuser performance is very sensitive to Reynolds number and the inflow velocity profile. The flow is likely to be at or near a separation condition when the Reynolds number is equal to that of the physical modeling and when there is a slight asymmetry in the inflow velocity profile. Flow separation is unlikely at the prototype Reynolds number unless there is a substantial amount of inflow velocity asymmetry.

2. The turning vanes, when set at the proper angle, turn the flow perfectly without altering the velocity profile. The turning vanes may be set at other angles in order to change the velocity profile provided that the elbow is followed by a sufficiently long, straight section. For a given inflow velocity profile measured in the physical model, an optimum–velocity distribution at the pump inlet at the prototype Reynolds number may be produced by underturning the guide vanes in the second elbow uniformly by 1.5 degrees.

3. The calibrated mathematical models of the main diffuser and guide vanes were used to extrapolate the pump inlet profile measured in the physical model to the prototype condition. Because of the Reynolds number effect on diffuser performance, the prototype should perform better than the model.

4. Boundary pressures measured along the longitudinal centerline of the bottom surface of the contraction compared favorably with those calculated with the math model.

5. Mean velocity profiles measured at various locations between the contraction and pump inlet in a vertical plane indicated a non–symmetry, with a deficiency in velocity towards the outside of the flow circuit. This asymmetry originated at the exit of the main diffuser. Profiles were essentially symmetric in a horizontal plane.

6. Installation of a honeycomb with hexagonal cells upstream of the contraction generally improved the overall flow performance. Calculations of the reduction in turbulence intensity by the honeycomb predicted more reduction than measured. However, the measured reduction by the contraction was better than predicted.

7. Attachment of a ship model provided by HSVA to the top surface of the test section at midlength did not degrade the overall performance of the system. Only local effects were observed on the inflow and exit flow of the main diffuser.

## REFERENCES


1. Song, Charles C. S. et al., "Hydrodynamic Analysis of the HYKAT," St. Anthony Falls Hydraulic Laboratory, University of Minnesota, Project Report No. 261, June 1987.

2. Deardorff, J. W., "A numerical study of three–dimensional turbulent channel flow at large Reynolds number," *J. Fluid Mechanics*, Vol. 41, Part 2, 1970.

3. Smagorinsky, J., "General circulation experiments with the primitive equations. I. The basis experiment," *Monthly Weather Review*, Vol. 91, No. 3, 1963.

4. Schumann, U., "Subgrid scale model for finite difference simulations of turbulent flows in plane channels and annuli," *Jour. Comp. Phys.*, Vol. 18, 1975.

5. Lumley, J. L. and McMahon, J. F., "Reducing water tunnel turbulence by means of a honeycomb," *Trans. ASCE, Jour. Basic Engineering*, Vol. 89, Dec. 1967, pp. 764–770.

6. Batchelor, G. K., *Homogeneous Turbulence*, Cambridge University Press, 1953.

Figures 1 through 50

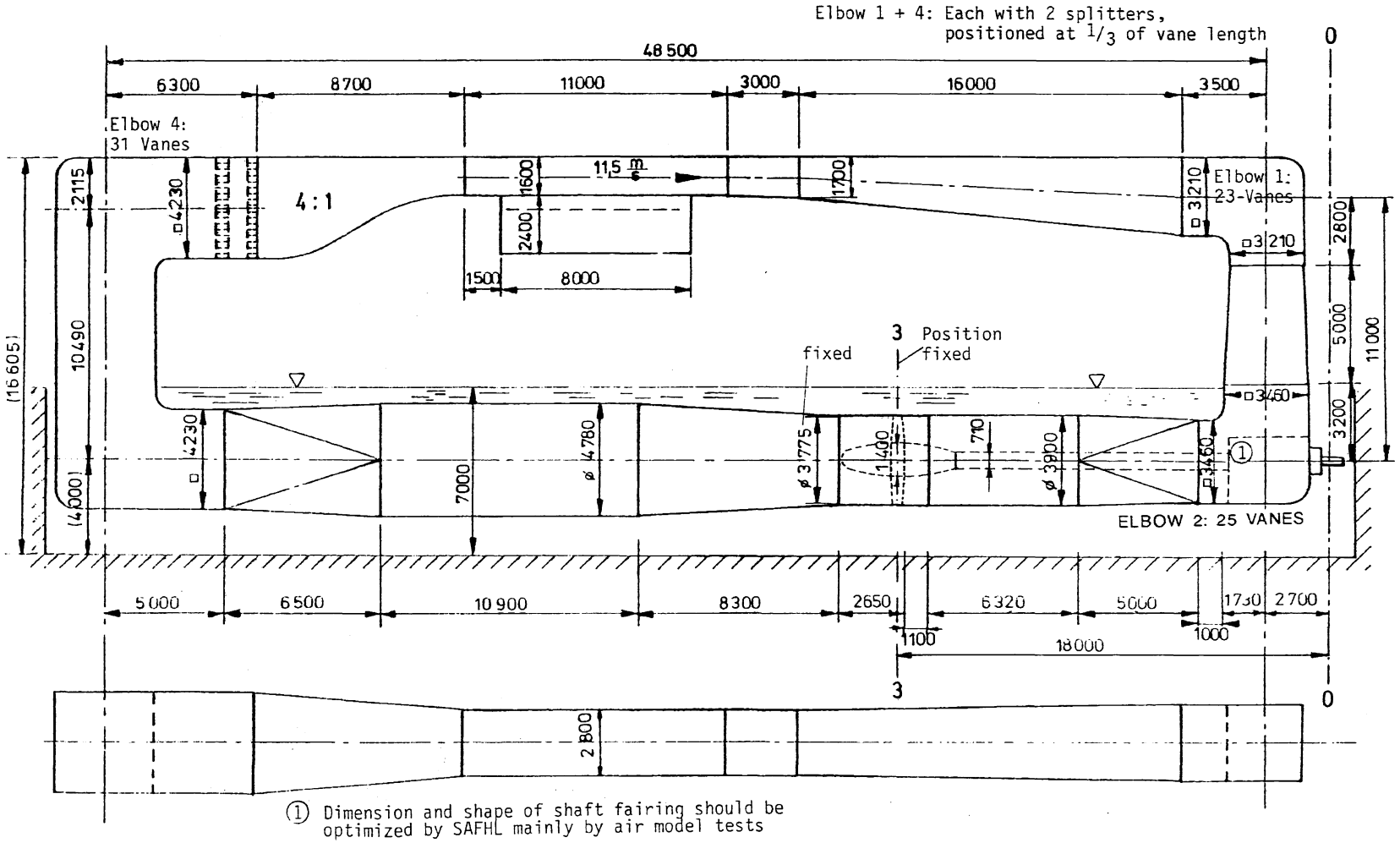


Fig. 1. Configuration of HYKAT.

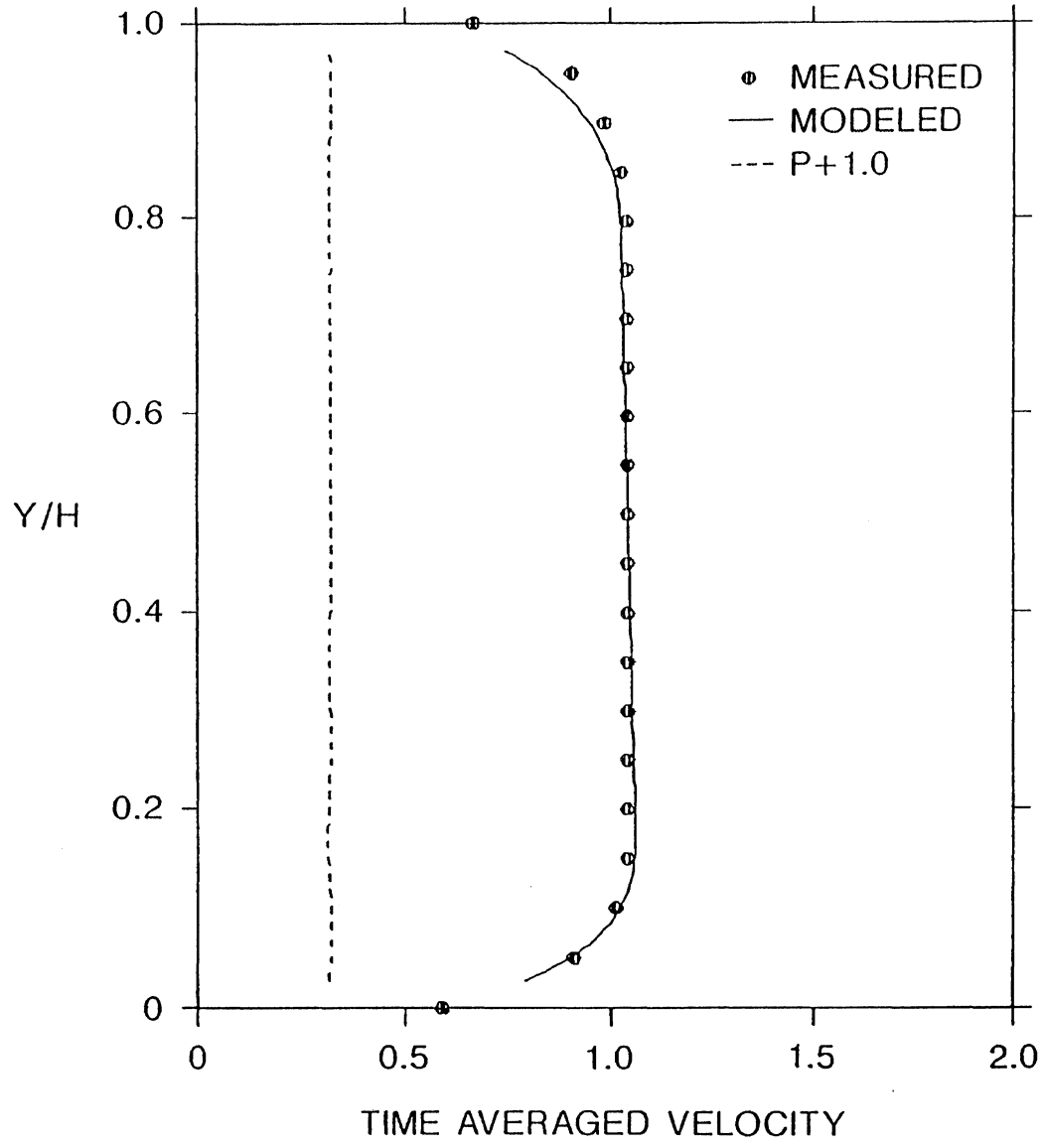


Fig. 2. Asymmetric inlet velocity profile used for the model compared with the base line value.

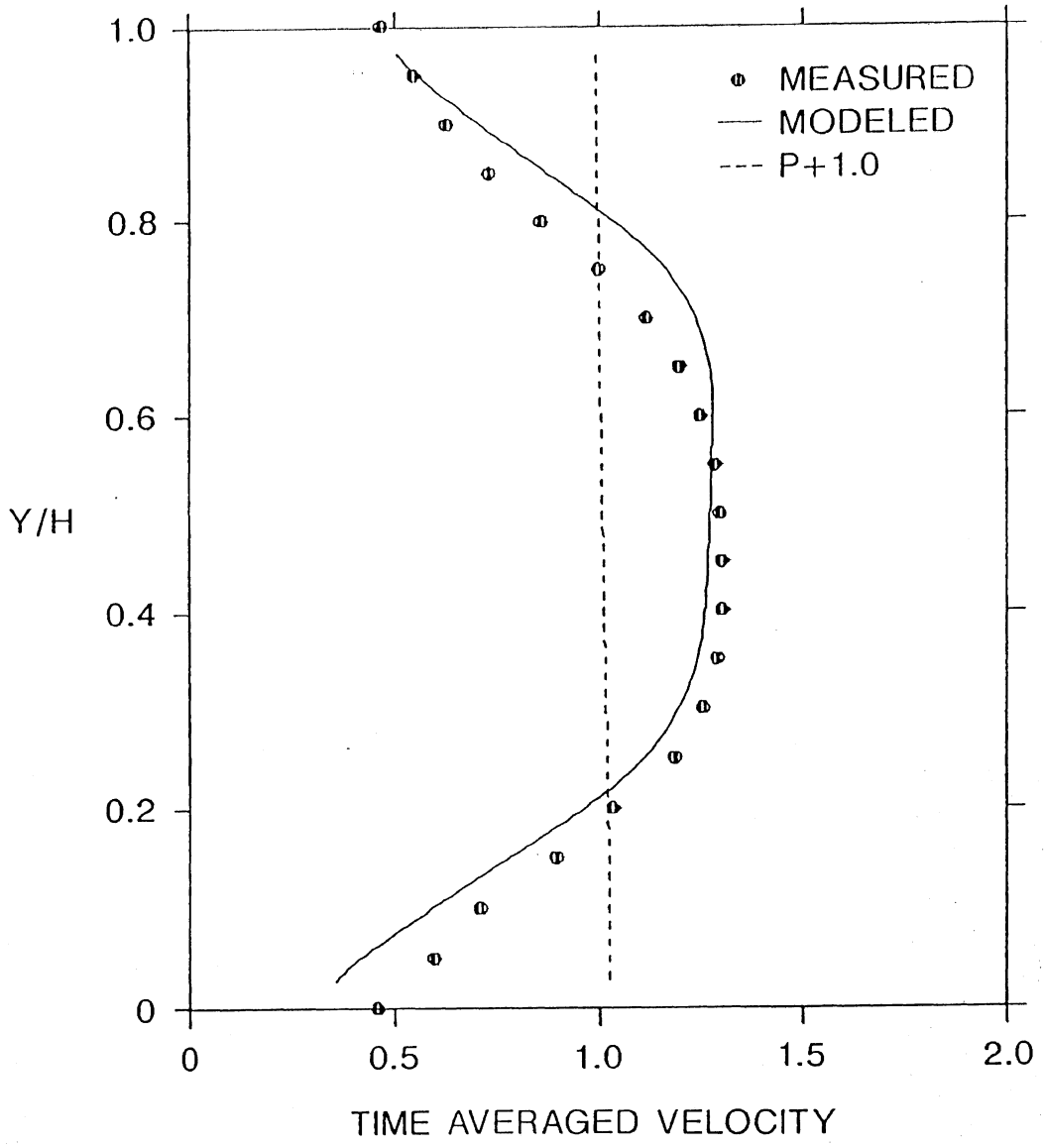


Fig. 3. Comparison of calculated and measured velocity distribution of diffuser exit.

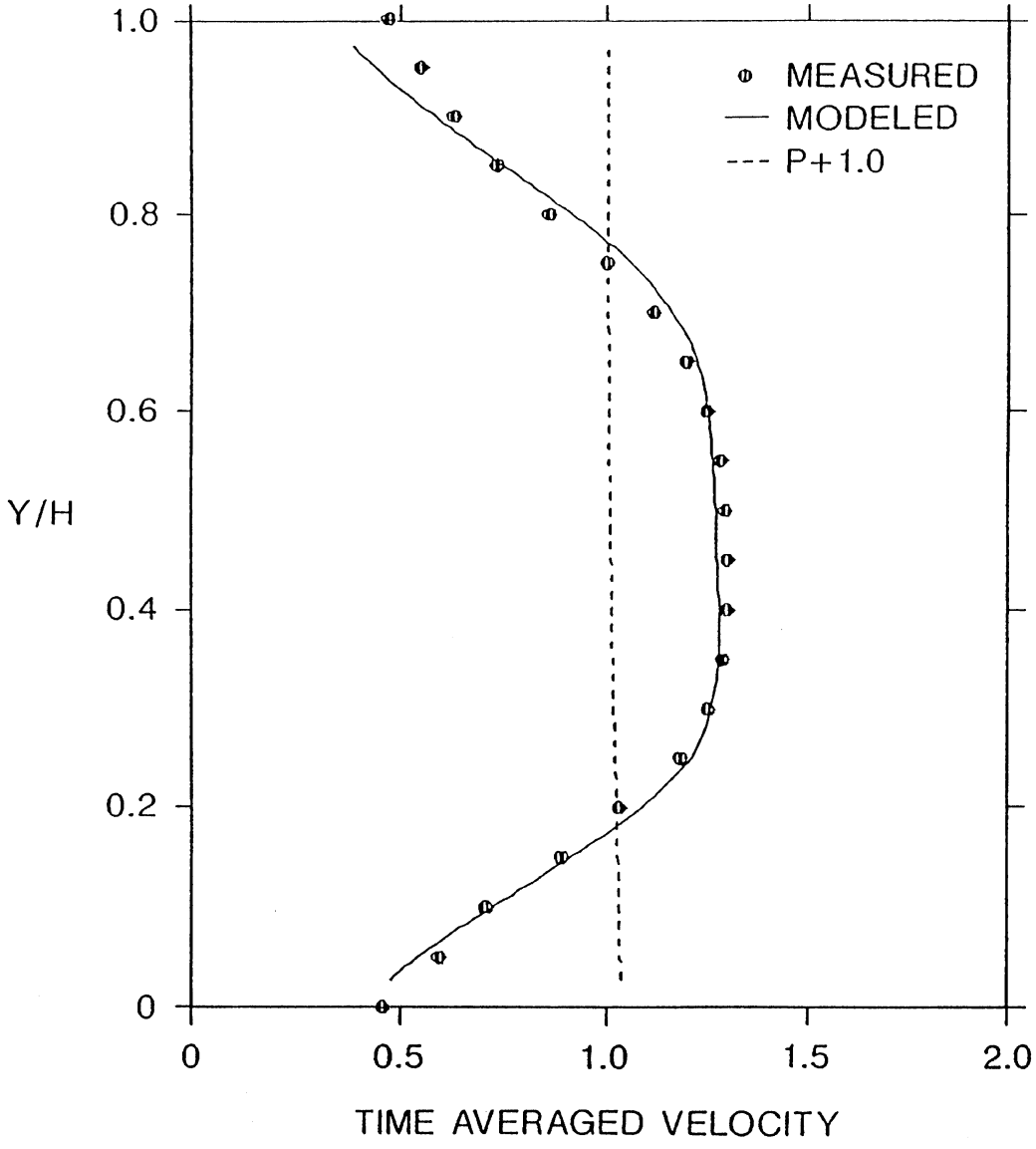


Fig. 4. Comparison of calculated and measured velocity distribution at exit (calculation based on adjusted inflow velocity distribution.

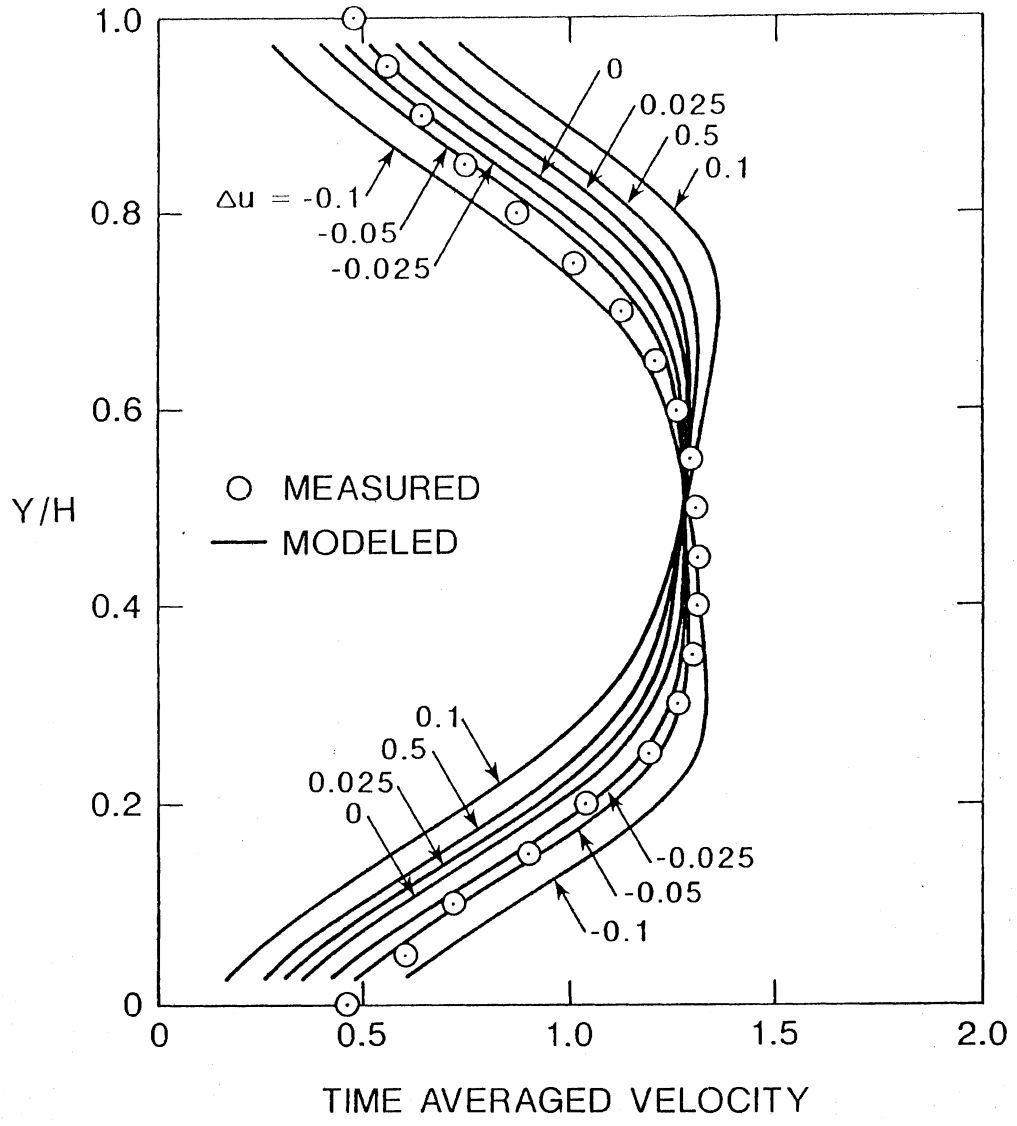


Fig. 5. Exit velocity distributions for various asymmetric inlet velocity profiles.

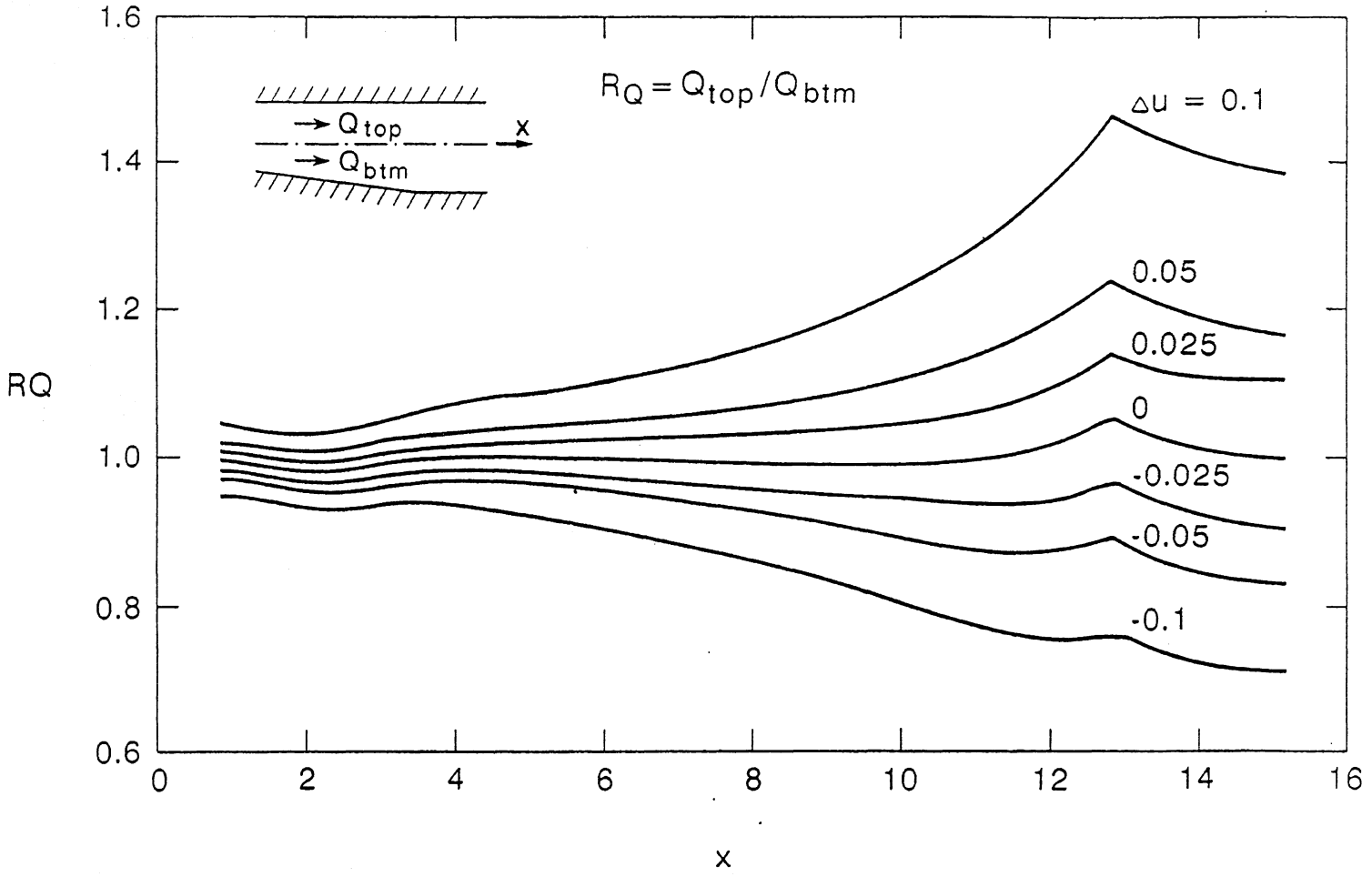


Fig. 6. Variation of RQ along the diffuser for various inlet velocity profiles.

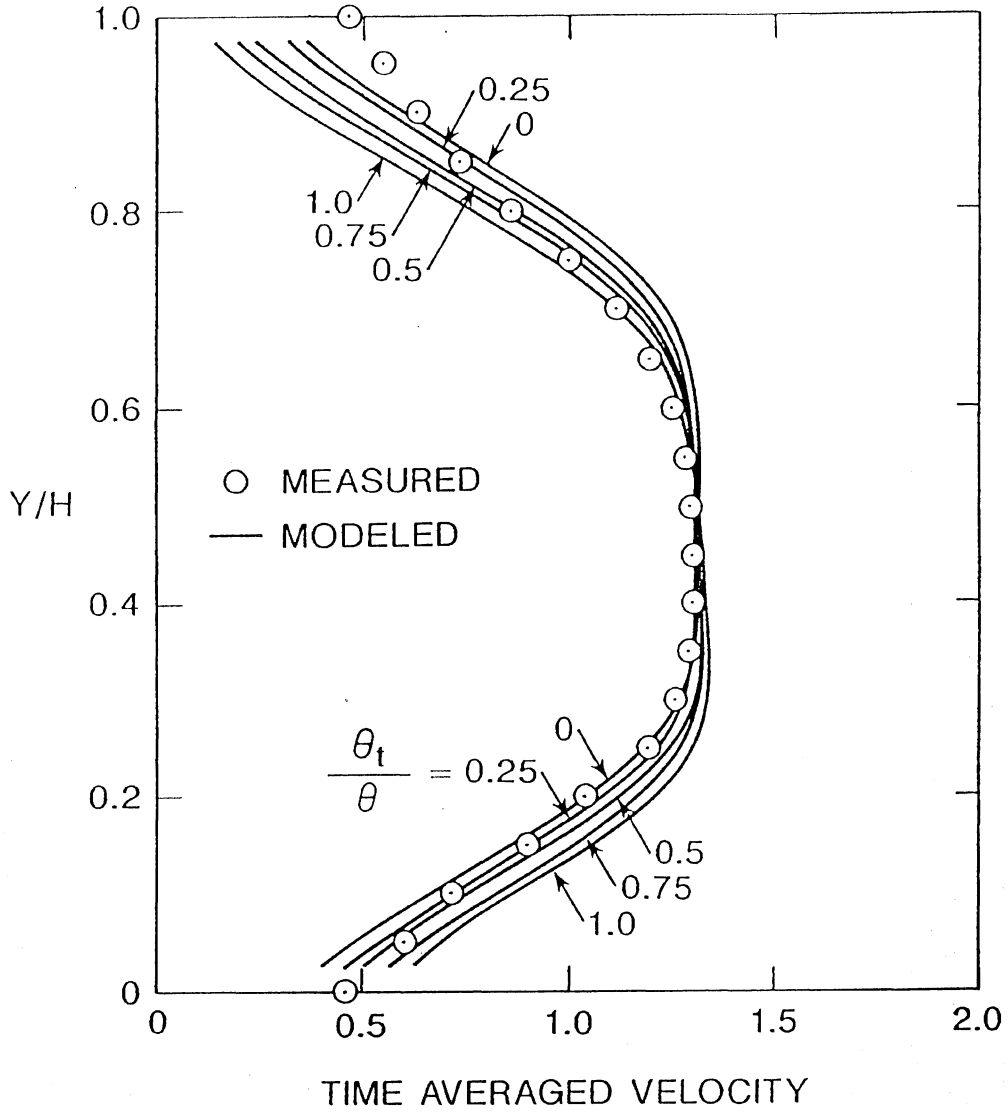


Fig. 7. Effect of diffuser asymmetry on exit velocity distribution.

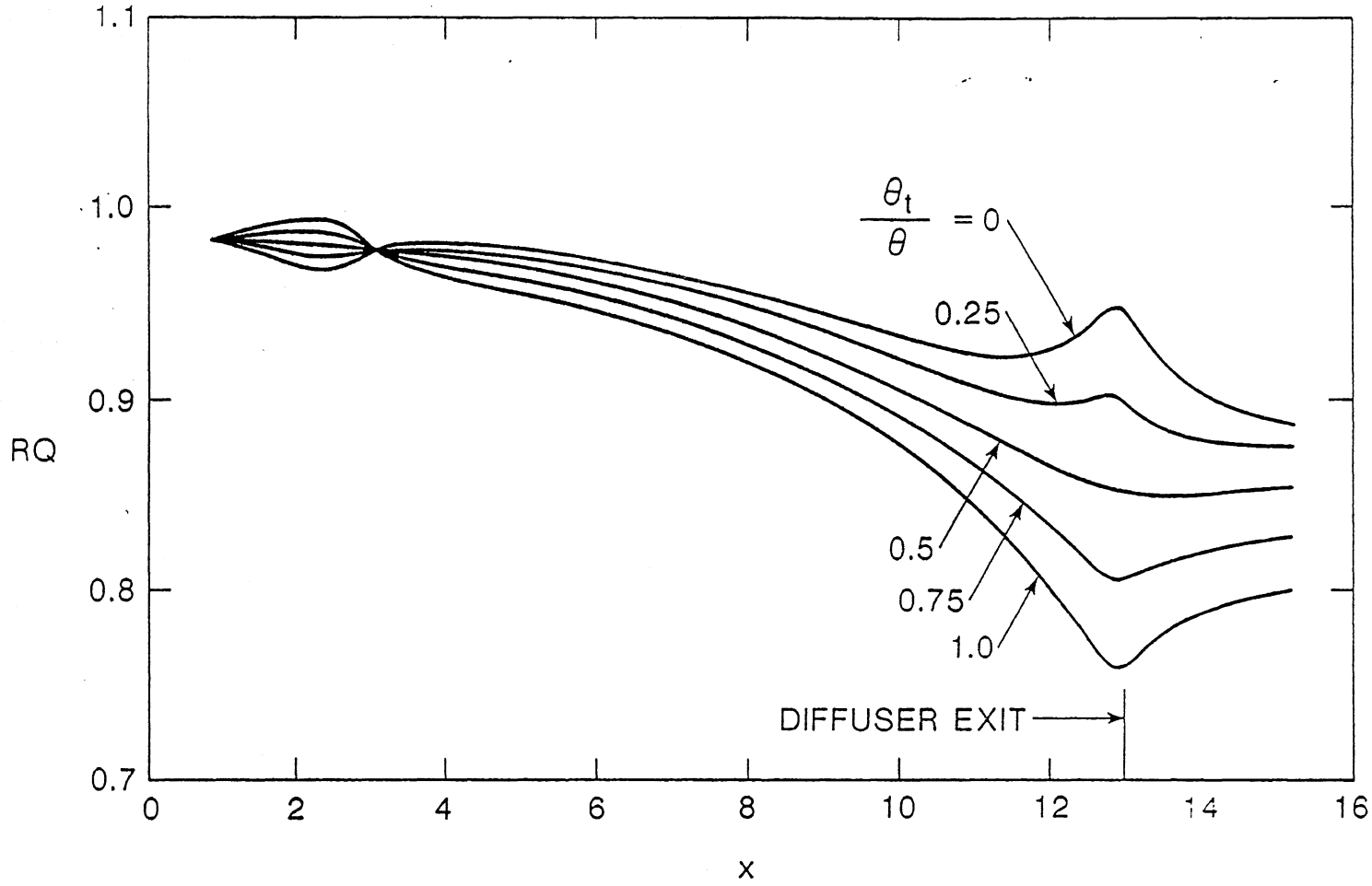


Fig. 8. Effect of diffuser asymmetry on discharge ratio.

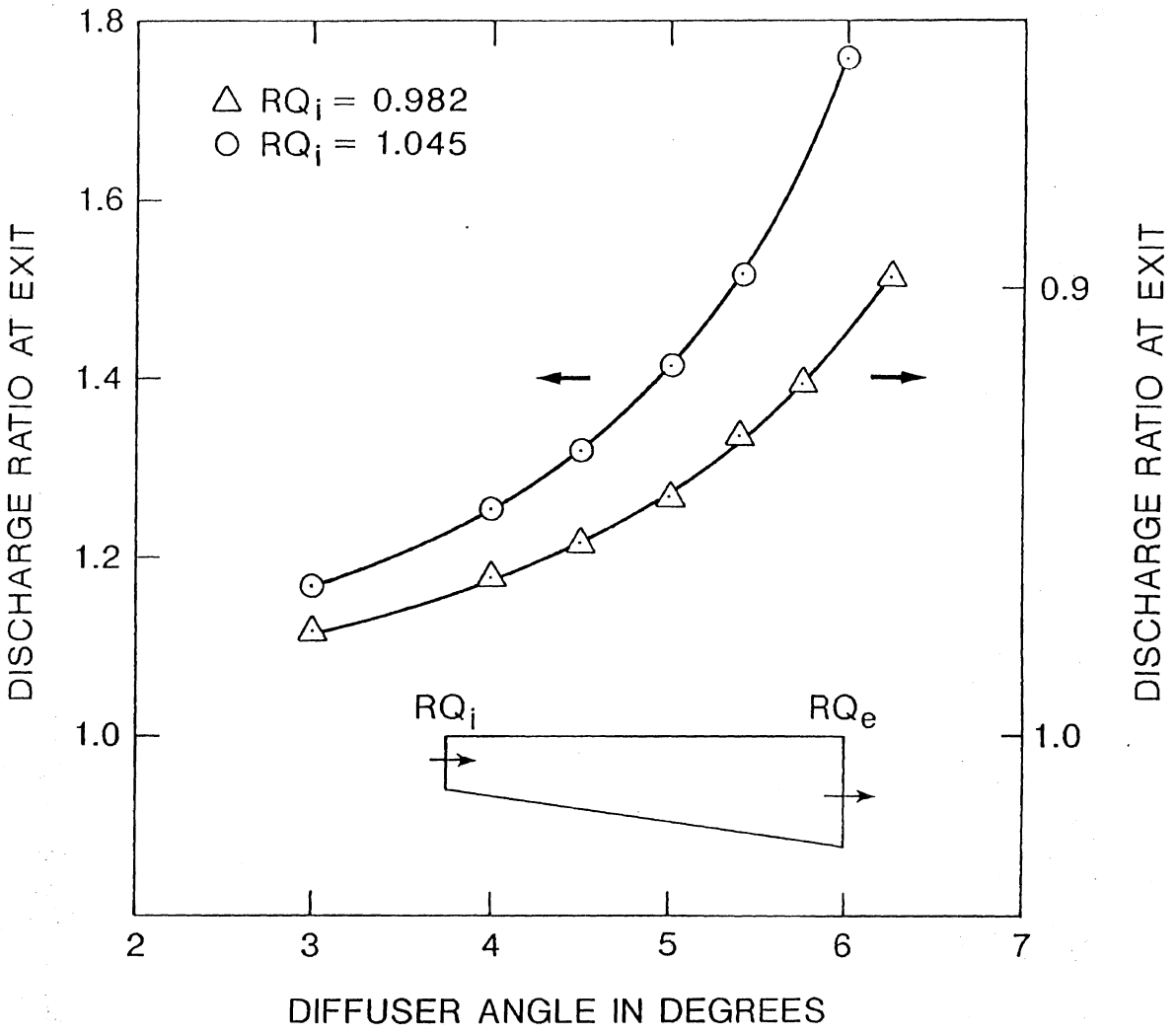


Fig. 9. Effect of diffuser angle on discharge ratio.

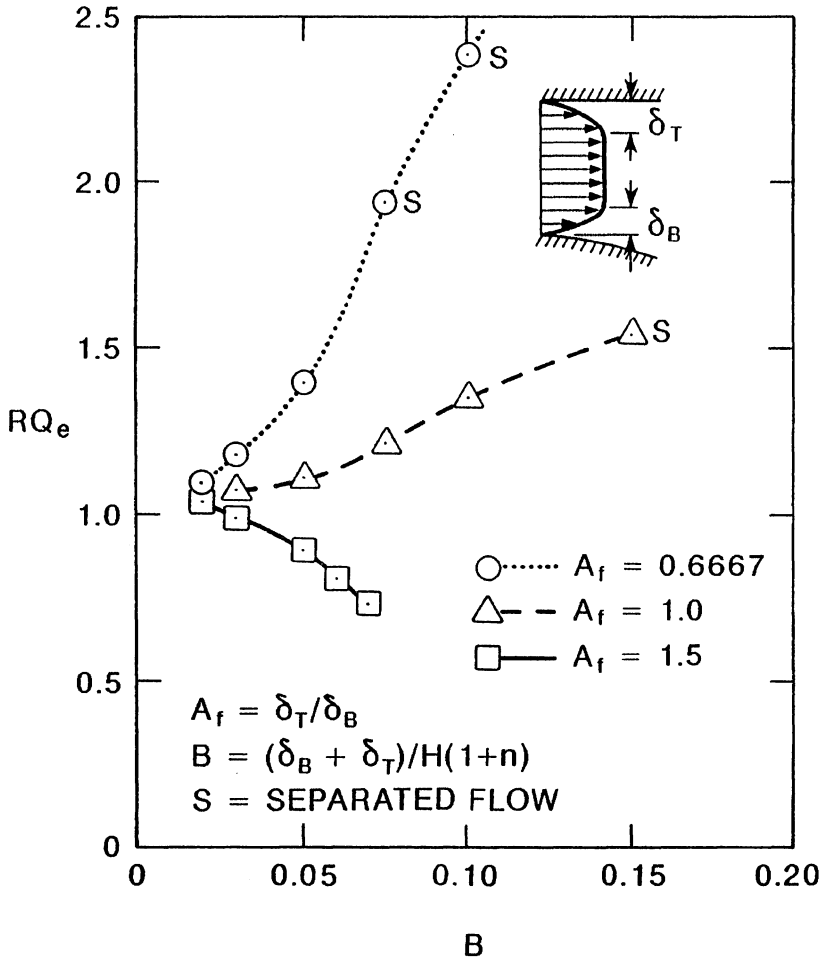


Fig. 10. Blockage effect on diffuser exit discharge ratio.

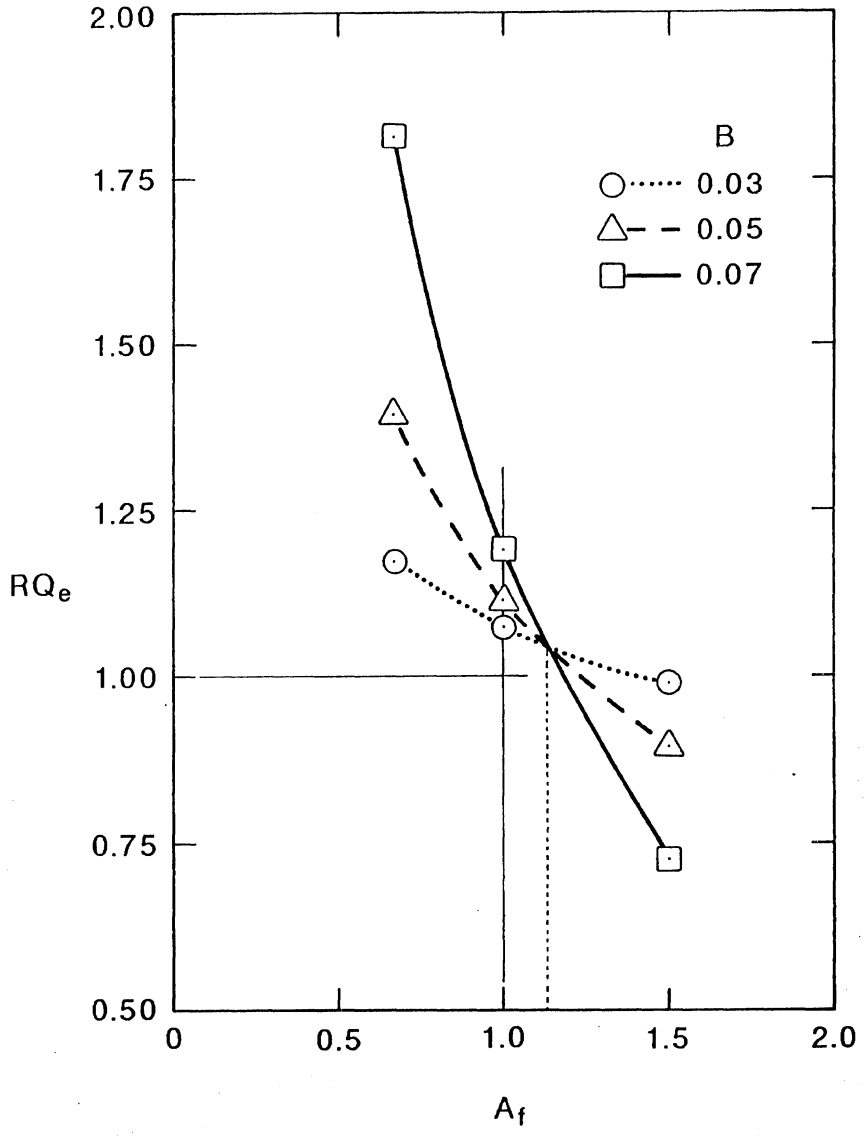


Fig. 11. Effect of asymmetric inflow on diffuser exit discharge ratio.

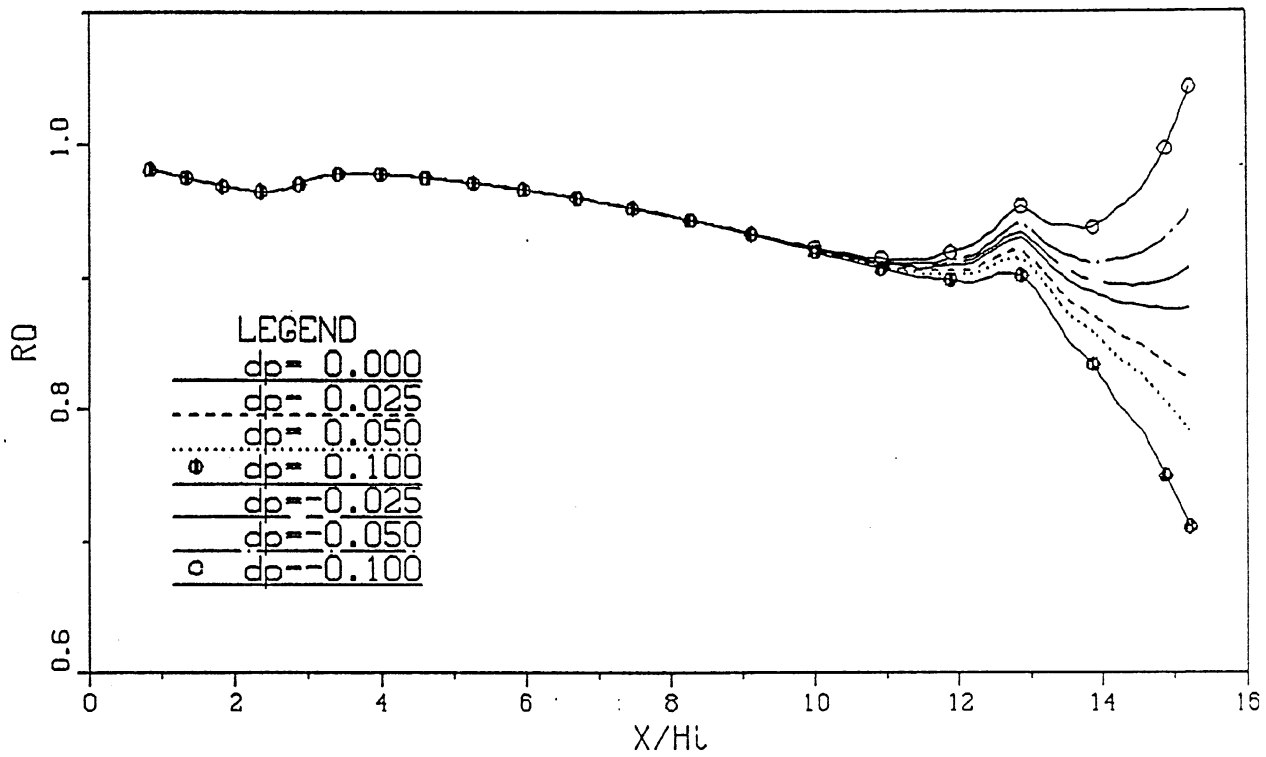


Fig. 12. Effect of nonuniform pressure distribution at exit on diffuser flow quality.

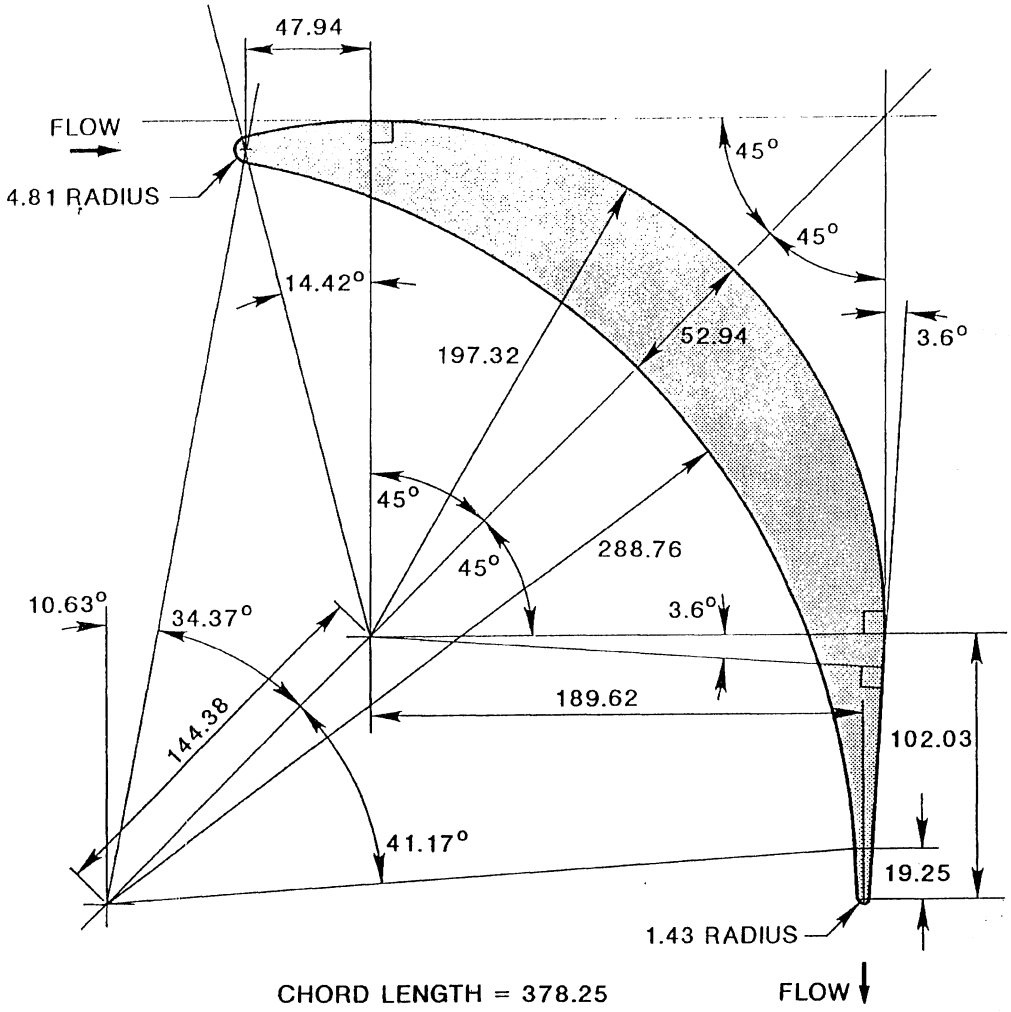


Fig. 13. Contoured tuning vane profile.

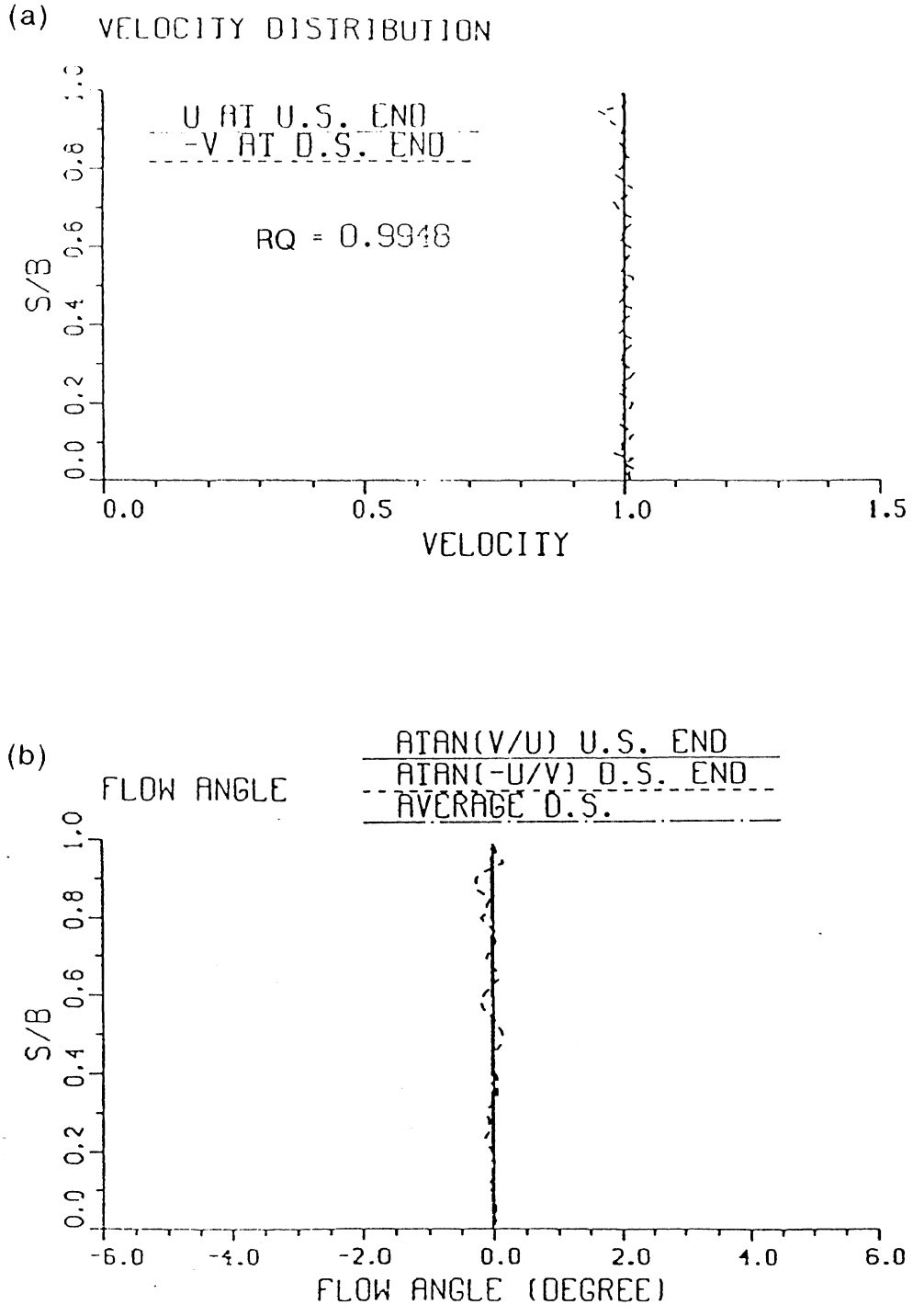


Fig. 14. Computed exit velocity distribution at first elbow.

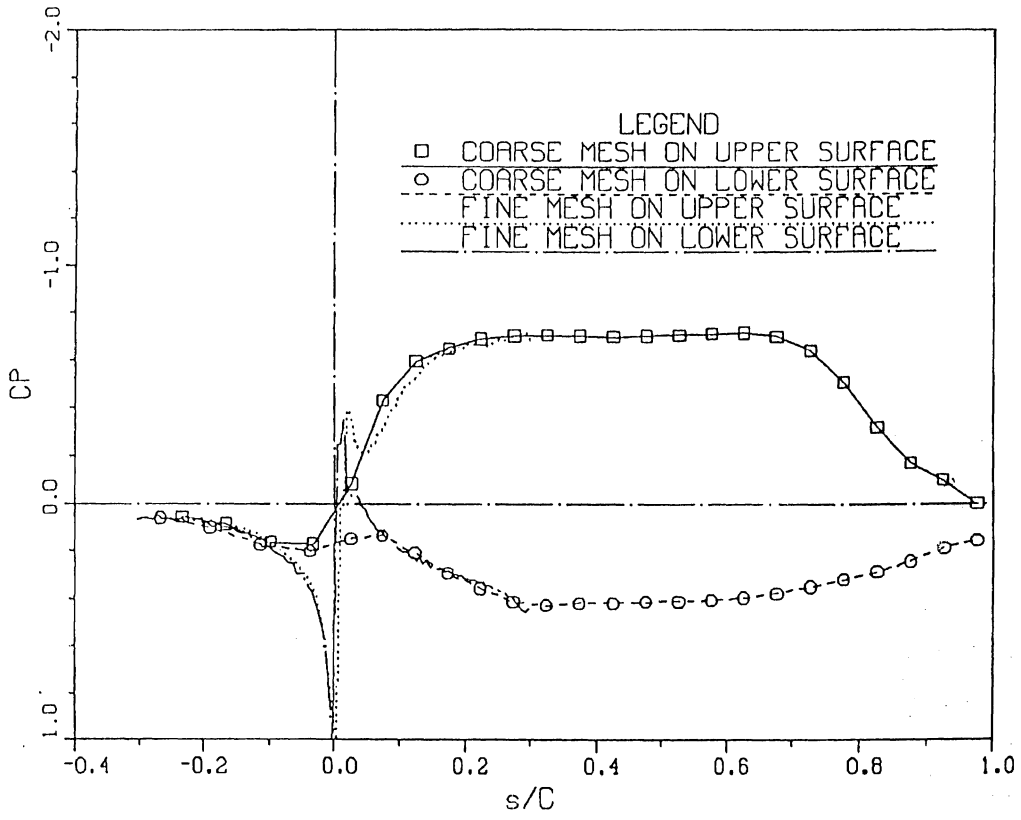


Fig. 15. Pressure distribution on recommended vane, fine mesh result compared with coarse mesh result.

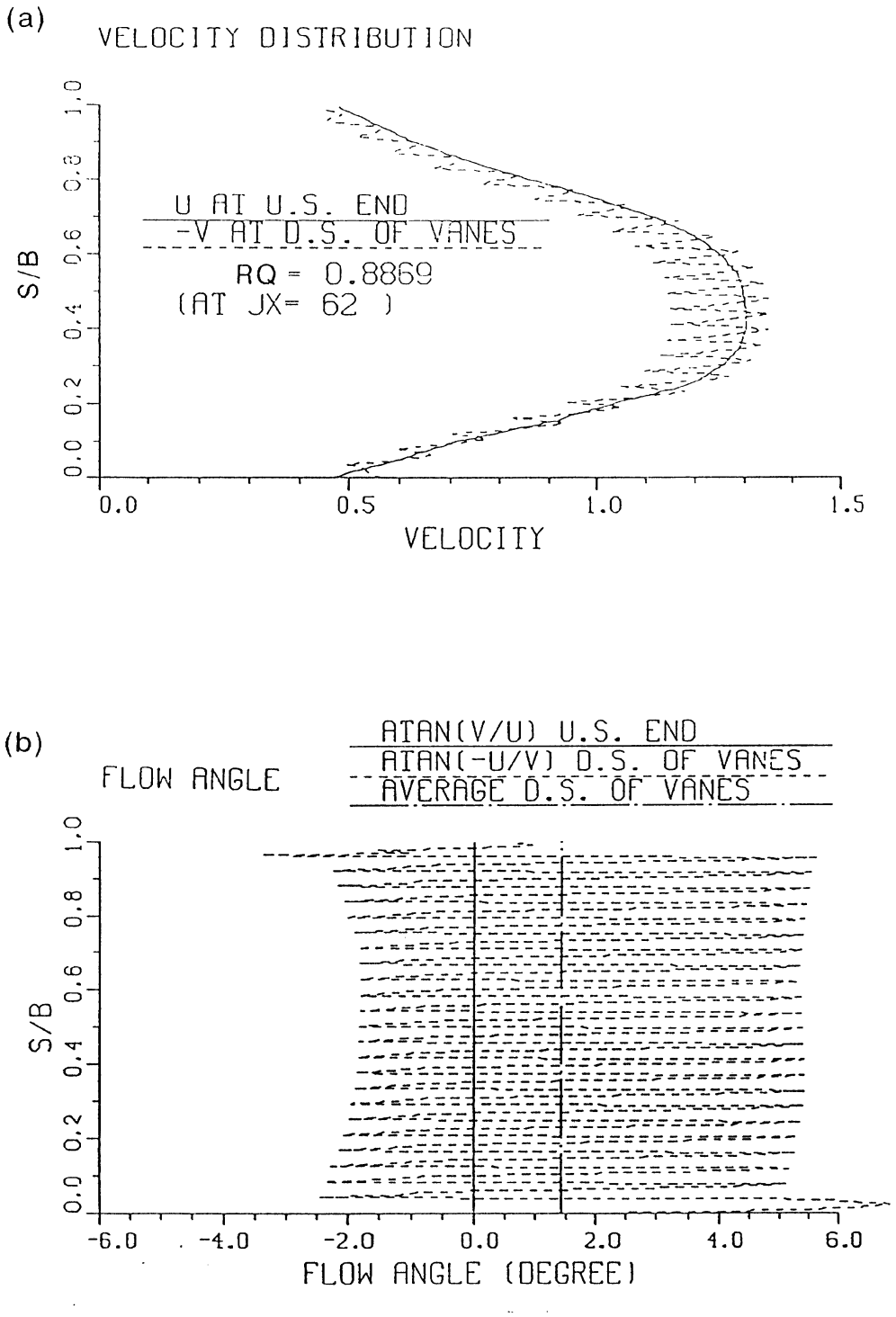


Fig. 16. Velocity distribution at downstream end of guidevanes; vane at normal position.

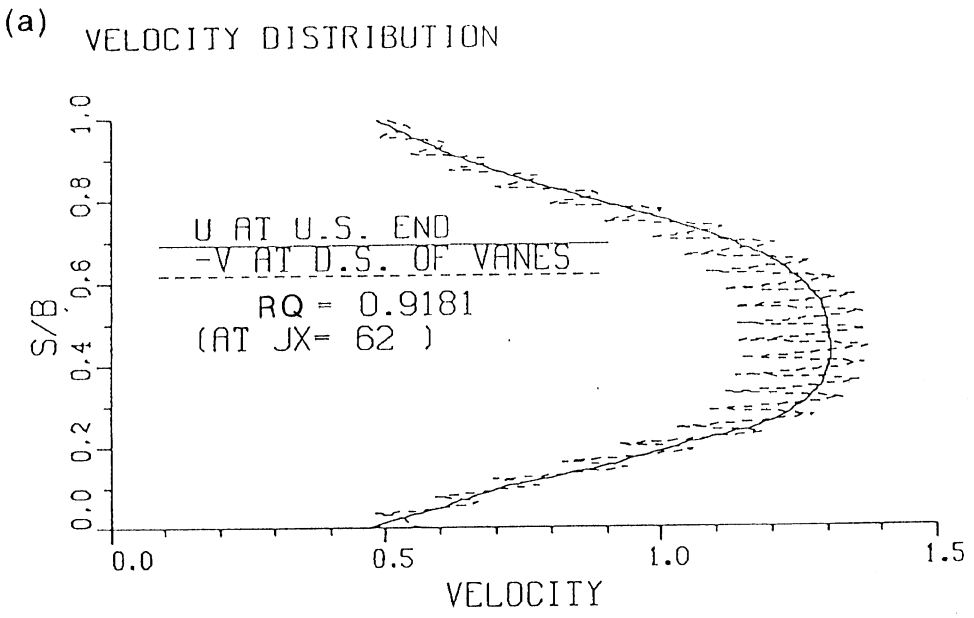


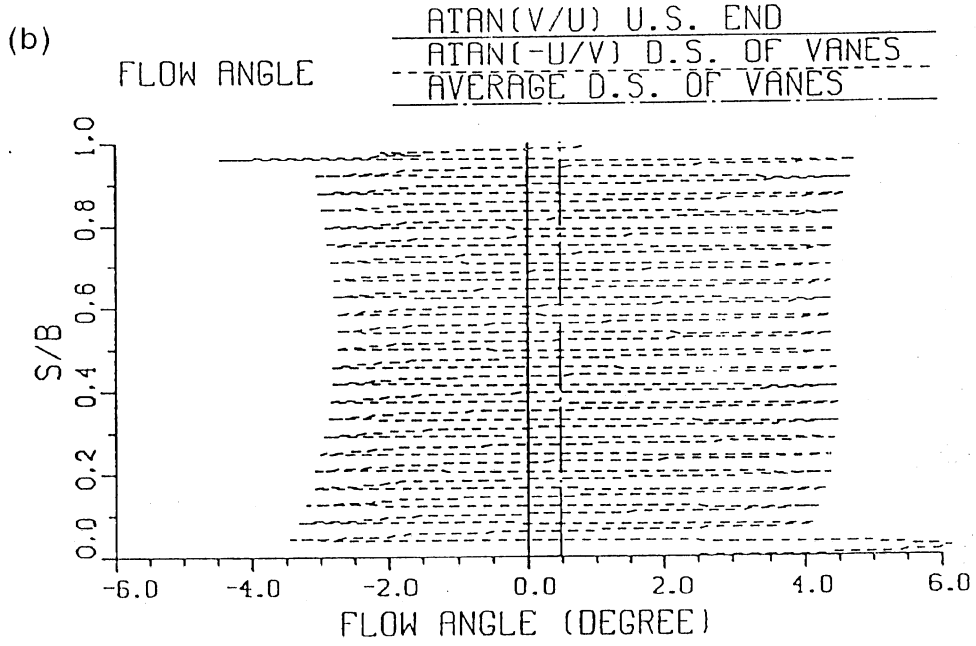


Fig. 17. Velocity distribution at downstream end of guide vanes; vanes at 1 degree overturn position.

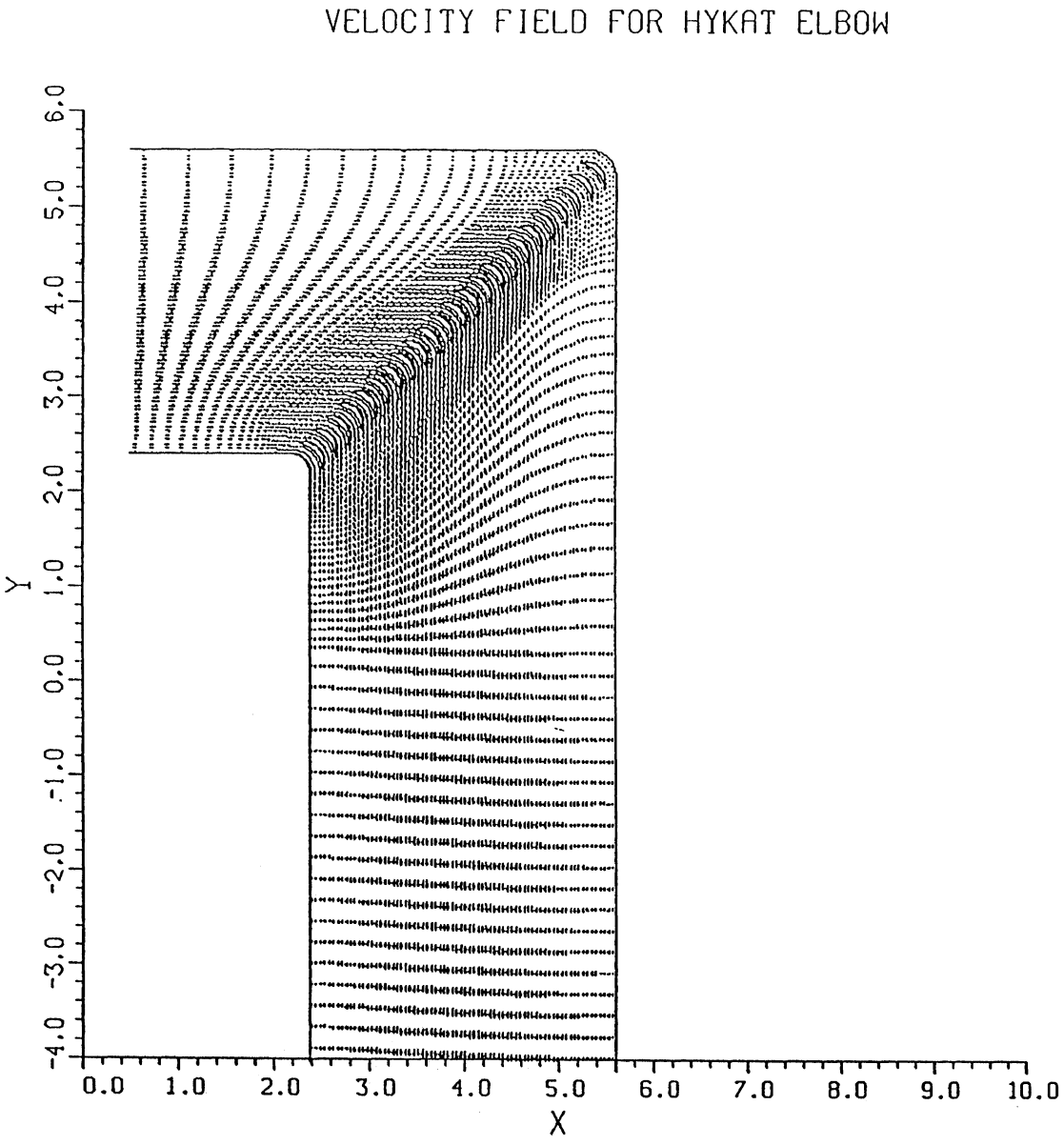


Fig. 18. The geometry and velocity field for HYKAT elbow with extended draft channel.

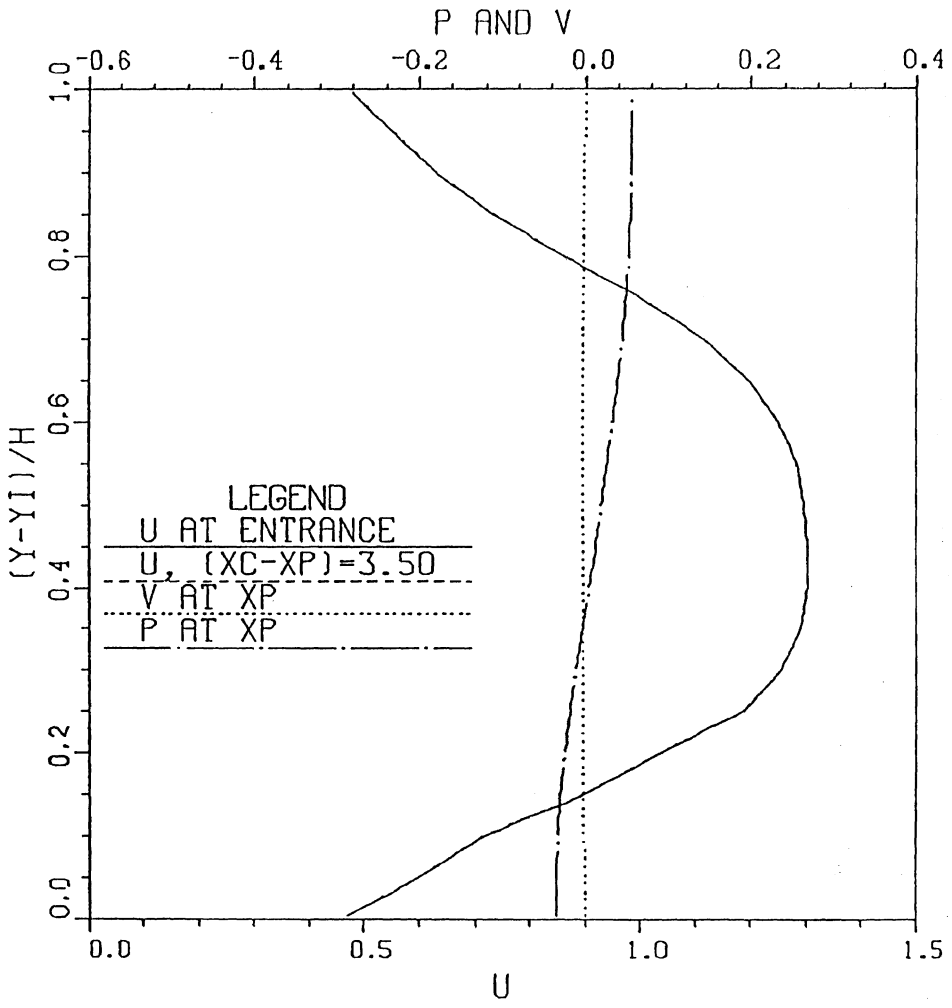


Fig. 19. Velocity (boundary condition) and pressure (calculated) distributions at upstream end, Re = $1.2 \times 10^6$.

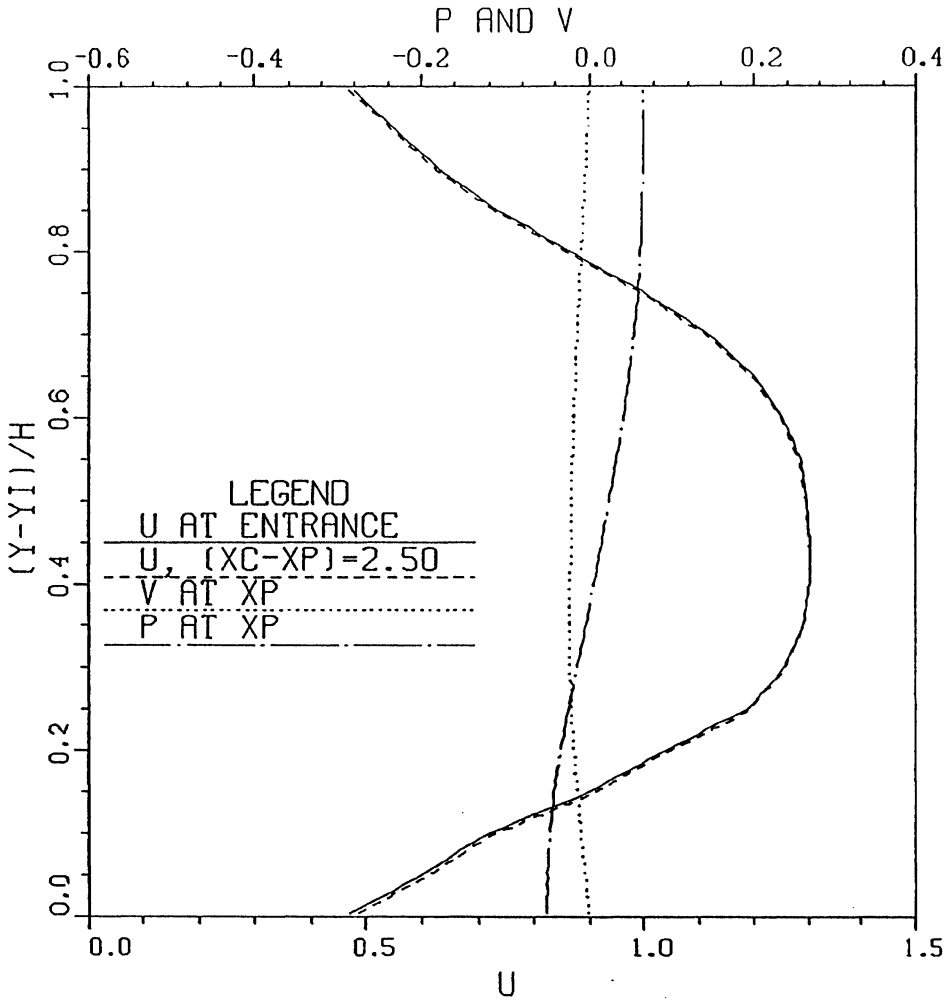


Fig. 20. Calculated velocity and pressure distribution at 1 meter downstream compared with the given velocity distribution at the upstream end.

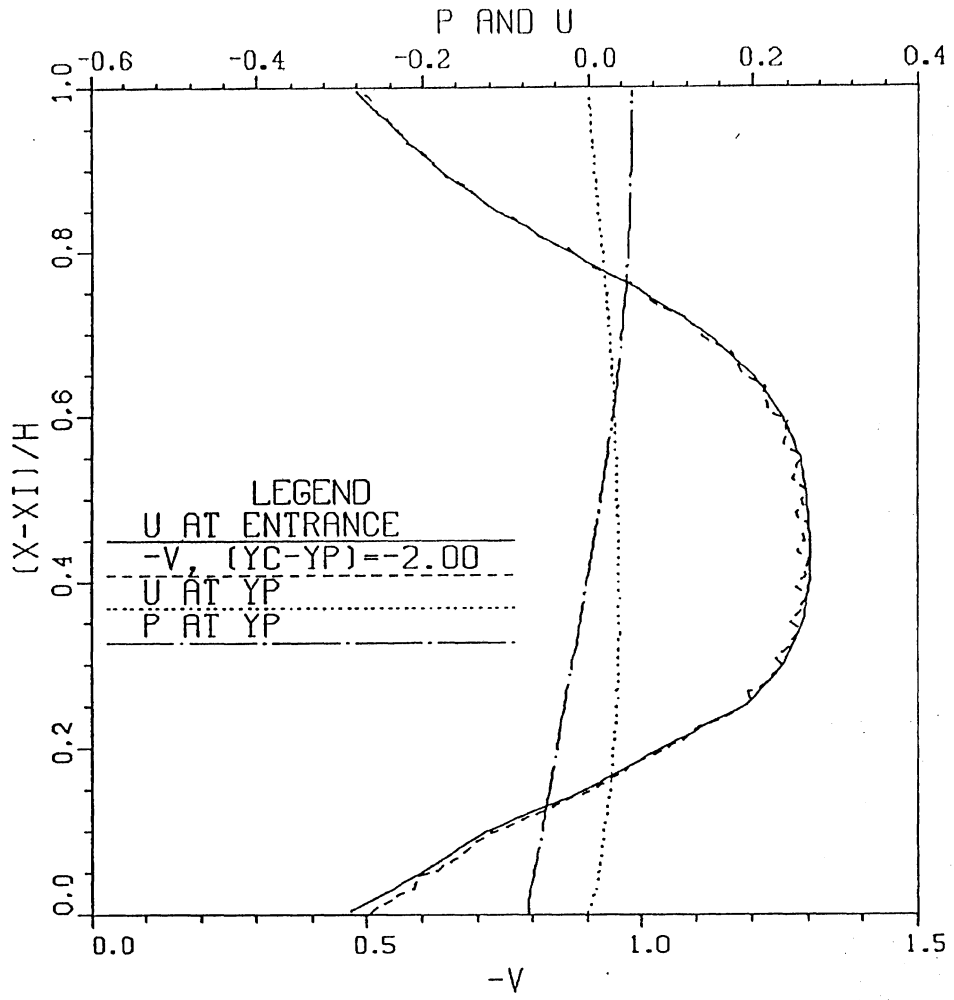


Fig. 21. Velocity and pressure distribution on a cross–section 2 meters downstream of the center of the miter line.

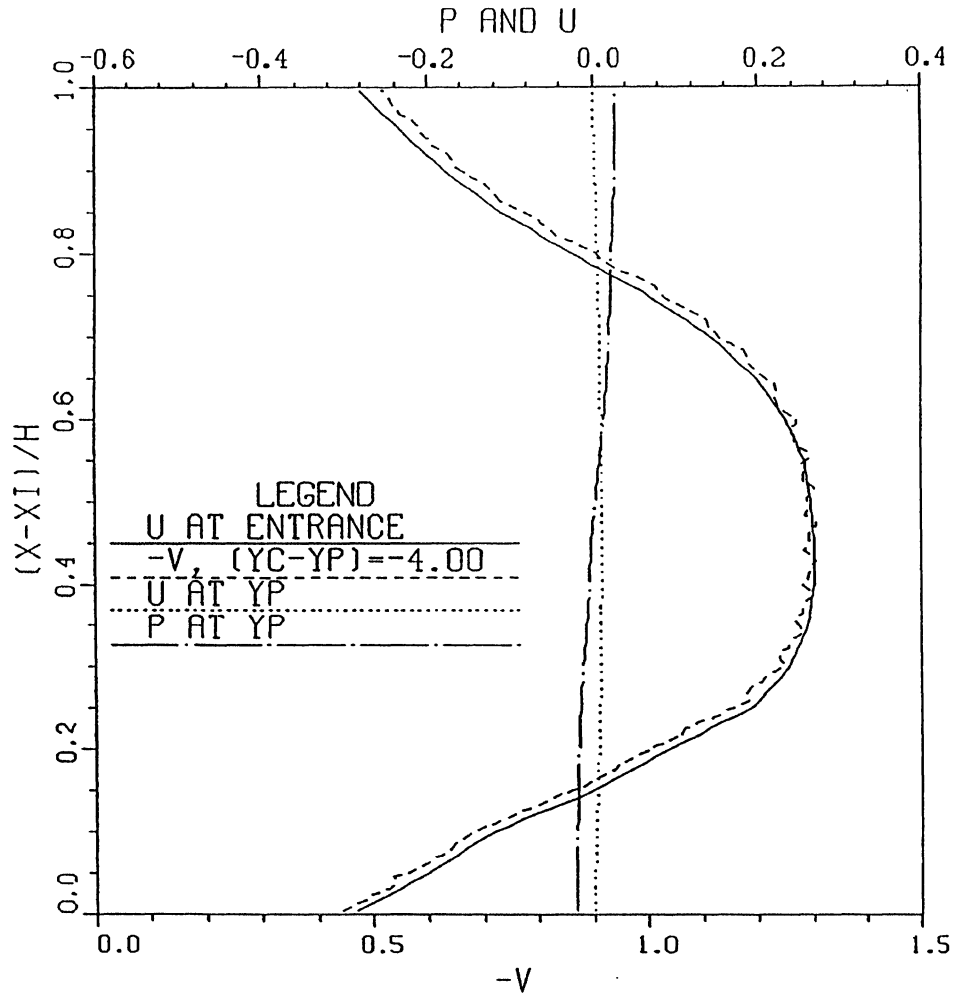


Fig. 22. Velocity and pressure distribution on a cross–section 4 meters downstream of the center of the miter line.

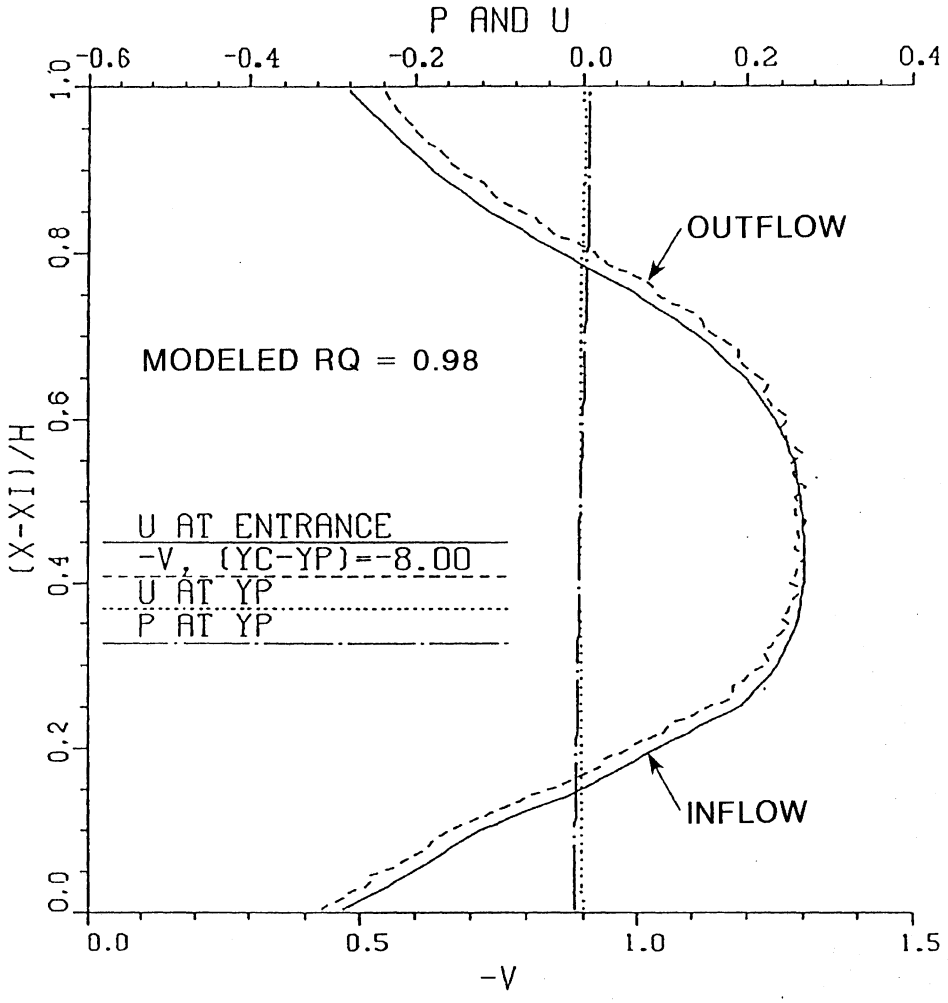


Fig. 23. Velocity and pressure distribution on a cross-section 8 meters downstream of the center of the miter line.

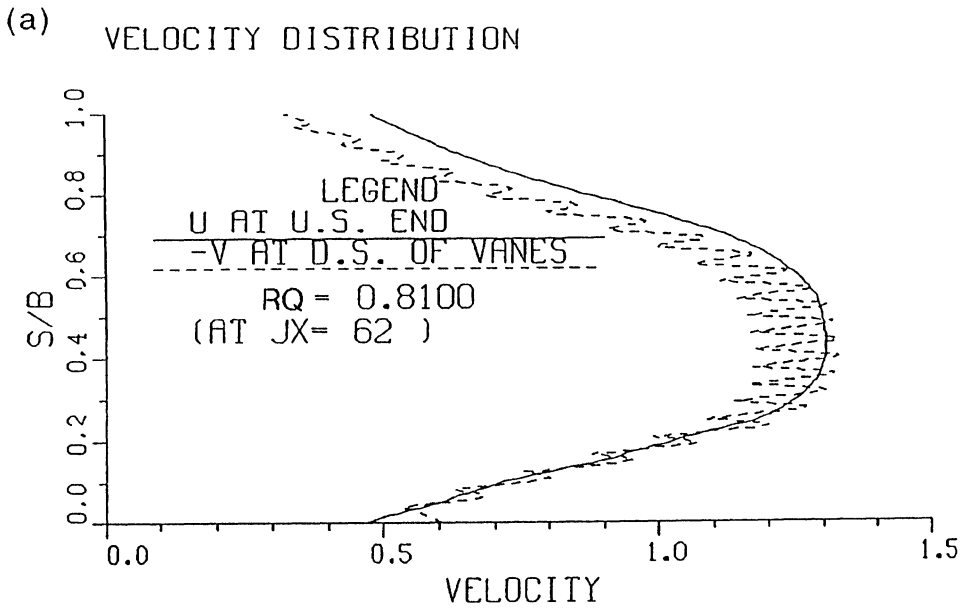


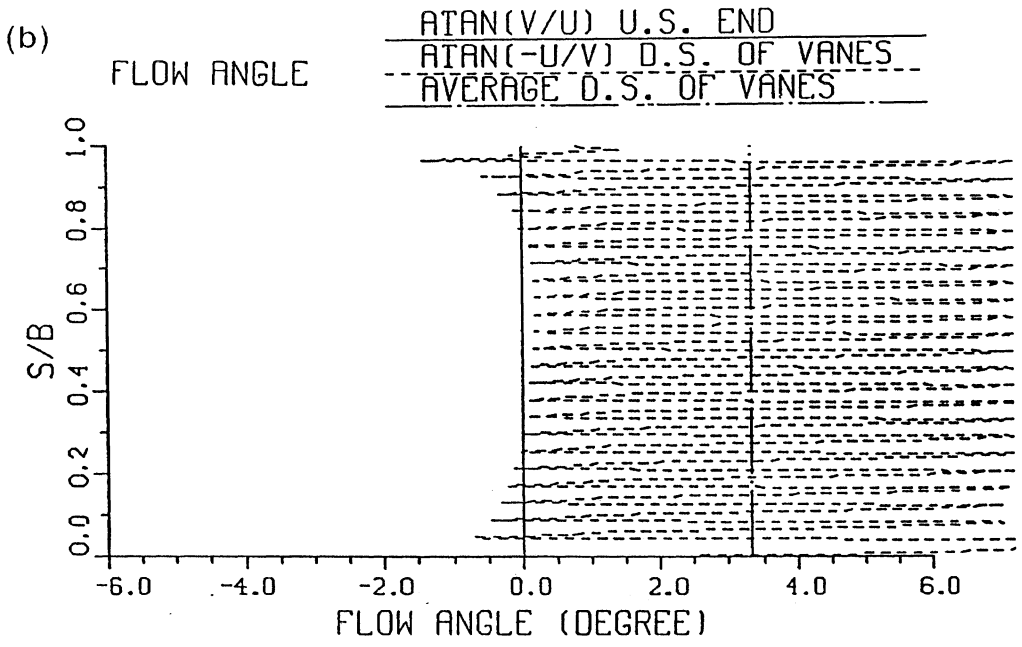


Fig. 24. Velocity distribution, magnitude and direction, on a line parallel to the miter line.

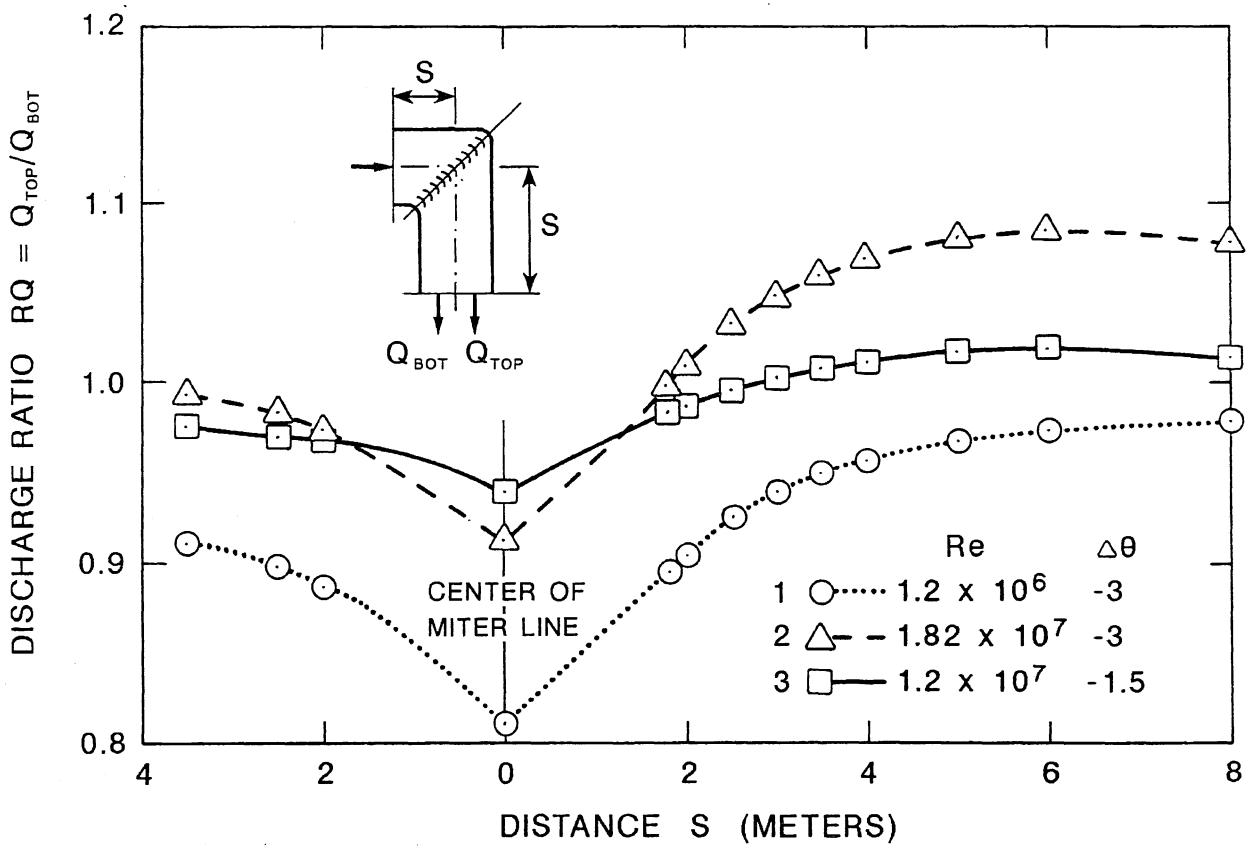


Fig. 25. Variation of discharge ratio.

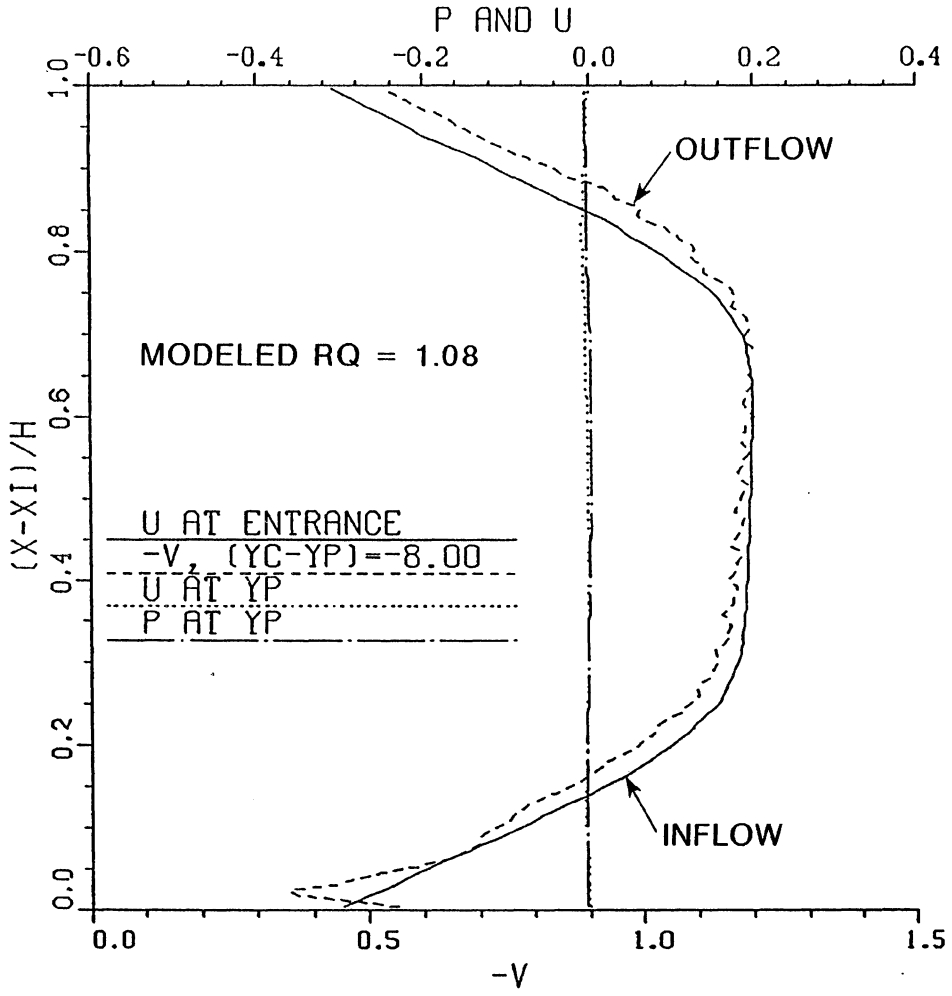


Fig. 26. Velocity and pressure distributions with 3 degree underturning and Re = $1.82 \times 10^7$.

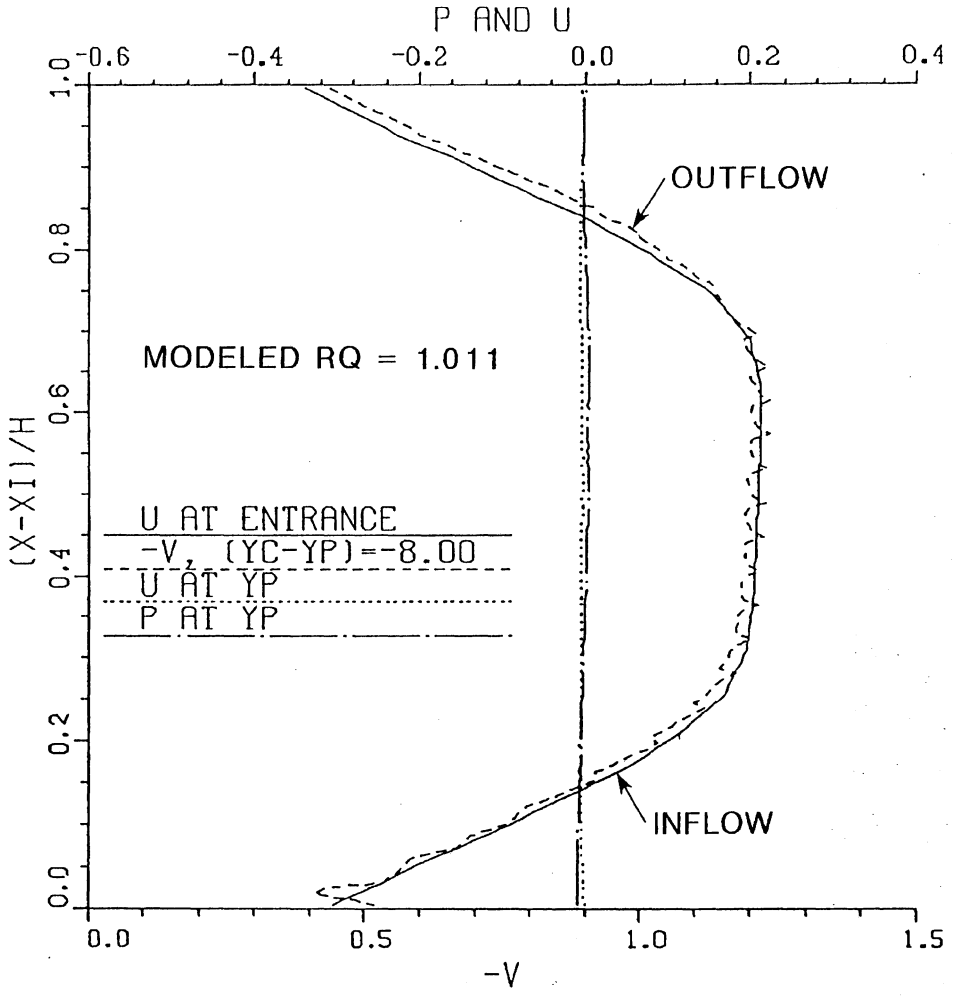


Fig. 27. Velocity and pressure distributions with 1.5 degree underturning and Re $\doteq 1.2\times10^7$.

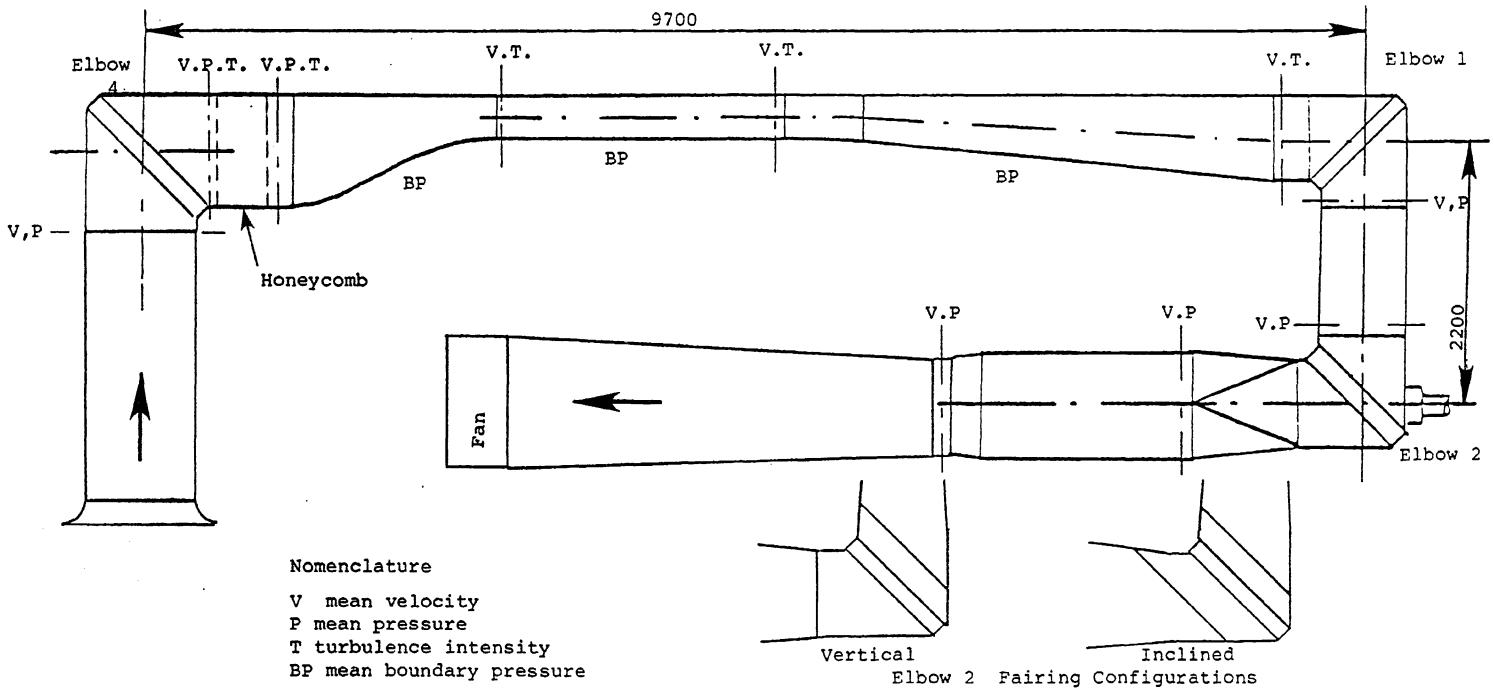


Fig. 28. Sketch of 1 to 5 physical model.

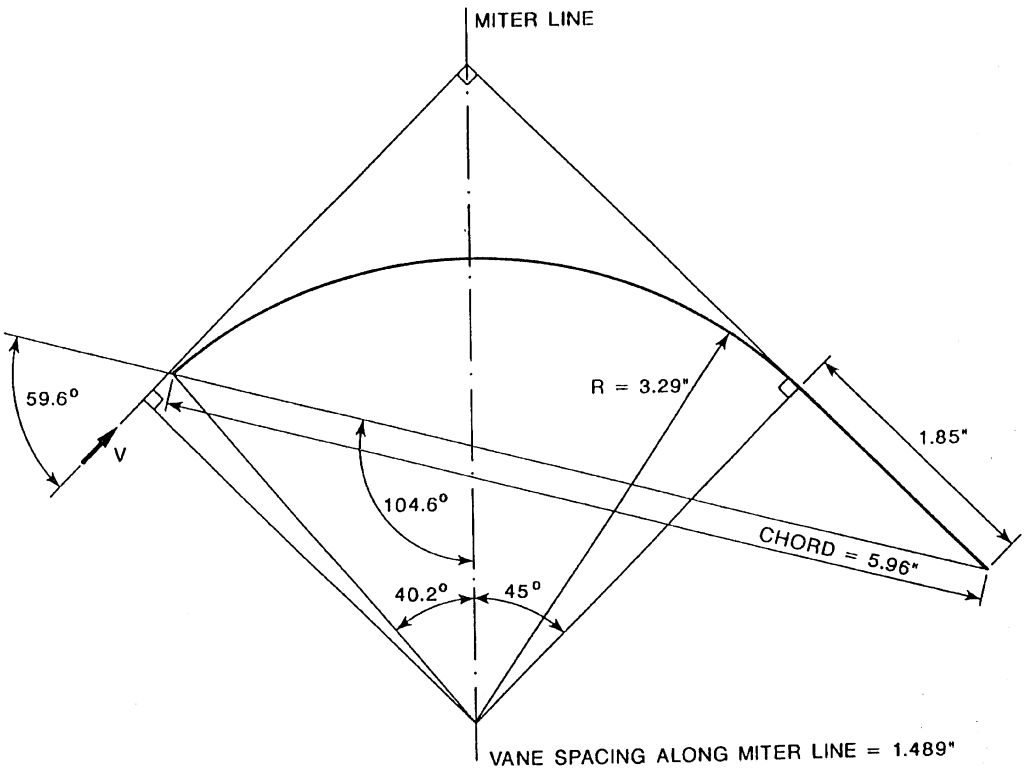


Fig. 29. Constant thickness turning vane profile.

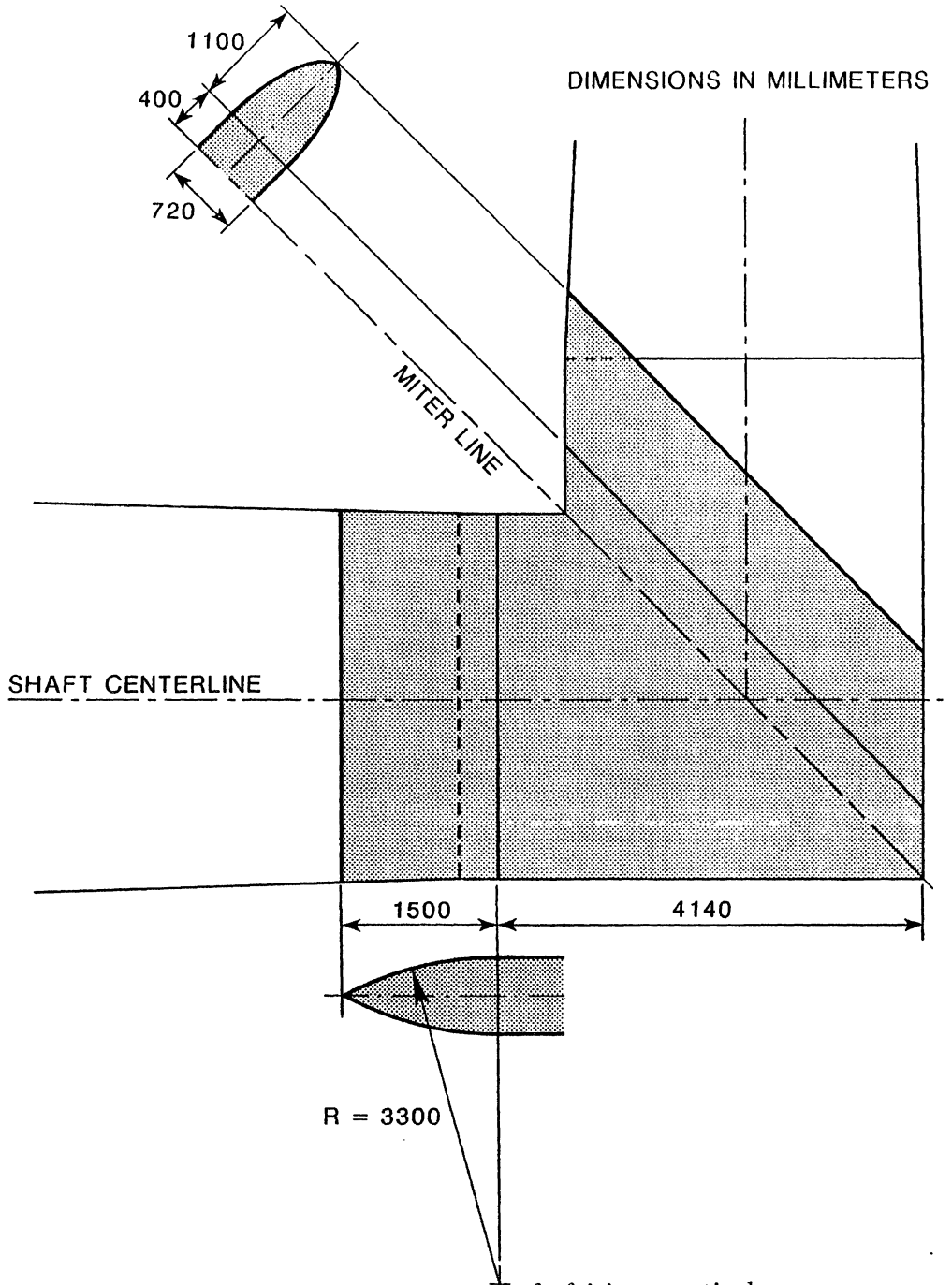


Fig. 30. Elbow No. 2 pump shaft fairing, vertical.

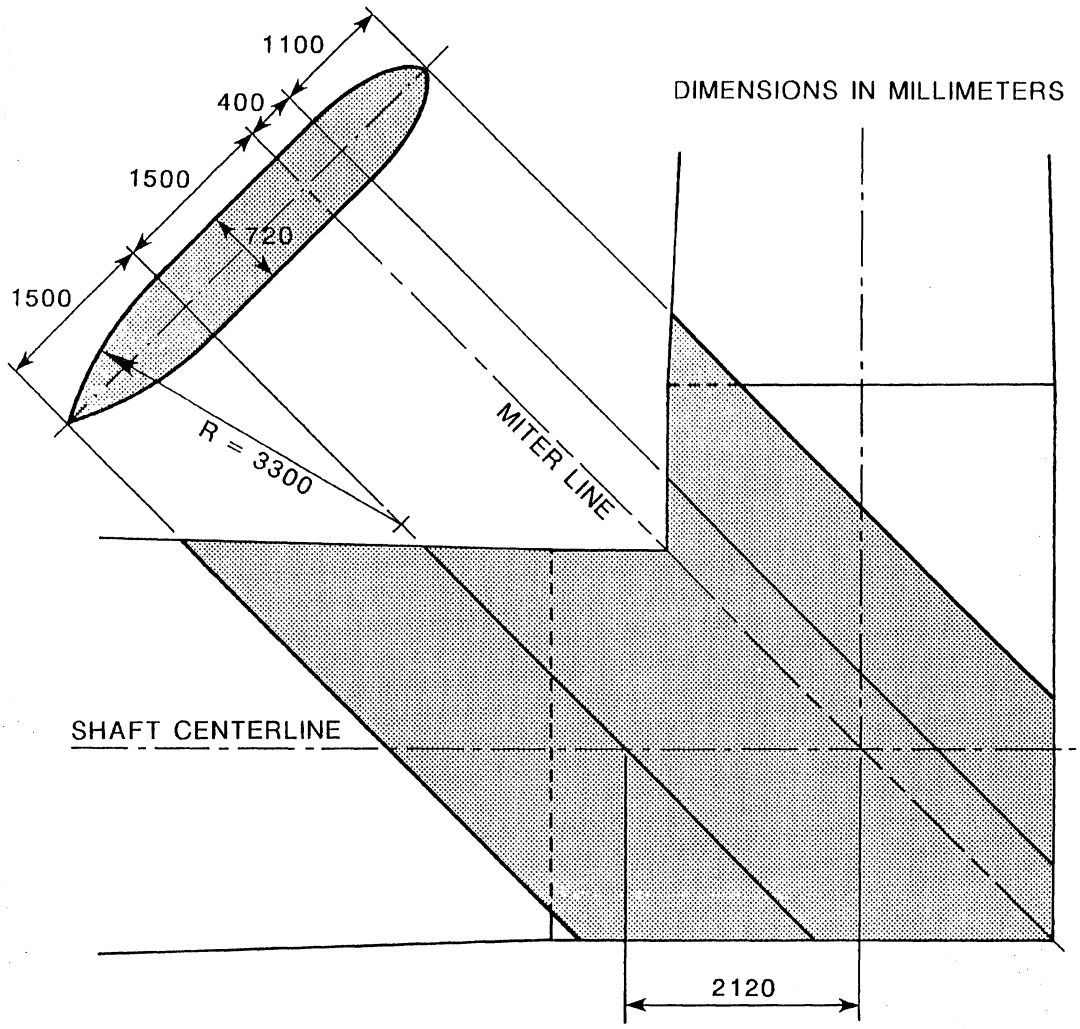


Fig. 31. Elbow No. 2 pump shaft fairing, inclined.

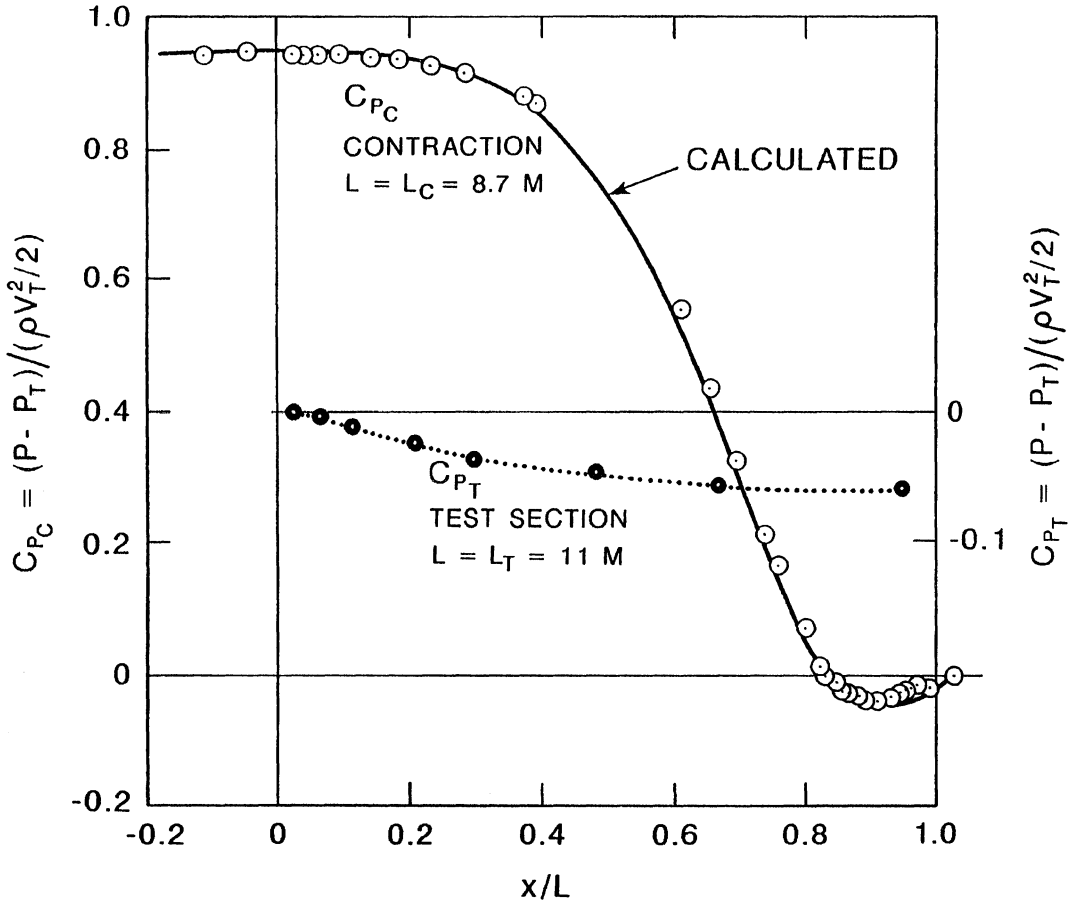


Fig. 32. Boundary pressure distributions, bottom centerline of contraction and test section.

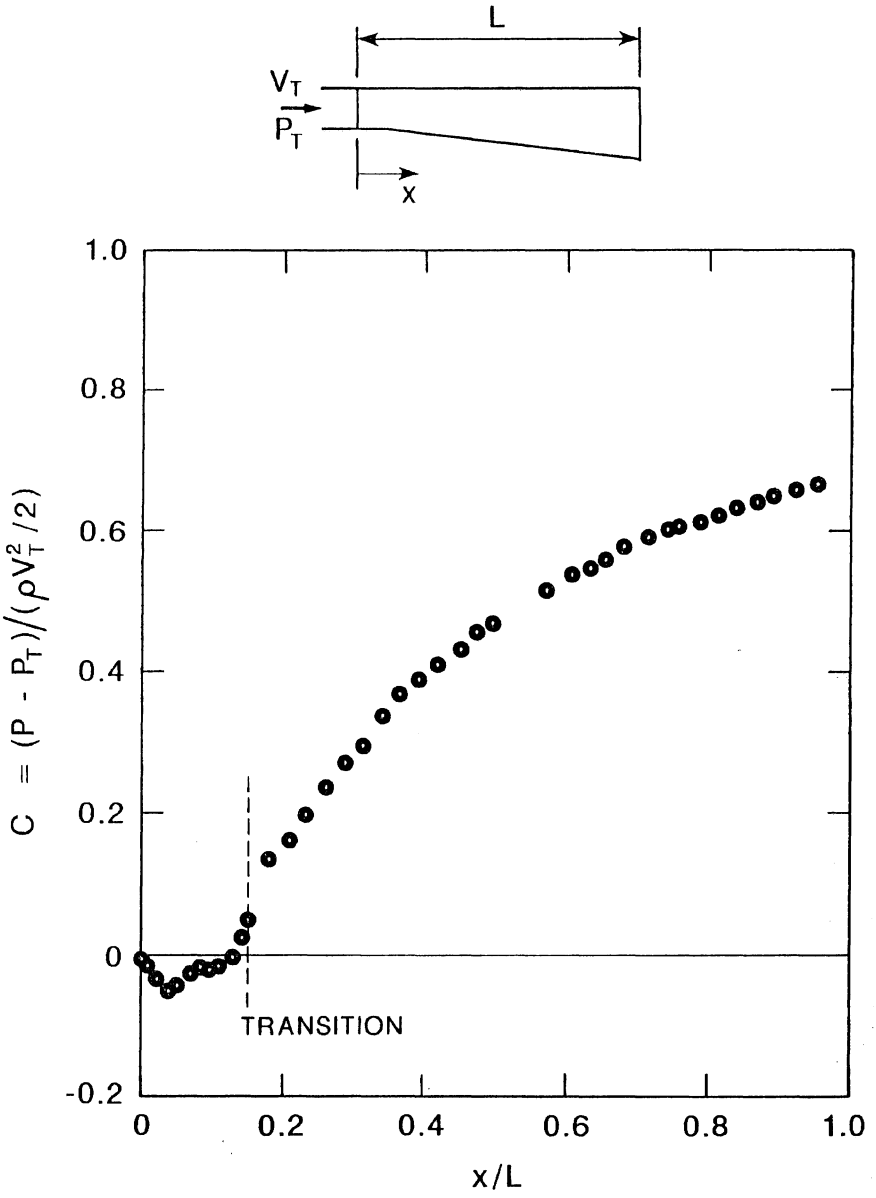


Fig. 33. Boundary pressure distribution bottom centerline, main diffuser.

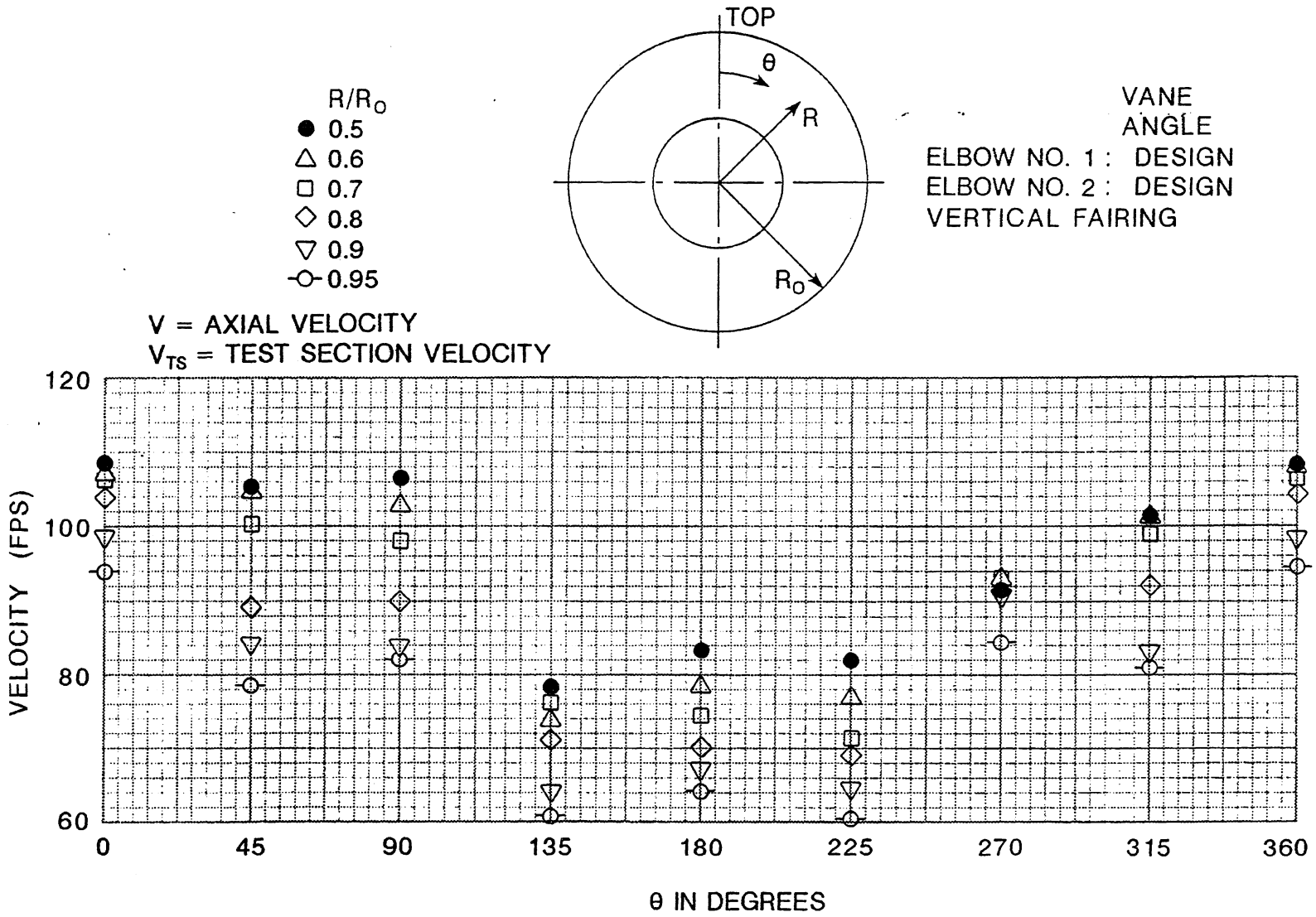


Fig. 34. Pump intake velocity distribution—plate vanes.

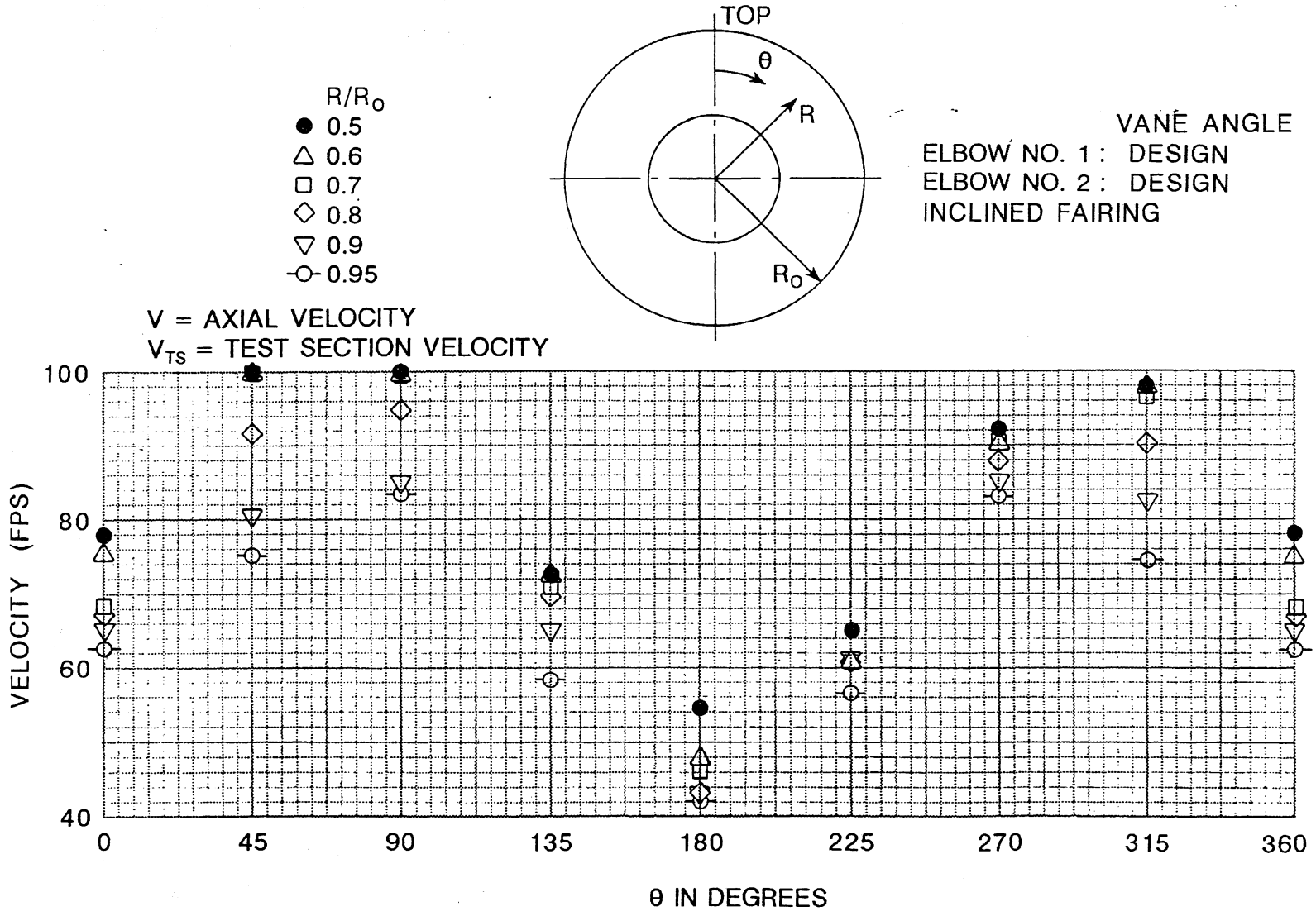


Fig. 35. Pump intake velocity distribution—contoured vanes.

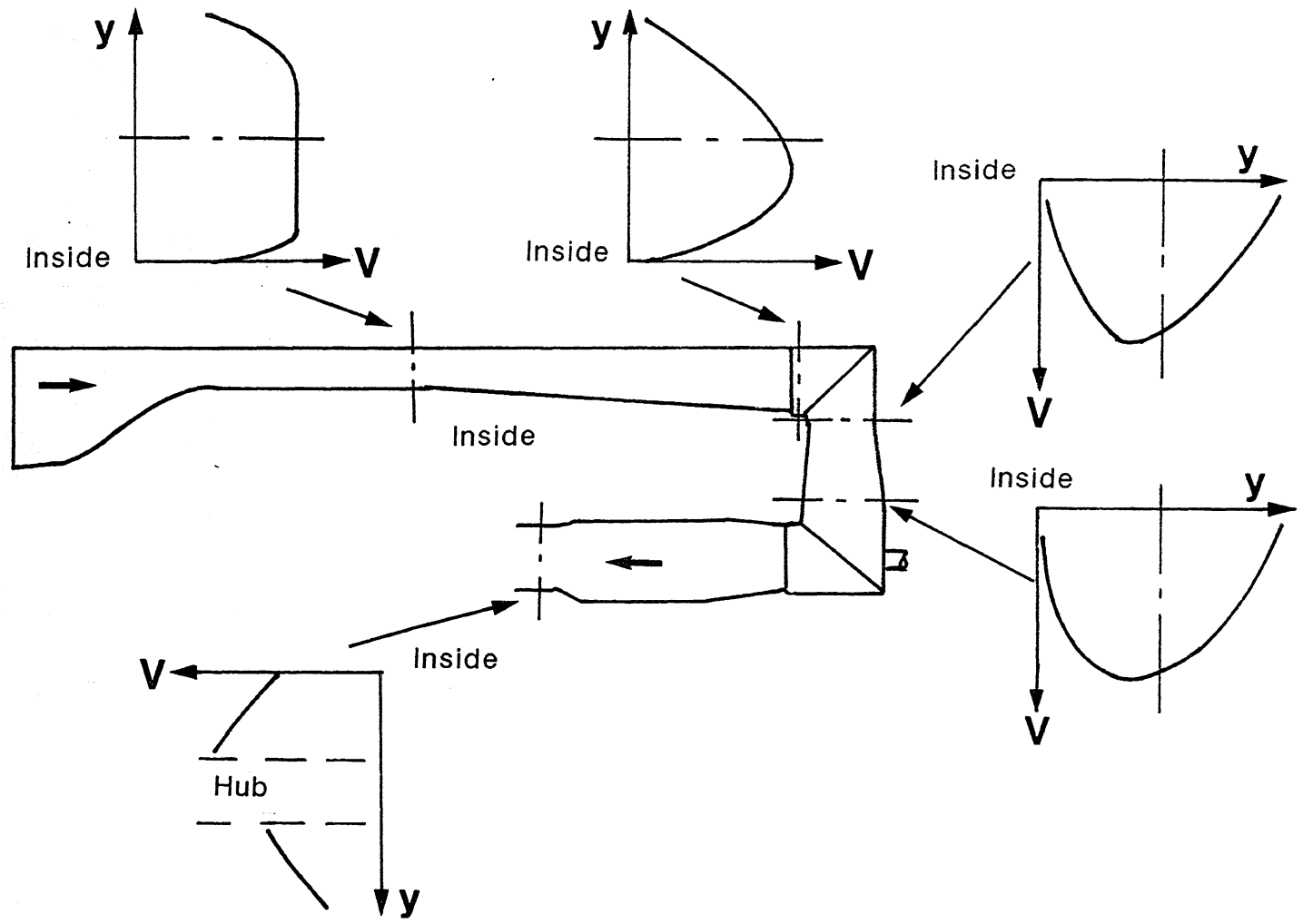


Fig. 36. Variation of vertical plane velocity profiles around circuit.

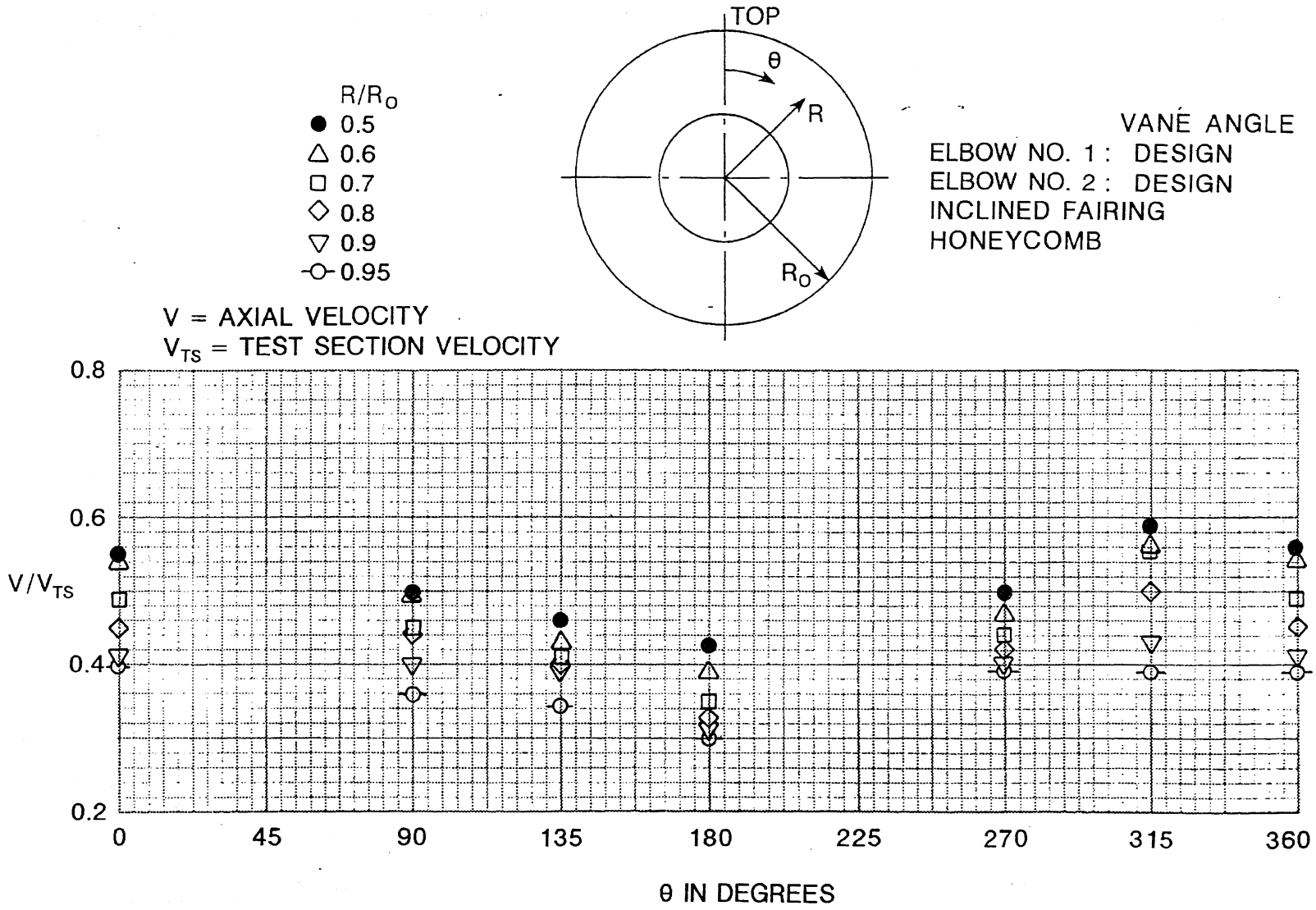


Fig. 37. Pump intake velocity distribution, with honeycomb.

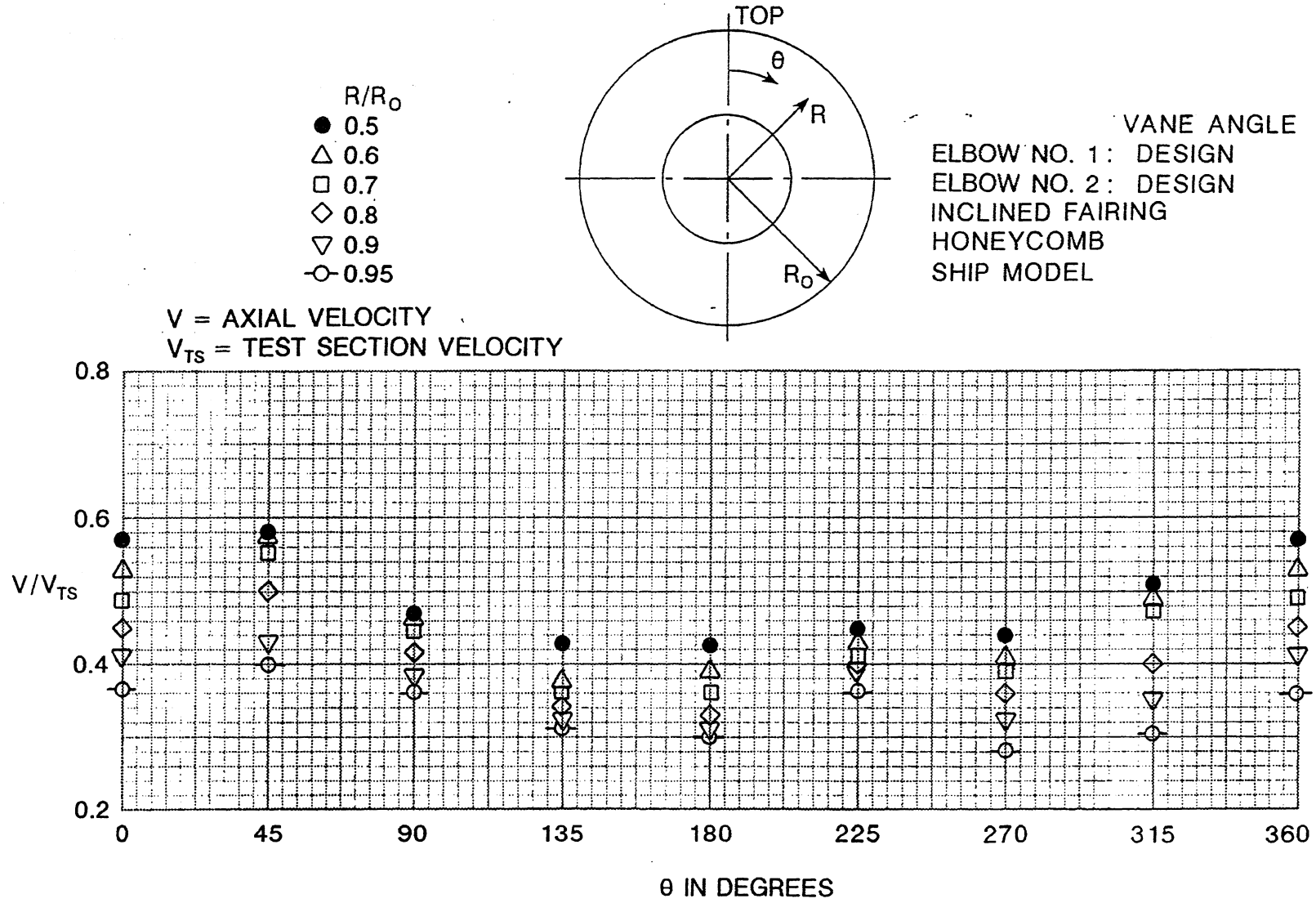


Fig. 38. Pump intake velocity distribution, with honeycomb and ship model.

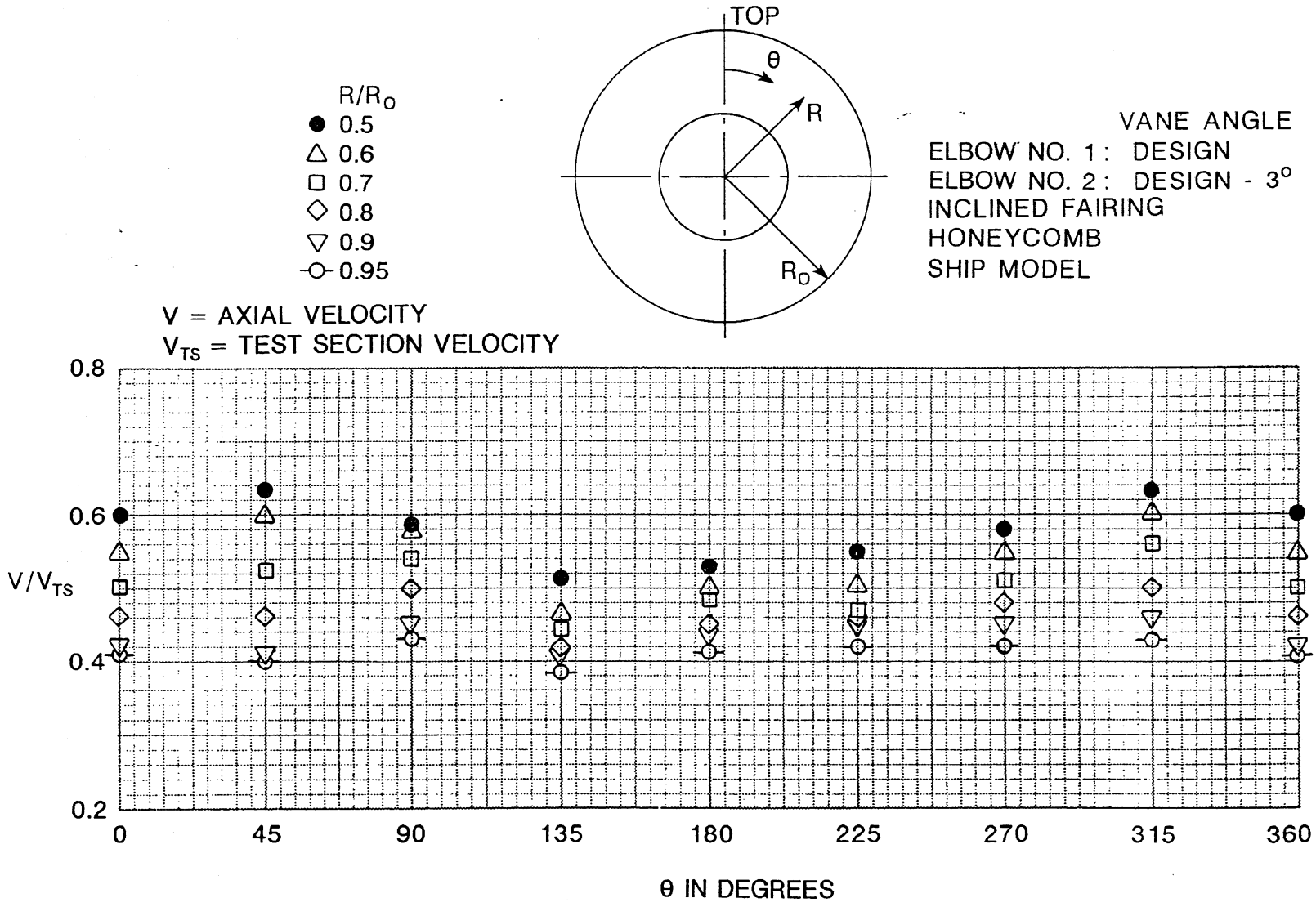


Fig. 39. Pump intake velocity distribution, Elbow No. 2, vanes 3° off design.

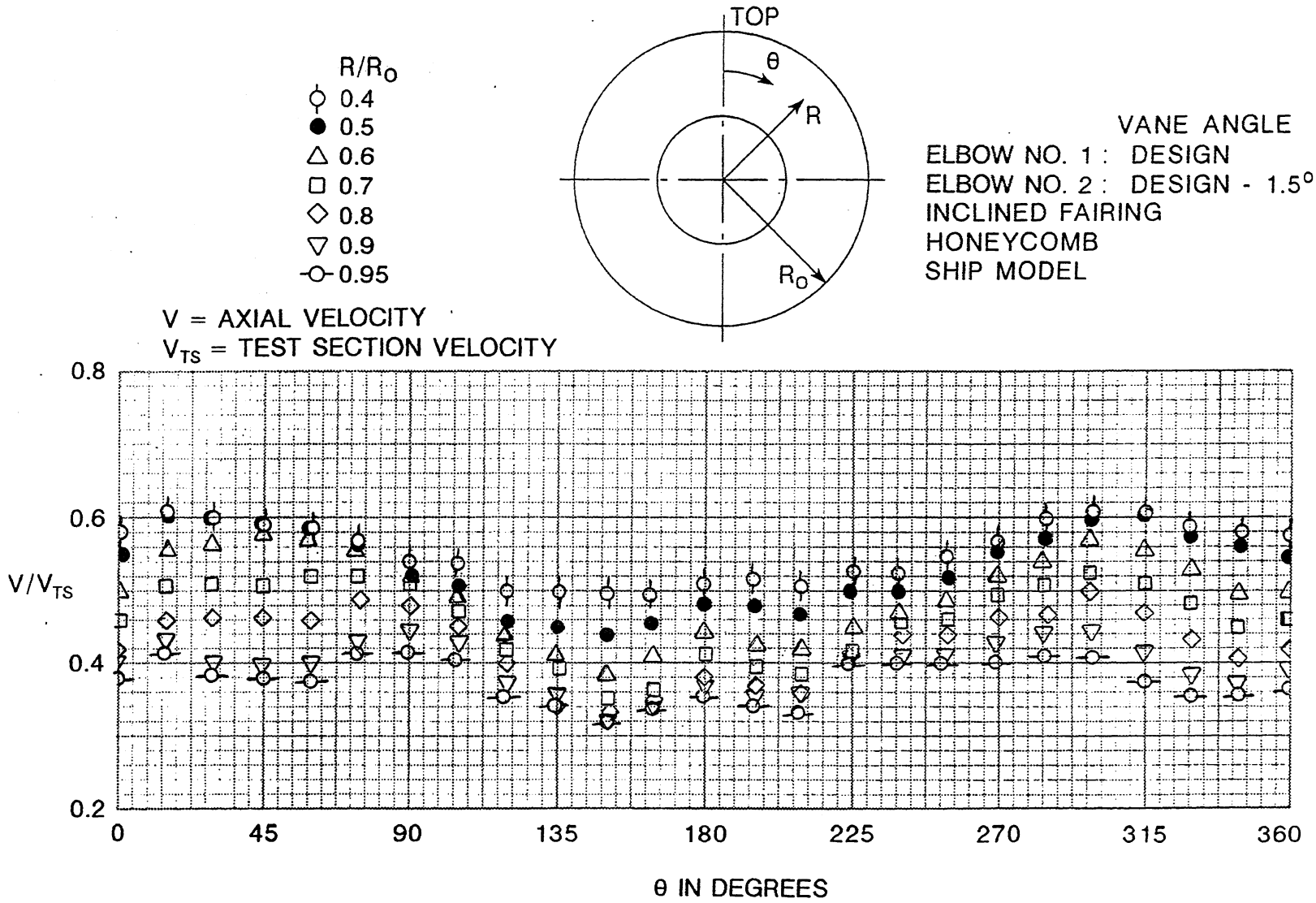


Fig. 40. Pump intake axial velocity distribution—final design.

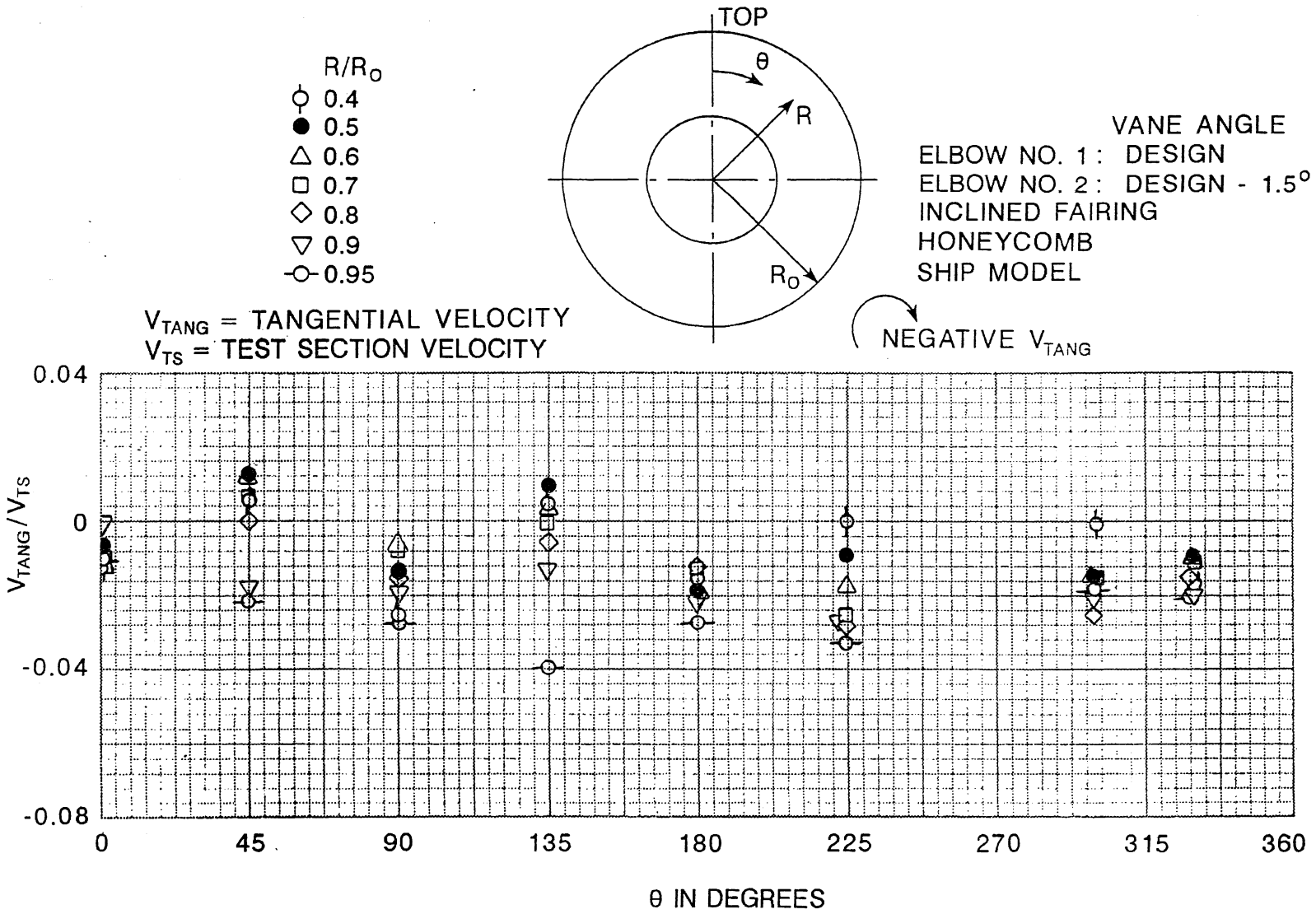


Fig. 41. Pump intake tangential velocity distribution—final design.

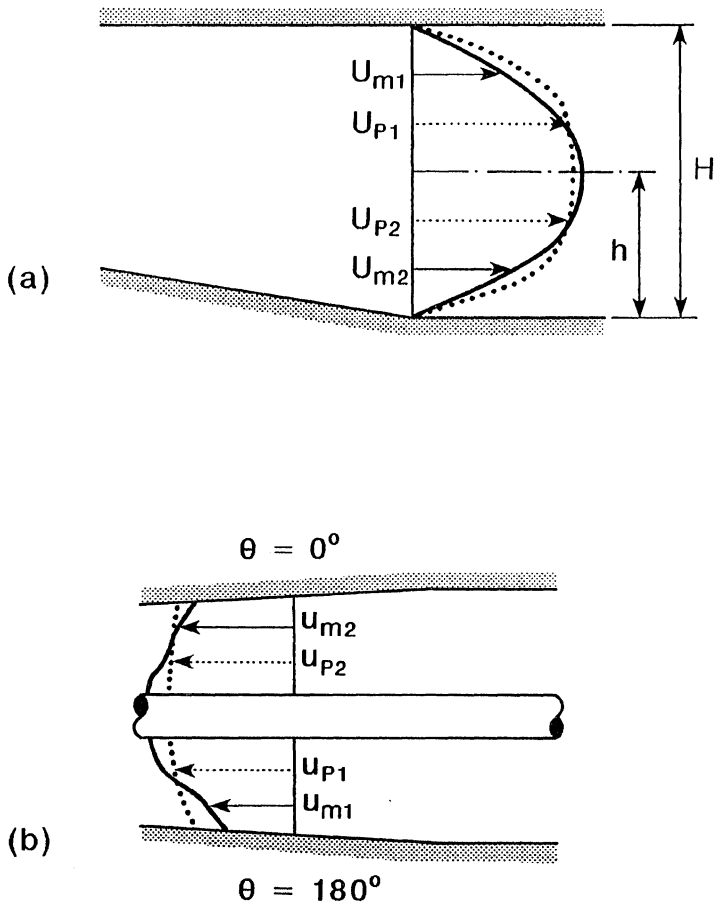


Fig. 42. Definition sketch for velocity distributions.

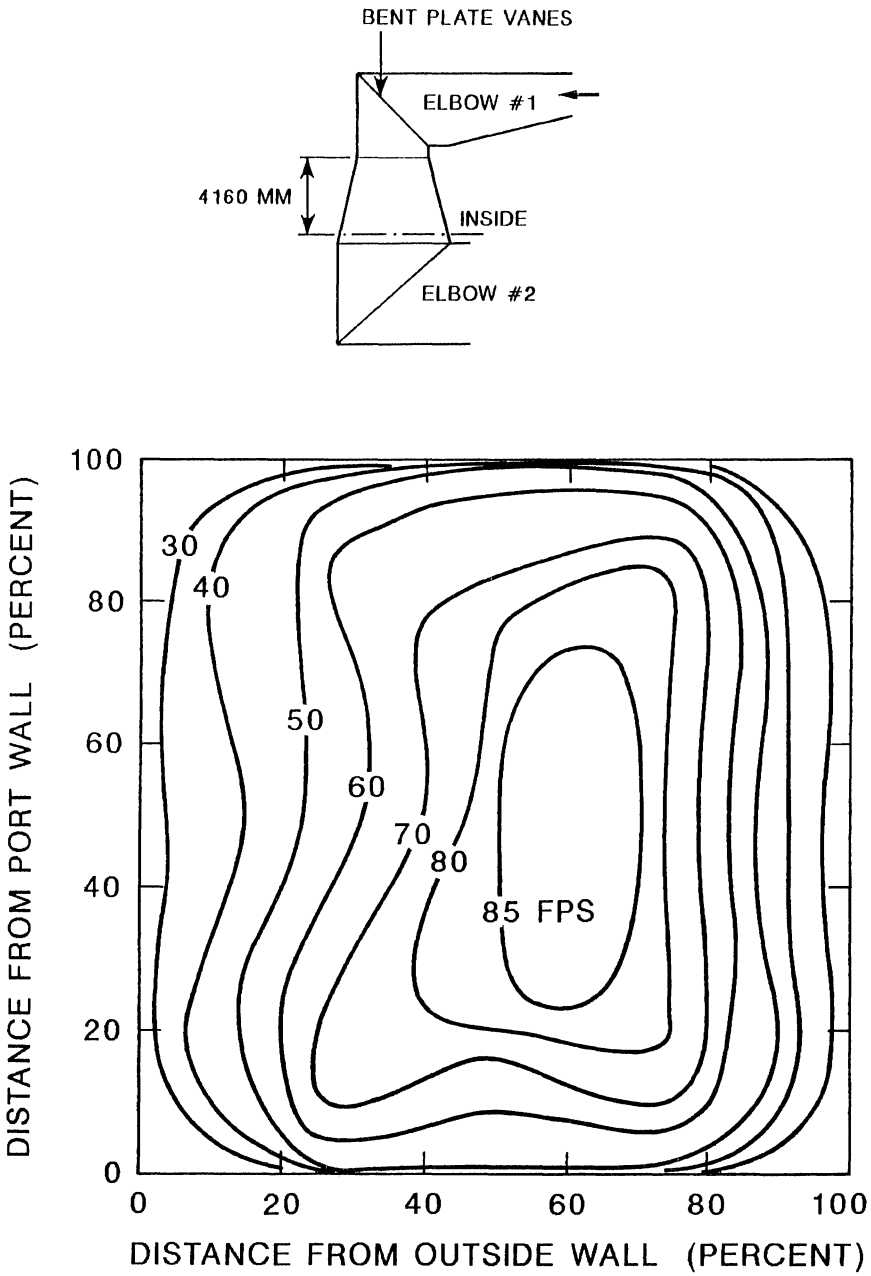


Fig. 43. Velocity contours at inlet to Elbow No. 2.

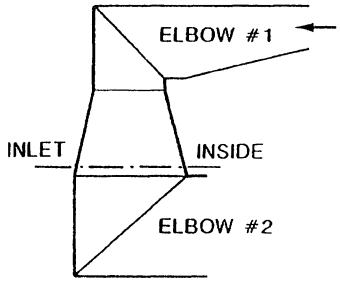


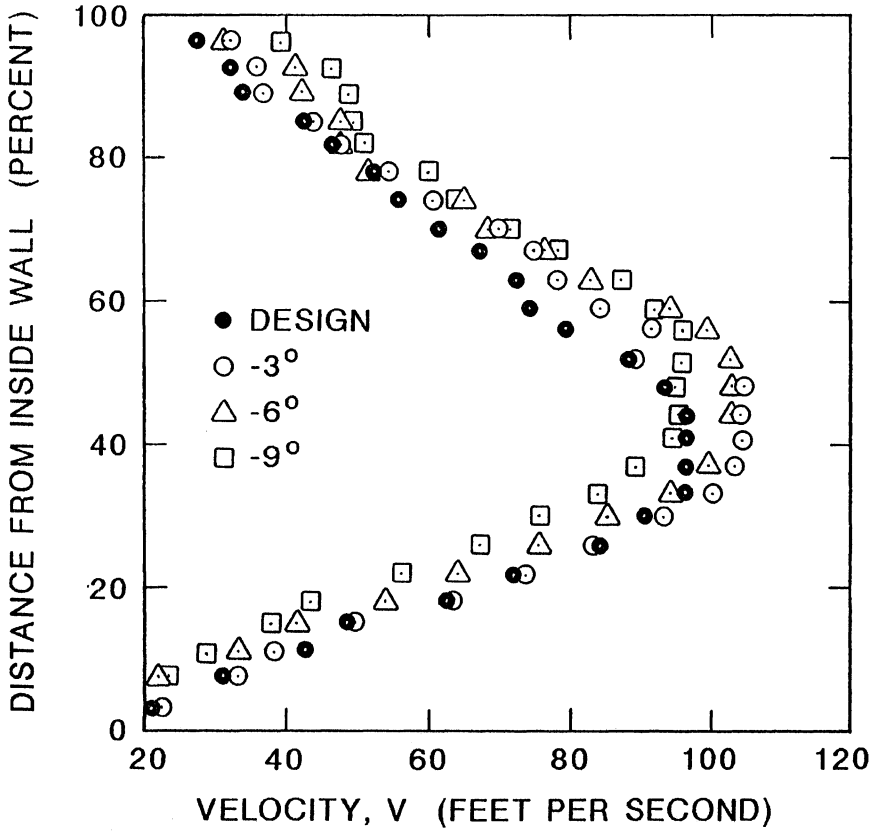


Fig. 44. Effect of reducing vane angle in Elbow No. 1 on centerline velocity profiles at Elbow No. 2.

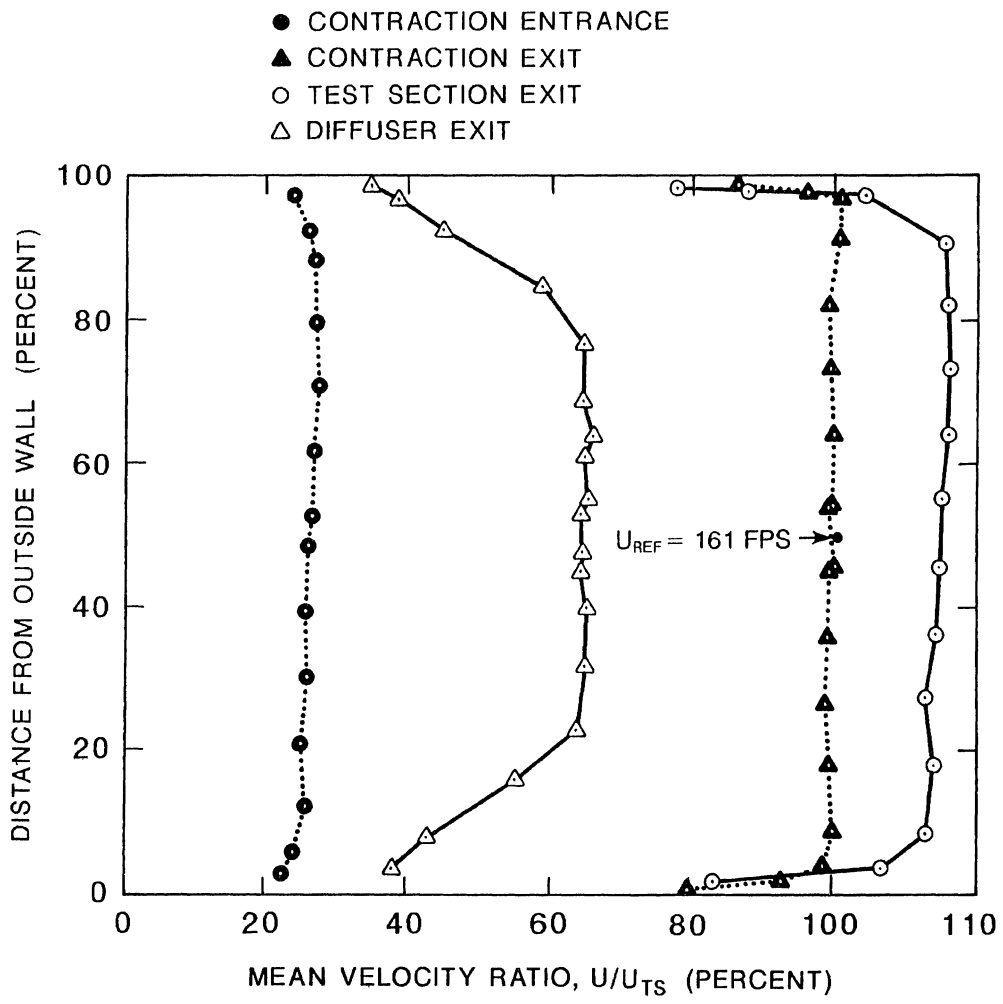


Fig. 45. Velocity profiles on horizontal centerline.

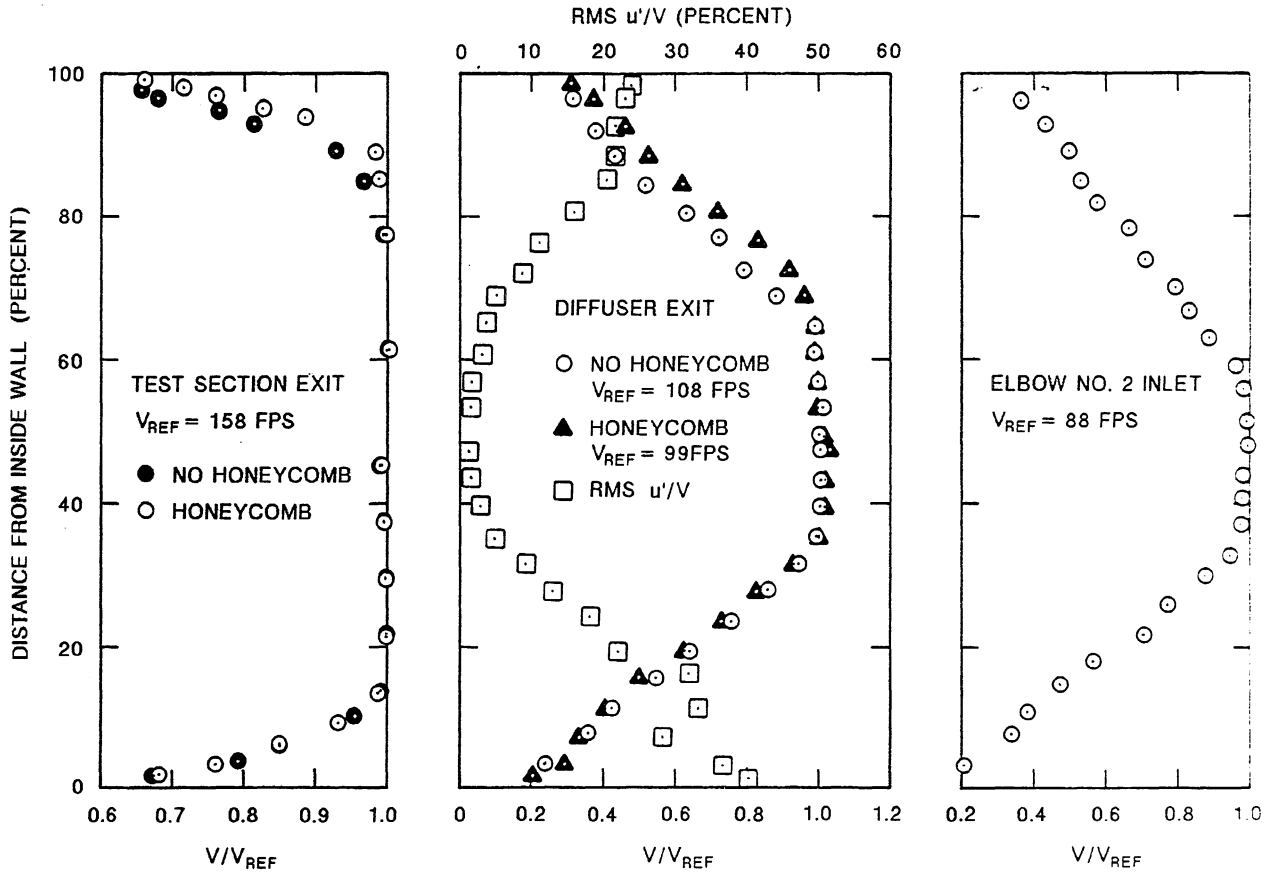


Fig. 46. Vertical centerline velocity profiles, with honeycomb Elbow No. 1 vanes—design angle.

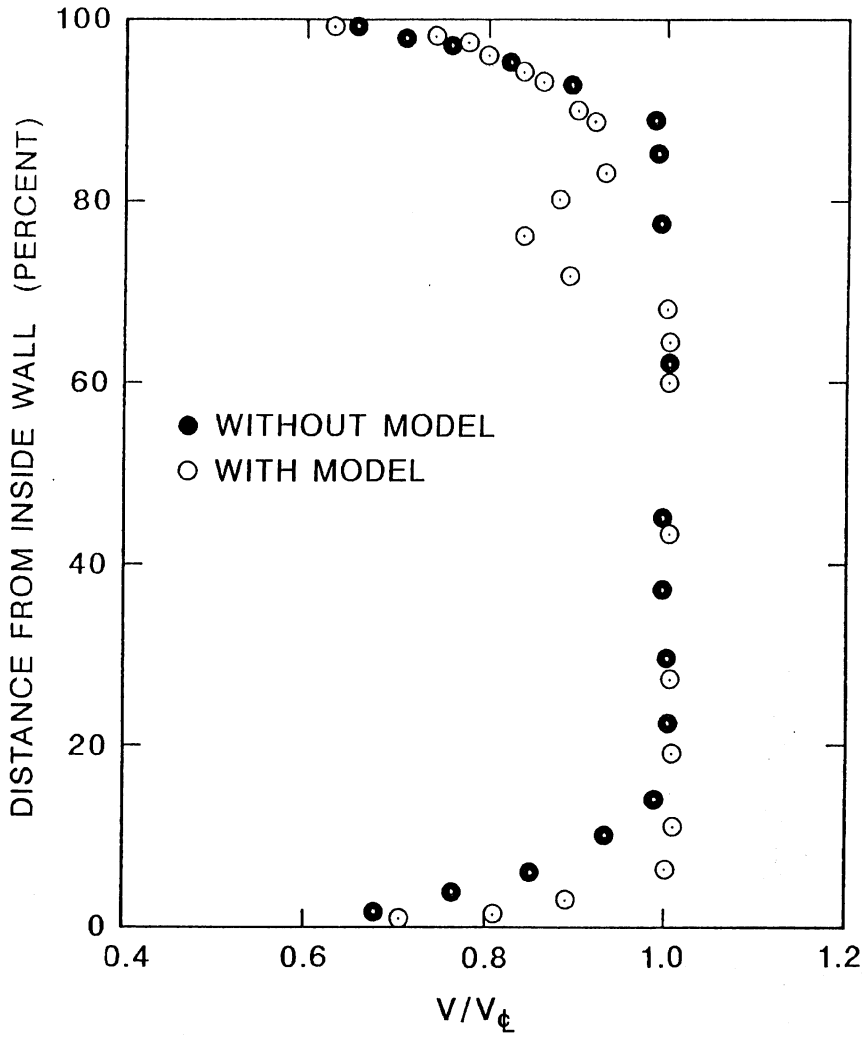


Fig. 47. Vertical velocity profiles at test section exit with ship model.

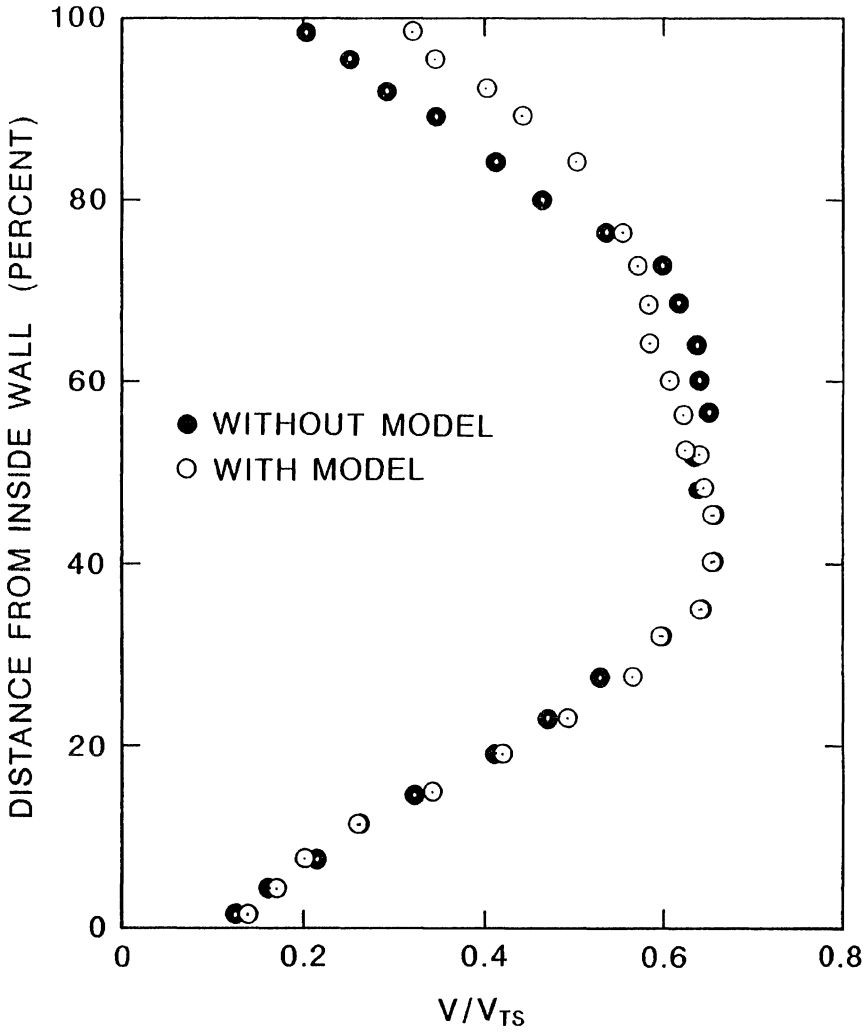


Fig. 48. Vertical velocity profiles at diffuser exit with ship model.

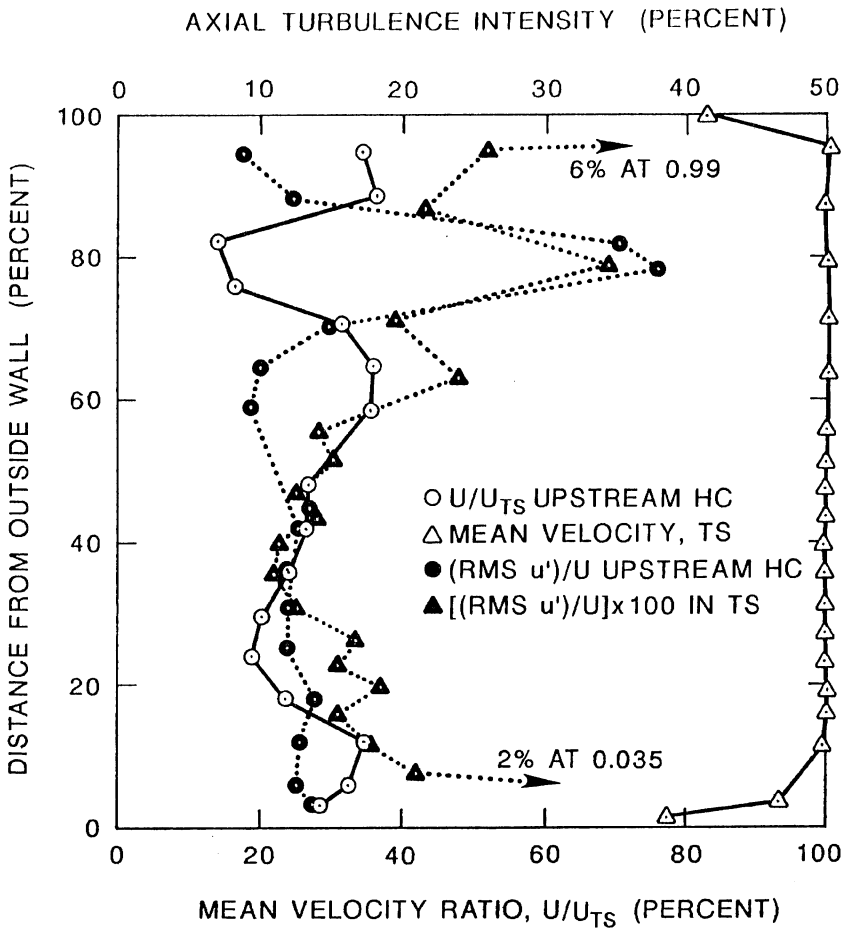


Fig. 49. Velocity and turbulence intensity profiles, upstream of honeycomb and test section entrance.

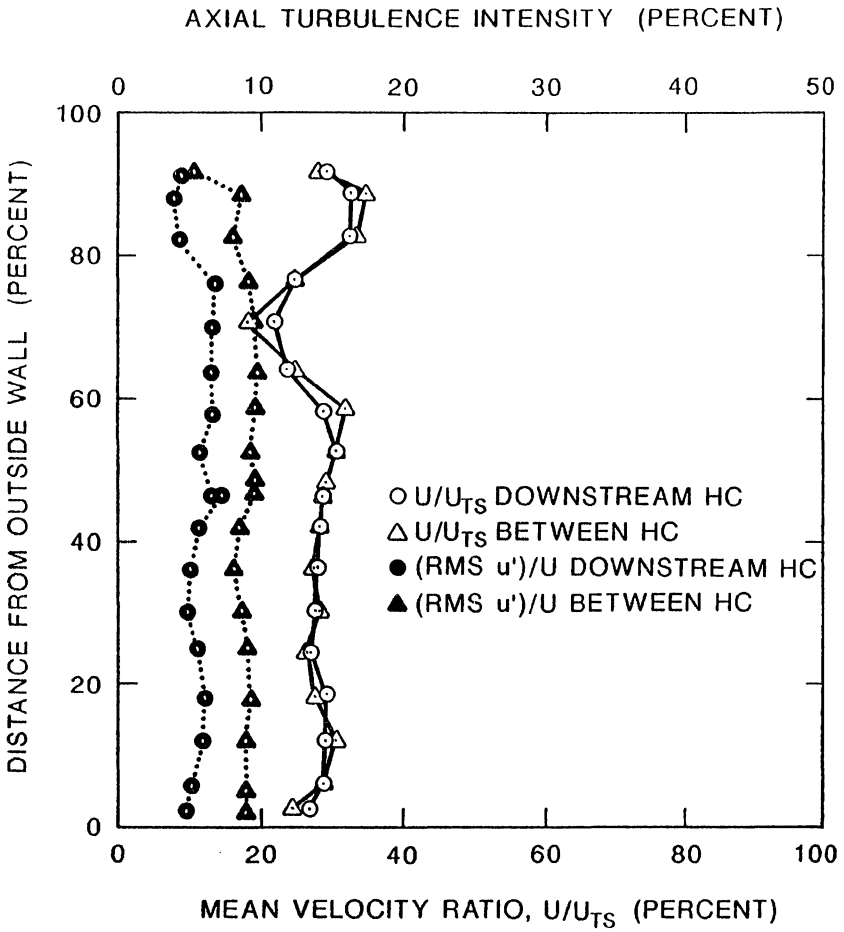


Fig. 50. Velocity profiles and turbulence intensity downstream of first and second honeycomb.